

DTIC FILE COPY

4

A Final Technical Report  
Contract No. N00014-82-K-0309

THE INVESTIGATION OF THE FRACTURE OF TITANIUM ALLOYS BY  
IN-SITU AND ANALYTICAL MICROSTRUCTURAL TECHNIQUES

Submitted to:

Office of Naval Research  
800 North Quincy Street  
Arlington, Virginia 22217-5000

Attention: Dr. D. E. Polk  
Program Officer  
Materials Division  
Code 1131

Submitted by:

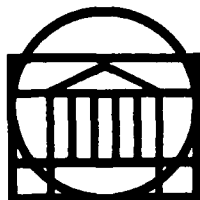
Heinz G. F. Wilsdorf  
William G. Reynolds Professor of Materials Science

AD-A197 514

DISTRIBUTION STATEMENT A  
Approved for public release  
Distribution Unlimited

DTIC  
SELECTED  
JUL 08 1988  
S E D

Report No. UVA/525375/MS88/103  
June 1988



SCHOOL OF ENGINEERING AND  
APPLIED SCIENCE

DEPARTMENT OF MATERIALS SCIENCE

UNIVERSITY OF VIRGINIA  
CHARLOTTESVILLE, VIRGINIA 22901

A Final Technical Report  
Contract No. N00014-82-K-0309

THE INVESTIGATION OF THE FRACTURE OF TITANIUM ALLOYS BY  
IN-SITU AND ANALYTICAL MICROSTRUCTURAL TECHNIQUES

Submitted to:

Office of Naval Research  
800 North Quincy Street  
Arlington, Virginia 22217-5000

Attention: Dr. D. E. Polk  
Program Officer  
Materials Division  
Code 1131

Submitted by:

Heinz G. F. Wilsdorf  
William G. Reynolds Professor of Materials Science

Department of Materials Science  
SCHOOL OF ENGINEERING AND APPLIED SCIENCE  
UNIVERSITY OF VIRGINIA  
CHARLOTTESVILLE, VIRGINIA

Report No. UVA/525375/MS88/103

June 1988

Copy No. \_\_\_\_\_

REPORT DOCUMENTATION PAGE

1a. REPORT SECURITY CLASSIFICATION Unclassified		1b. RESTRICTIVE MARKINGS None	
2a. SECURITY CLASSIFICATION AUTHORITY		3. DISTRIBUTION/AVAILABILITY OF REPORT Approved for public release; distribution unlimited	
2b. DECLASSIFICATION/DOWNGRADING SCHEDULE			
4. PERFORMING ORGANIZATION REPORT NUMBER(S) UVA/525375/MS88/103		5. MONITORING ORGANIZATION REPORT NUMBER(S)	
6a. NAME OF PERFORMING ORGANIZATION University of Virginia Dept. of Materials Science	6b. OFFICE SYMBOL (If applicable)	7a. NAME OF MONITORING ORGANIZATION Office of Naval Research Resident Representative	
6c. ADDRESS (City, State and ZIP Code) Thornton Hall Charlottesville, VA 22901		7b. ADDRESS (City, State and ZIP Code) 818 Connecticut Avenue Eighth Floor Washington, DC 20006	
8a. NAME OF FUNDING/SPONSORING ORGANIZATION Office of Naval Research	8b. OFFICE SYMBOL (If applicable)	9. PROCUREMENT INSTRUMENT IDENTIFICATION NUMBER N00014-82-K-0309	
8c. ADDRESS (City, State and ZIP Code) 800 North Quincy Street Arlington, VA 22217-5000		10. SOURCE OF FUNDING NOS.	
11. TITLE (Include Security Classification) see 16.		PROGRAM ELEMENT NO.	TASK NO.
12. PERSONAL AUTHOR(S) H. G. F. Wilsdorf		PROJECT NO.	WORK UNIT NO.
13a. TYPE OF REPORT Final	13b. TIME COVERED FROM 3/1/82 TO 2/28/88	14. DATE OF REPORT (Yr., Mo., Day) 1988 June	15. PAGE COUNT 109
16. SUPPLEMENTARY NOTATION The Investigation of the Fracture of Titanium Alloys by In-Situ and Analytical Microstructural Techniques			
17. COSATI CODES		18. SUBJECT TERMS (Continue on reverse if necessary and identify by block number)	
FIELD	GROUP	SUB. GR.	
19. ABSTRACT (Continue on reverse if necessary and identify by block number)			
<p>ABSTRACT</p> <p>To study the effects of microstructures on crack propagation in titanium and titanium alloys was the prime objective of this project. The initial phase consisted of producing and characterizing microstructures in Ti-8Mn and in Ti-10V-2Fe-3Al. Other preliminary work was concerned with a determination of void initiation sites in C.P. titanium.</p> <p style="text-align: right;">continued</p>			
20. DISTRIBUTION/AVAILABILITY OF ABSTRACT UNCLASSIFIED/UNLIMITED <input checked="" type="checkbox"/> SAME AS RPT <input type="checkbox"/> OTIC USERS <input type="checkbox"/>		21. ABSTRACT SECURITY CLASSIFICATION Unclassified	
22a. NAME OF RESPONSIBLE INDIVIDUAL Dr. D. E. Polk		22b. TELEPHONE NUMBER (Include Area Code) 202-696-3401	22c. OFFICE SYMBOL

The discovery that fracture surfaces exhibited limited areas with unusual dimple features, interpreted to have been caused by high temperatures, led to research on the temperature rise of moving crack tips. Experimentally, this entailed mechanical measurements using strain rates between  $10^{-3} \text{ sec}^{-1}$  and  $10^3 \text{ sec}^{-1}$ , the determination of stress intensity rates, straining in vacuum, measurement of fracture topographies by stereophotogrammetry, and the recording of light emission during fracture. Three theoretical models were developed to explain the above hypothesis; the first explored the extent of thermal-mechanical coupling by finite element analysis, the second developed the geometry of adiabatic shear for plane stress specimens, and the third consisted of a numerical analysis of crack tip temperatures based on a new development of microstructural plasticity for fast moving cracks. Results from all phases of this research provided support for the contention that the melting point can be exceeded at certain local areas along the crack flank for the high strength, low thermal conductivity titanium alloys investigated.

#### Acknowledgement

Dr. Bruce MacDonald, Program Manager for Metallic Materials, deserves our sincere thanks for his continuous support and his encouragement in the course of this study.

THE INVESTIGATION OF THE FRACTURE OF TITANIUM  
 ALLOYS BY IN-SITU AND ANALYTICAL  
 MICROSTRUCTURAL TECHNIQUES  
TABLE OF CONTENTS

	<u>Page</u>
I. INTRODUCTION AND OVERVIEW .....	1
II. VOID INITIATION PRECEDING DUCTILE FRACTURE IN POLYCRYSTALLINE TITANIUM .....	7
III. THE EFFECT OF THERMAL-MECHANICAL COUPLING AT THE HEAD OF A RAPIDLY LOADED CRACK TIP .....	35
IV. A GEOMETRICAL MODEL OF THE STRAIN RATE DEPENDENT FRACTURE OF Ti-8Mn .....	67
V. A NUMERICAL MODEL FOR CALCULATING THE TEMPERATURE RISE AT CRACK TIPS IN A TITANIUM ALLOY .....	99

Appendix I  
 Appendix II  
 Presentations  
 Publications  
 Degrees Awarded

Accession For	
NTIS GRA&I	<input checked="" type="checkbox"/>
DTIC TAB	<input type="checkbox"/>
Unannounced	<input type="checkbox"/>
Justification	
By _____	
Distribution/	
Availability Codes	
	Avail and/or
Dist	Special
<b>A-1</b>	





SECTION I  
INTRODUCTION AND OVERVIEW

The objective of this project was to develop an understanding of the influence of microstructure on the fracture of ductile titanium alloys and specifically on their fracture toughness. The microstructures of most titanium alloys are complex and their relationship to fracture toughness is rather involved as reported earlier by Hirth and Froes [1].

The project was started with a study of void initiation in P. C. titanium by correlating tensile data with detailed observations of fracture surfaces examined by scanning electron microscopy (SEM). Grain size was chosen as structural variable, and a range from 13  $\mu\text{m}$  to 1310  $\mu\text{m}$  was covered. In the past, the 3-D character of fracture surfaces had been neglected and most measurements were taken from the 2-D projection. Our work was done with SEM stereo-pairs and the features of fracture surfaces were measured with a light spot stereoscope. Concentrating on void initiation during deformation leading to ductile fracture by void coalescence, it was found that up to grain sizes of about 50  $\mu\text{m}$  the primary void initiation site was at grain boundary triple points. At larger grain sizes, void initiation sites were seen at slip band intersections, interaction of dislocation avalanches with grain boundaries, grain boundary ledges, twin intersections, and triple points. By reconstructing the topography of matching fracture surfaces it was possible to determine the sequence of void initiation and the subsequent growth of voids towards their coalescence for specific cross sections.

Turning to titanium alloys the research focused on crack propagation selecting Ti-10V-2Fe-3Al for plane strain fracture and Ti-8Mn for the plane stress mode. Our early SEM stereo observations of fracture surfaces revealed in both alloys limited areas of droplet-like features at the dimple walls. The two most obvious interpretations led us to believe that these features were due to an artifact from oxidation or that the melting point had been exceeded at the moment of final separation and the droplet-like dimple wall remnants represented solidified molten material. The experimental approach involved fractures in vacuum and argon, exposure to short heat flashes, and attempts to record radiation possibly coming from the fracture location.

Theoretically, calculations were made initially to obtain a ball park figure to see whether indeed a temperature rise exceeding the melting point at a few local areas during the final separation was a reasonable conclusion and, if so, should be pursued further. A summary of these early deliberations is provided in Appendix I [2]. In that paper the transformation of plastic deformation during straining preceding fracture into heat was estimated as a first contribution, but was found negligible. Following, an equation developed by Rice and Levy [3] was adapted to our situation with the result that, theoretically, a temperature of more than 1,000°C at the tip could be generated during crack propagation. And finally, dislocation theory was applied to the rupture of microligaments which always develop between voids in ductile metals, this being the last step in the fracture process; an additional 300°C - 500°C can be generated locally by this mechanism. Adding the three temperature contributions reassured us that our interpretation of the experimental results as a melting/solidification phenomenon was reasonable. Details of microstructural effects at the crack tip in general are provided in Appendix II [4]. In addition to two Masters Theses [5,6], two Ph.D. Theses have documented by various research techniques [7,8] our hypothesis.

One can anticipate that the development of heat at the crack tip depends on the rate of crack propagation. This was explored with the metastable beta Ti-10V-2Fe-3Al alloy which was subjected to strain rates from quasistatic ( $10^{-3} \text{ s}^{-1}$ ) to near ballistic ( $10^3 \text{ s}^{-1}$ ) in tensile loading. Yield stress, ultimate tensile stress, reduction in area, and strain to fracture increase with increasing strain rate,  $\dot{\epsilon}$ . With a four order of magnitude increase of  $\dot{\epsilon}$  the fracture toughness was seen to increase by 82%. The tortuosity of the tensile fracture surfaces was of interest in this connection and changes due to the increasing strain rates were measured with a semi-automatic stereographic mapping system (built by Bryant [9]). In order to assess the magnitude of the thermal mechanical coupling at the crack tip, a finite element analysis was carried out which is summarized in this report (pp.35-66). It should be added that the boundary conditions for the finite element method were obtained from experimental measurement on Ti-10-2-3. This work confirmed the high temperature rise at the crack tip.

The alpha/beta alloy Ti-8Mn was investigated in sheet form with emphasis on the verification of the "microroughened" or droplet-like

features on the fracture surfaces by heat and the possible involvement of adiabatic shear including the corresponding glide geometries. The first task involved the exposure of regular dimples to flashes (0.5 sec) of a neutral hydrogen/oxygen torch flame. Re-examination of these treated surfaces showed indeed a resemblance of the "microroughened" features observed after fracture. Since surface oxides and nitrides rapidly form on titanium above 650°C, it was suggested that oxidation might be responsible for the observed "microroughening." To investigate this possibility, tensile tests were performed in a chamber which had been evacuated to  $10^{-4}$  Pa and backfilled with argon four times. Although oxygen and nitrogen were not completely absent in these tests, the short duration of the high temperatures and the rarified nature of the concentration of these two gases severely limits the extent of oxidation reactions. Examination of the resulting fracture surfaces revealed the same features as the air-fractures samples. This result was considered a clear indication that, although some oxidation of newly formed, heated titanium surfaces is inevitable, the surface structures found on our samples do not form primarily by an oxidation mechanism. The geometrical aspects of adiabatic shear are summarized in this report on pp. 67 to 98, and a brief account of visible light coming from the fracture area is included. All results are providing evidence for a high temperature rise ahead of the crack tip.

Our earlier analysis of the temperature rise at the crack tip was based on the Rice-Levy equation which does not include the effect of a heat increase simultaneous with the moving crack. Contrary to the earlier models by other authors who based their calculations on continuum concepts, our model (executed by Dr. K. Jagannadham, North Carolina State University, Raleigh, N.C., under subcontract) is making use of the plastic work term which in our opinion must change in the region ahead of the crack tip during crack propagation. Appropriate parameters used in the model are dislocation density in the process zone, frictional stress for dislocations, dislocation velocity, plastic strain, plastic work rate, and loading rate. Thus the workhardening characteristic in the "plastic zone" is included in the model. The results of extensive computer calculations are relating a very substantial temperature rise in the process zone to the time scale of crack propagation.

In summary, the project research explored the effect of

microstructure on the ductile fracture of C.P.Ti, Ti-8Mn, and Ti-10V-2Fe-3Al. It was found that the temperature rise ahead of the crack tip can be more than 1,000°C, more likely 1,300°C; when adding to this value the heat developed during the rupture of microligaments between voids, the melting point of these alloys was exceeded in localized areas of the crack flank. This temperature regime for the temperature rise at the crack tip could be calculated since, for the first time in a high temperature metal, a determination of the final temperature at fracture was possible with better than average precision. It should be remembered that titanium alloys have very low heat conductivity and high strength which makes it possible for adiabatic shear to occur at normal loading rates. With increasing loading rates the fracture toughness was found to increase by more than 50%.

## References

1. J. P. Hirth and F. H. Froes, Met. Trans. 8A (1977) 1165.
2. J. D. Bryant, D. D. Makel and H. G. F. Wilsdorf, Mater. Sci. Eng. 77 (1986) 85.
3. J. R. Rice and N. Levy, in A. S. Argon (ed.), Physics of Strength and Plasticity, MIT Press, Cambridge, MA (1969) 177.
4. K. Jagannadham and H. G. F. Wilsdorf, Mater. Sci. Eng., 81 (1986) 273.
5. M. A. Erickson, The Ductile Fracture of C. P. Titanium, M.Sc. Thesis, U. Virginia, 1983.
6. J. D. Bryant, The Effect of Primary Alpha Precipitates on Deformation in Ti-10V-2Fe-3Al. M.S. Thesis, U. Virginia, 1985.
7. J. D. Bryant, Deformational Heating at the Crack Tip and its Role in Fracture of Ti-10V-2Fe-3Al. Ph.D. Thesis, U. Virginia, 1987.
8. D. D. Makel, Strain Rate Dependent Processes in the Fracture of Ti-5Mn. Ph.D. Thesis, U. Virginia, 1987.
9. J. D. Bryant, Micron and Micr. Acta, 17 (1986) 237.



SECTION II  
VOID INITIATION PRECEDING DUCTILE FRACTURE  
IN POLYCRYSTALLINE TITANIUM

Based on a Masters Thesis (Materials Science) by Marjorie A. Erikson\*,  
UVa. 1983.

ABSTRACT

The objective of this research was a determination of primary void initiation sites preceding void growth in the process of deformation leading to ductile fracture in polycrystalline C. P. titanium. Stereophotogrammetry was employed to evaluate SEM fracture surfaces. Two distinct regimes of void initiation were found to operate.

- (i) Void initiation occurred primarily at grain boundary triple points in specimens with grain sizes up to 50  $\mu\text{m}$ ;
- (ii) In material with larger grain sizes additional void initiation sites were found to be at slip band intersections, interaction of dislocation groups with grain boundaries, twin intersections, and grain boundary ledges.

Quantitative topographical information was obtained from measurements with a light spot stereoscope. Reconstructing the topography of matching fracture surfaces with SEM accuracy and resolution, the time sequence of void initiation along a line on the fracture surface was obtained.

---

\* Current Address: Mrs. Marjorie A. Natishan, David W. Taylor Naval Ship R&D Center, Annapolis Laboratory, Annapolis, Maryland 21402-5067.



TABLE OF CONTENTS

	<u>Page</u>
1. INTRODUCTION .....	11
2. SAMPLE PREPARATION AND EXPERIMENTAL PROCEDURE .....	11
3. RESULTS .....	14
4. DISCUSSION .....	20
5. CONCLUSIONS .....	31
REFERENCES .....	32



# VOID INITIATION PRECEDING DUCTILE FRACTURE IN POLYCRYSTALLINE TITANIUM

## 1. INTRODUCTION

While void initiation has been covered in fair detail for particle containing alloys [1,2], experimental evidence in pure or relatively pure polycrystalline ductile metals has received only scant attention, except for fracture at higher temperatures [3]. Under creep conditions grain boundary sliding often leads to void formation at grain boundary triple points (GBTP) and theoretical models for the high temperature regime have been published [4,5]. One cannot expect that these mechanisms are operative in high melting point metals at room temperature, and plastic deformation has been invoked for void initiation by assuming the development of pile-ups when dislocations were unable to penetrate grain boundaries [6,7,8]. Also, grain boundary ledges have been thought to initiate microcracks [9]; other mechanisms are based on crossing slip bands [10], or intersecting twins [11], and bend planes [7,12].

The present investigation has as its objective to determine the locations of primary void initiation sites. Fracture experiments were made with C.P. titanium under tensile loading, and fracture surfaces were examined with a scanning electron microscope (SEM). The crack path in most metals is a tortuous one, and this is particularly true for titanium. It was found necessary to employ stereo-photogrammetry in order to obtain true measurements of fracture surface features.

## 2. SAMPLE PREPARATION AND EXPERIMENTAL PROCEDURE

Tensile samples were prepared from a 0.198 cm thick sheet of C.P. titanium. The material was 99.838% pure with an impurity content that included O, N<sub>2</sub>, C, H<sub>2</sub> and Fe<sub>2</sub>. After polishing the gauge sections of each sample with grit size decreasing to 600 grit and heat treating, the gauge lengths and cross-section areas of each sample were carefully measured. Once fracture occurred pieces containing the fracture surfaces were carefully cut approximately 0.5 cm from the fracture edge and mounted onto an aluminum specimen stub for subsequent SEM study.

A range of heat treatments was done to vary the grain size of

samples to allow a study of grain size versus tensile properties and fracture surface characteristics. Because of sample purity only the  $\alpha$ -phase of Ti is present at room temperature, so stress relief, recrystallization and grain control were the primary goals of heat treating.

Ten samples were prepared for study. Heat treatments were designed to cause a variation in grain size from 13  $\mu\text{m}$  to 1300  $\mu\text{m}$ . Table 1 lists the various samples with the heat treatment they were given and their resulting grain size.

To prevent oxygen from diffusing into the samples during heat treating, each sample was enclosed in a quartz tube evacuated to  $5 \times 10^{-7}$  torr.

For grain size determination, a piece from the shoulder of each sample was cut, mounted onto an SEM stub, encased in epoxy, and polished and etched in a solution of 10 ml HF, 5 ml  $\text{HNO}_3$  and 85 ml distilled water for  $1\frac{1}{2}$  minutes.

The tensile specimens were pulled to fracture on an Instron Universal Testing Machine. The crosshead speed was either 0.05 cm/sec or 0.005 cm/sec. Load vs. time was recorded and from this tensile properties were determined.

Fractographs of the entire surface were taken of opposing surfaces at low magnifications, using stereo techniques, as references for future higher magnification micrographs. These low magnification fractographs were also used to measure final cross-sectional area at the fracture to determine the reduction in area of each sample.

A number of pictures were taken at higher magnifications (300x to 1000x), using stereo techniques to enable a detailed three-dimensional study of the fracture surface. Thus, fracture surface features could be determined accurately by making measurements of relative height as well as relative horizontal distances.

Studies of microstructures were related to studies of fracture surface features to pinpoint primary void initiation sites in  $\alpha$ -Ti. Five to ten micrographs of each sample, polished and etched for grain size measurements, were enlarged and used to determine grain size using

TABLE 1

## GRAIN SIZES OF FRACTURE SPECIMENS

<u>SAMPLE</u>	<u>HEAT TREATMENT</u>	<u>Average Grain Size</u>	<u>Range</u>
1	$\frac{1}{2}$ hr. at 700°C furnace cool	13 $\mu\text{m}$	1-55 $\mu\text{m}$
2	$\frac{1}{2}$ hr. at 700°C air cool	21 $\mu\text{m}$	2-72 $\mu\text{m}$
3	2 hrs. at 700°C air cool	46 $\mu\text{m}$	7-188 $\mu\text{m}$
4A	2 hrs. at 1000°C air cool	178 $\mu\text{m}$	30-1210 $\mu\text{m}$
4B	2 hrs. at 1000°C air cool	200 $\mu\text{m}$	27-1215 $\mu\text{m}$
5A	5 hrs. at 1175°C furnace cool	427 $\mu\text{m}$	40-1550 $\mu\text{m}$
5B	5 hrs. at 1150°C furnace cool	420 $\mu\text{m}$	35-1490 $\mu\text{m}$
6	$8\frac{1}{2}$ hr. at 1150°C furnace cool	792 $\mu\text{m}$	70-1880 $\mu\text{m}$
7A	20 hrs. at 1150°C furnace cool	1247 $\mu\text{m}$	82-2150 $\mu\text{m}$
7B	20 hrs. at 1150°C furnace cool	1310 $\mu\text{m}$	79-2120 $\mu\text{m}$

the grain boundary-line intercept method. These pictures were also used to measure intertriple point distances by direct measurements. Measurements were made over areas of  $\sim 1000 \mu\text{m}^2$  for small grained samples and  $1000^2 - 2000^2 \mu\text{m}^2$  for larger grained samples.

Measurements of dimple diameter and interdimple distances were taken directly from stereo micrographs which allowed evaluations in 3-dimensions. Dimple diameters were taken as the line through the center of the dimple perpendicular to the long axis of the dimple. Interdimple distances were measured from the center of one dimple to the center of an adjacent dimple taking relative height variations into account by making measurements using a Hilger-Watts stereo viewer.

### 3. RESULTS

Significant mechanical properties of typical tensile samples are listed in Table 2.

An evaluation of measurements obtained from SEM fractographs indicated immediately that in small grain specimens interdimple distances corresponded primarily to intertriple point distances. This can be clearly seen in Figure 1; the measurements were taken from specimens 1-3 with average grain sizes of  $13 \mu\text{m}$ ,  $21 \mu\text{m}$ , and  $46 \mu\text{m}$ , respectively. The fit of the second peak of interdimple spacings with intertriple point spacing peaks is amazingly good. Notably, there is on each of these graphs a higher peak for interdimple spacings which lies between  $1 \mu\text{m}$  and  $3 \mu\text{m}$ . The significance of this maximum peak will be discussed in the following section. Figure 2 gives an impression of dimple size distributions in a fracture surface of specimens having grain sizes below  $50 \mu\text{m}$ .

The character of fractographs changed drastically for specimens with grain sizes of  $200 \mu\text{m}$  and larger (Figure 3). Instead of only a broad distribution of dimple sizes over the whole fracture surface, elongated ridges are also seen over a relatively large area. Dimple size distributions for four grain sizes are given in Figure 4. For these samples, interdimple distances and intertriple point distances are unrelated although the maximum peak of the first group is retained at  $1 \mu\text{m}$  to  $3 \mu\text{m}$ . The change in the fracture surface characteristics between specimens with "small" and "large" grains indicates the presence of two

TABLE 2  
TENSILE PROPERTIES FOR FOUR SAMPLES WITH DIFFERENT GRAIN SIZES

Sample	Grain Size ( $\mu\text{m}$ )	Engineering 8 Y.S. ( $\times 10^8$ Pa)	Engineering 8 U.T.S. ( $\times 10^8$ Pa)	Engineering 8 F.S. ( $\times 10^8$ Pa)	True 8 Y.S. ( $\times 10^8$ Pa)	$\bar{n}$	%EI.	RA
1	13	3.68	4.37	3.19	3.76	0.169	17.7	59.4%
2	21	3.87	4.62	3.24	3.91	0.120	22.9	64%
3	46	3.45	4.18	2.96	3.49	0.128	19.9	64.1%
5A	427	2.50	2.98	0.72	2.53	0.152	18.7	64.4%

EI. = Elongation to fracture; RA = Reduction in area

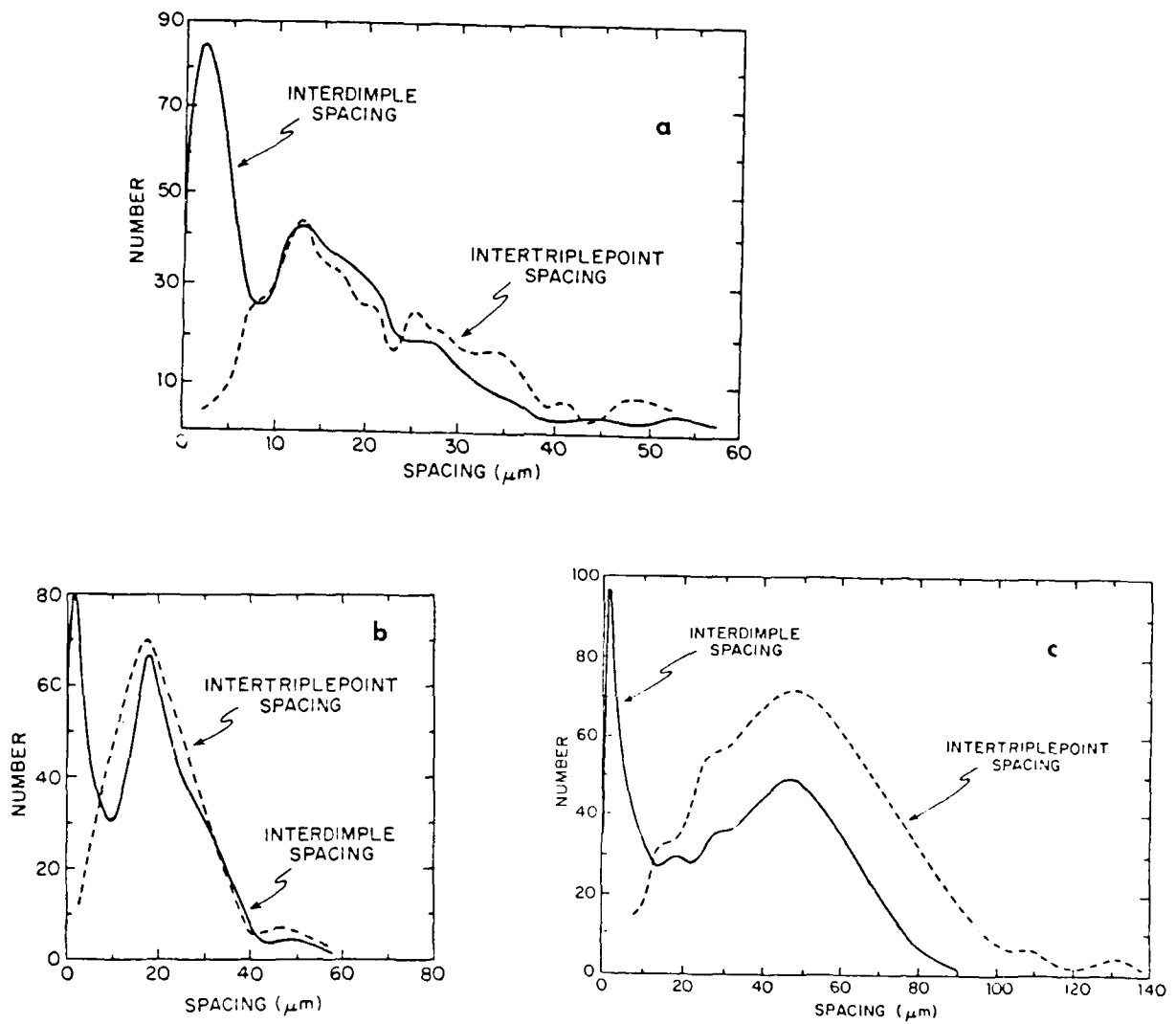


Figure 1. Comparison between the numbers of interdimple and intertriplepoint spacings for specimens with average grain sizes of 13, 21 and 46  $\mu\text{m}$  corresponding to specimen numbers 1, 2, and 3.



Figure 2. SEM fractograph of specimen #2 having an average grain size of  $21\ \mu\text{m}$ . Range of grain sizes from  $2$  to  $72\ \mu\text{m}$ . The bottom levels of dimples A, C and B are at  $10\ \mu\text{m}$ ,  $5\ \mu\text{m}$  and  $0$  base, respectively, as determined by stereo-photogrammetry. The ridge on the right of dimple B (arrow) is almost  $40\ \mu\text{m}$  higher than the bottom level of B.



Figure 3. SEM fractograph of specimen #7A with average grain size of 1,250  $\mu\text{m}$ . Note numerous dimples in the center area and grain boundary ledges at lower right. Range of grain sizes: 82  $\mu\text{m}$  to 2,150  $\mu\text{m}$ .

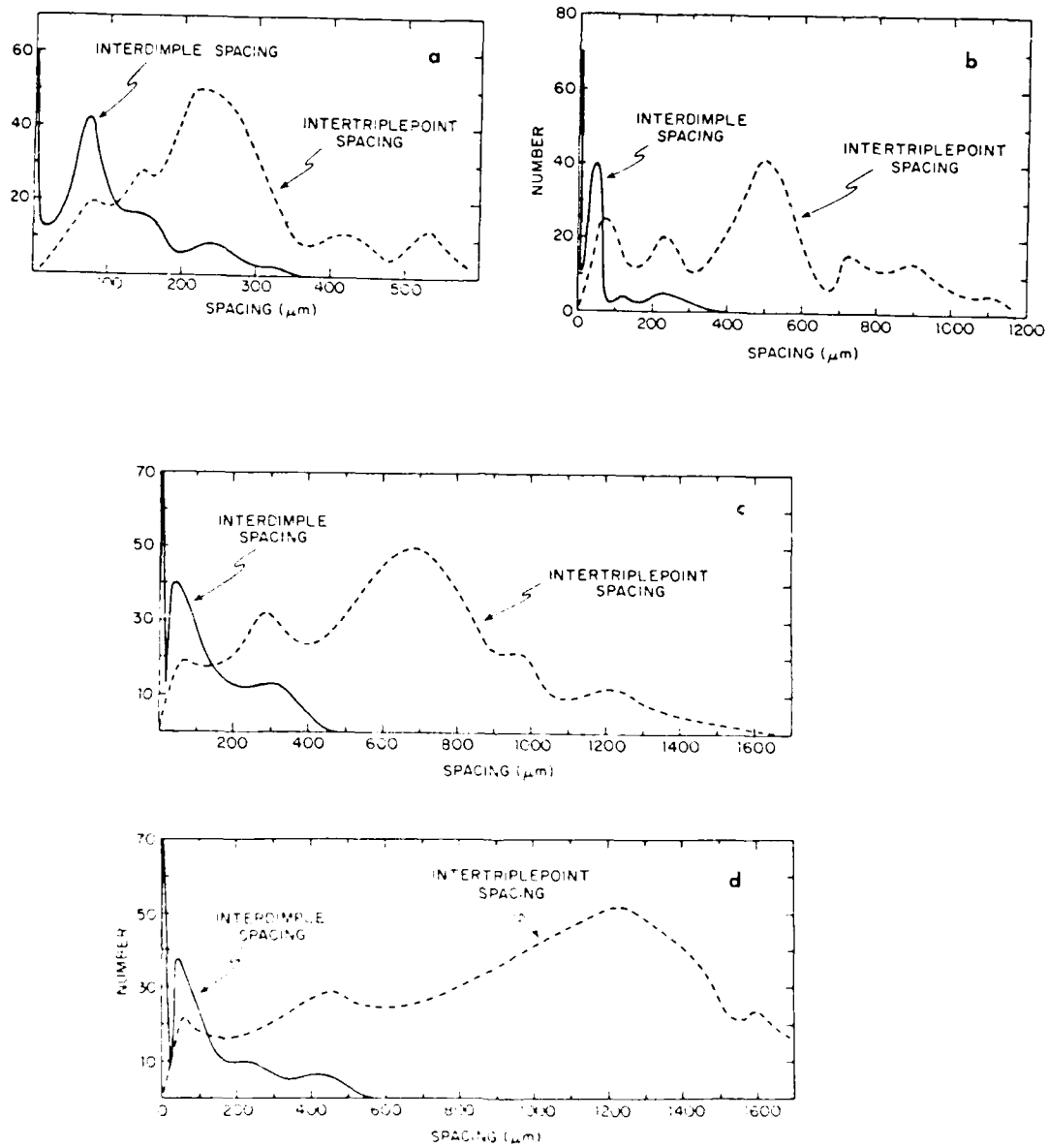


Figure 4. Comparison of frequency of interdimple and intertriple point spacings for four large grained specimens. Average grain sizes were 200, 427, 792, and 1,250  $\mu\text{m}$  corresponding to specimens 4B, 5A, 6 and 7A, respectively.

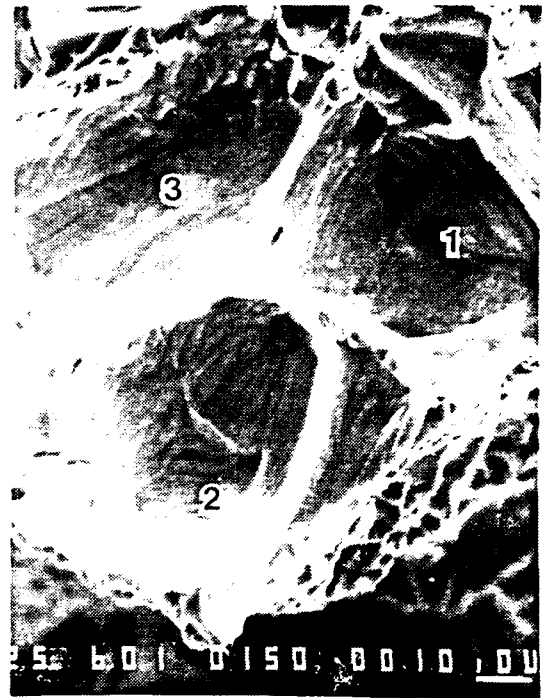
distinct mechanisms of void initiation.

The measurements displayed in Figure 1 and 4 were made from stereo-pairs. A simple addition to a flying spot stereo-microscope made it possible to draw topographical maps of fracture surfaces. An example is given for a rather simple fractograph, Figure 5, for which a stereo-pair is shown. The corresponding topographical map is given in Figure 6. While stereo-viewing conveys a distinct three-dimensional impression of the general layout of a fracture surface and also of individual dimple geometries, it would not have been possible to conceive the large difference between the lowest points of the dimples. The largest height difference measured in this micrograph amounts to 40.8  $\mu\text{m}$ . Dimple #1 has an average depth of 24  $\mu\text{m}$  while dimples #2 and #3 have average depths of 13  $\mu\text{m}$  and 10  $\mu\text{m}$ , respectively. The stereo-photogrammetry revealed not only that the dimple depths are different by larger amounts than what the eye had perceived but that the base surface is inclined, i.e., it increases from top right of Figure. 5 to bottom left. The even greater complexity of the topography in large-grained specimens is now appreciated and stereo pairs are essential for their evaluation.

For a complete evaluation of fracture surfaces, however, one has to go one step further. From the irregular features seen in all stereo-micrographs, one must draw the conclusion that the growth of voids depends on local stress conditions at a microstructural scale and consequently is anisotropic. Therefore, one can expect that matching fracture surfaces will look differently, and the drawing of contour maps has shown this convincingly. Figure 7a depicts a cut through contour maps of matching fracture surfaces. In order to classify the difference in the features of these matching surfaces, the vertical scale has been enlarged by a factor of five. The true profile for the "lower" surface is shown in Figure 7b.

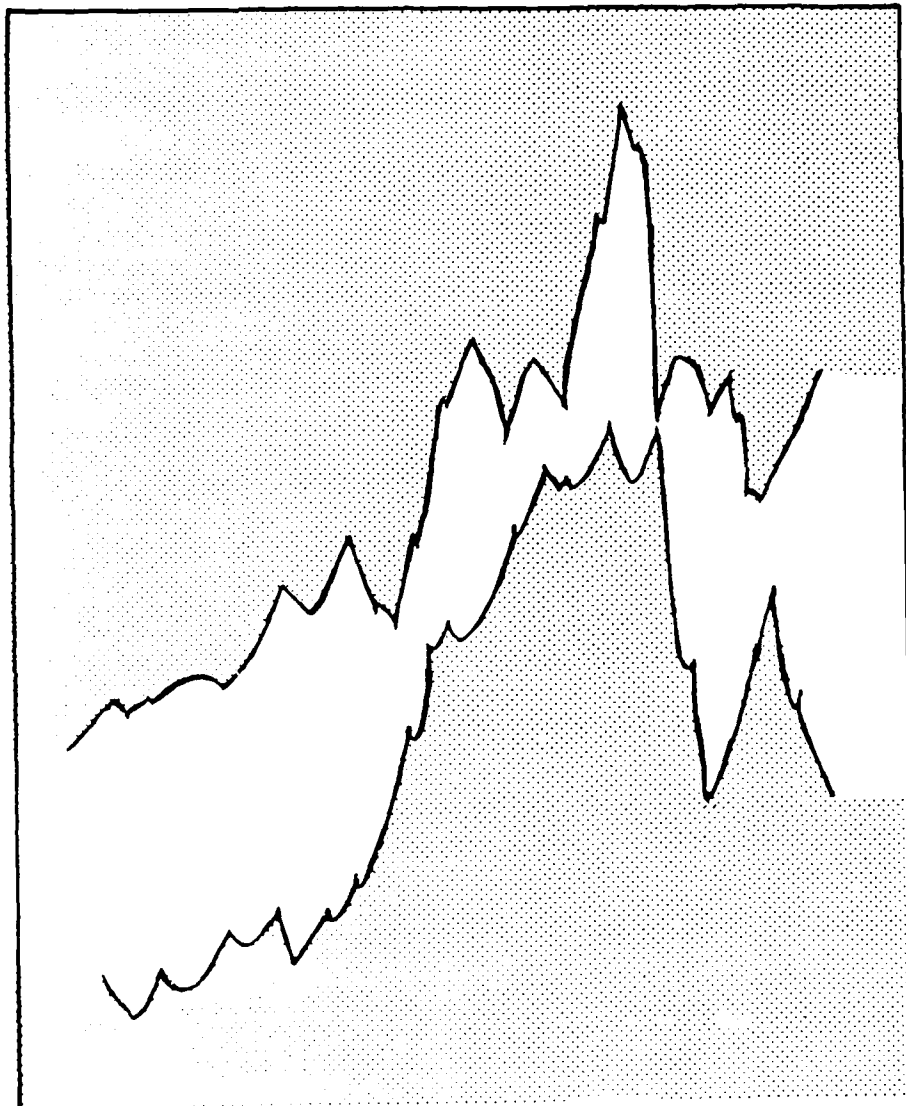
#### 4. DISCUSSION

The immediate problem is to rationalize the effects of grain boundary structures on void initiation. The dimple measurements show that there are two relationships between interdimple distances and intertriple point distances: one group with grain sizes below 50  $\mu\text{m}$  has





7(a).



7(b).

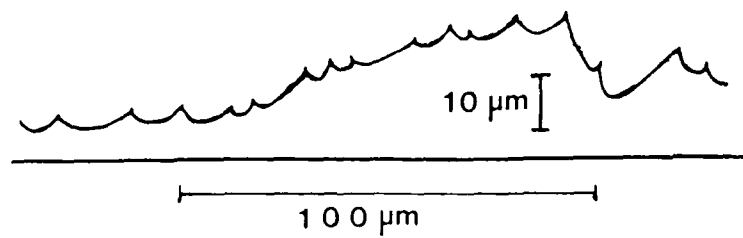


Figure 7(a) Upper and lower profiles of a cross-section of a fracture surface taken by SEM from specimen #3. Note differences between the two profiles. Vertical axis magnified by a factor of five. See lower profile at 7(b) for normal scale.

an almost perfect correspondence between these data points, while for another group with grain sizes above 200  $\mu\text{m}$  this relationship is not the dominating one.

Crack initiation at triple points is common in creep as first explored by Zener [13]; here grain boundary glide was involved and thereby a triple point becomes the obvious location for a stress concentration. Movement between grains along their boundary is not to be expected in titanium at room temperature. However, incompatibility stresses between grains [14] should be high at triple points. In-situ straining in a TEM showed that the first glide dislocations are often generated at triple points (see Figure 8 [15]), and slip lines have been seen to originate at triple points [16]. Recently Kurzydowski et al. concluded on the basis of in-situ TEM work in stainless steel that the emission of dislocations from a triple point occurs at a stress of  $G/320$ , with  $G$  the shear modulus [17]. These authors claim that the stress concentration factor of a triple point is not far from 2.8 [17,18]. All of this indicates that after extensive deformation, a triple point represents an exceptionally high local stress concentration in a polycrystalline material. In addition, it is known that impurities reduce the energy in grain boundaries [19] and this most likely applied to our case. The experimental result that grain boundary triple points have been the primary sites for void initiation is thus understandable. The question now to be treated is concerned with the observation that for specimens with grains larger than 200  $\mu\text{m}$  this does not hold.

Since the reduction in area for all specimens was 60% or higher, the plastic deformation in the neck was substantial. Titanium deforms at room temperature by prism glide,  $\{10\bar{1}0\} \langle 11\bar{2}0 \rangle$ , and by twinning on six planes [20]; the most frequently observed twins have  $\{10\bar{1}2\}$  and  $\{11\bar{2}2\}$  as composition planes. The influence of twinning on void initiation has to be included in our deliberations since it is well known that twinning plays an important role in larger grained titanium while deformation twins have not been seen in small grained titanium [21]. Mechanical twinning will occur in Ti for  $\{10\bar{1}2\} \langle 10\bar{1}1 \rangle$ , for example, by stresses in tension parallel to the c-axis and correspondingly for compression stresses perpendicular to it. That both types of stresses can act at grain boundaries cannot be doubted since

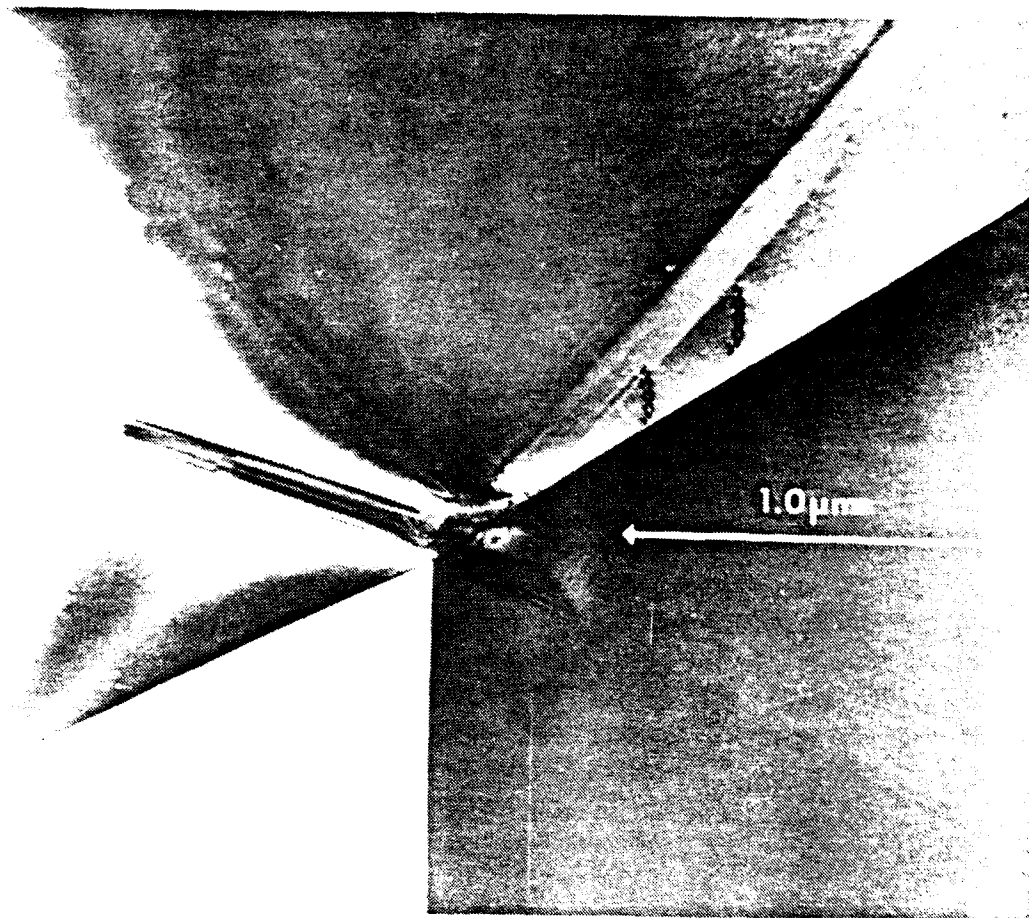


Figure 8. Initiation of first dislocations at triple point area upon straining at 304 stainless steel foil. In-situ TEM experiment [15].

after even modest strains, grain boundaries will have developed ledges, the stress fields of which have been calculated by Das and Marcinkowski [9]. Amateau et al. reported the occurrence of twins in  $\alpha$ -Ti ( $O_2 = 0.25\%$  as compared to our  $O_2 = 0.102\%$ ) after a strain of 4.8% for specimens with grain sizes comparable to our specimen #4 [22]. These authors identified "thick" twins as  $\{10\bar{1}2\}$  and  $\{11\bar{2}2\}$  types and "thin" twins of  $\{11\bar{2}x\}$  types with  $x = 1, 3, \text{ or } 4$  (second order twins) in accordance with the findings of Rosi et al. [23]. The second order twins were seen in the  $\{11\bar{2}2\}$  twins and the crack nucleation occurred between second order twins and matrix based on observations by light microscopy at  $180^\circ\text{K}$ . Figure 9 shows a fracture surface in support of this mechanism. In stereo-viewing one can see a fine ridge structure with a spacing of a few micrometers lying within larger bands  $10 \mu\text{m}$  to  $30 \mu\text{m}$  wide. The latter fit the description of the "thick"  $\{11\bar{2}2\}$  twins and the finer lamellae the secondary twins. A grain boundary is indicated by arrows. Intergranular fracture obviously has produced the relatively flat area marked A. Arrows B are pointing to two deep microcracks. While Figure 9 represents an extreme case of crack initiation by twinning processes, Figure 10 is indicative of slip and twinning which are both present in areas about a few hundred micrometers across where void initiation by glide and initiation of microcracks by twinning operated in close proximity in grains between  $200$  and  $1,300 \mu\text{m}$ .

In Figure 11 we have plotted the maxima of interdimple spacings against grain size and one can see that the interdimple spacing follows the grain size for the grains and then levels off regardless of grain size. All measurements of interdimple spacings have been made from only those areas of fracture surfaces which showed full ductility. As seen from Figure 4, the broad distribution of dimples is not uniform but shows in addition to the maximum of about  $50 \mu\text{m}$  a number of smaller peaks. The same is true for the intertriple point spacing with its maximum near the average grain size. It should be noted that for the four grain sizes (Figure 4) a small peak of intertriple point spacings coincides with a peak of interdimple spacings. Again the indication is that triple points remain important void initiation sites. However,



Figure 9



Figure 10

Figure 9 SEM micrograph indicative of primary and secondary twinning  
 (A) and (B) are feature initiation.

Figure 10 SEM micrograph showing ridge structures due to twinning  
 at a glide. A reasonable smooth surface (i.e. without  
 dislocations) almost perpendicular and indicates a brittle  
 segment of the fracture process; this plane is indicated  
 between arrows.

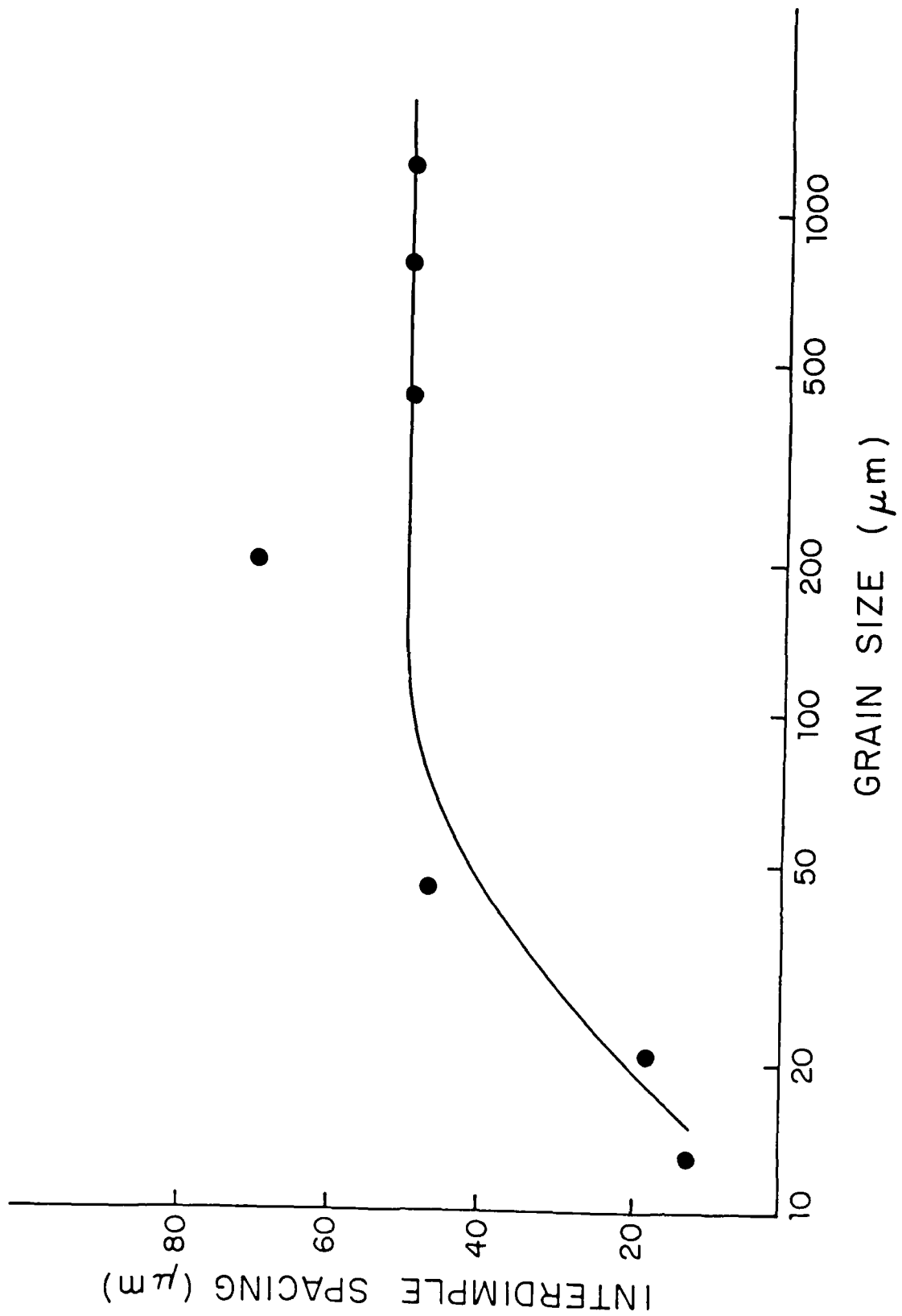


Fig. 11. Relationship between interdimple spacings and grain size.

other void initiation processes are now more competitive. Besides initiation sites at grain boundary ledges and secondary twin-matrix intersections, other processes must have been active. The "bend plane" mechanism is normally cited as an important crack nucleation model for hexagonal crystals but is not applicable for highly strained polycrystalline Ti since that mechanism is based on bicrystal studies in zinc at low temperatures where cracks appeared parallel to the basal plane after elongations to fracture of only 0.5% to 2.8% [12]. All of our samples showed multiple glide in the necked region which means that extensive glide was produced by a number of glide systems crossing each other. Microcrack initiation at slip intersections in close packed crystals has been considered as one of the most important void initiation mechanisms [10], and it is proposed that this mechanism also participates in polycrystalline Ti. The significant peak for interdimple spacings in Figure 4 is consistently at or near 50  $\mu\text{m}$  in larger grain size material and gives credence to a glide crossing mechanism for prime void initiation sites for large-grained Ti.

Close inspection of SEM fractographs shows that the largest number of voids grows only to a diameter of about 1  $\mu\text{m}$  as documented by the highest peaks for interdimple spacings in Figures 1 and 3. Earlier work on the initiation of microcracks in heavily workhardened metals and alloys [25,26,27,28,29] pointed to the importance of dislocation cell walls for microvoid initiation. This is exactly the situation in the micro-ligaments between the large voids discussed so far. Here  $\epsilon > 1$  on account of the continuous reduction in thickness of the micro-ligaments to a few micrometers. A detailed description of microvoid initiation and growth has been given elsewhere [30]. The microdimples under discussion are seen primarily on the rims of larger dimples and indicate areas where localized rupture has taken place.

A determination of the profile of a dimpled fracture surface can provide information as to the precise sequence of void initiation, provided the resolution of the technique is high enough to discern the relationships between dimples for the two opposite fracture surface profiles. The profiles in Figure 7 have been evaluated for a time sequence by first "closing" the fracture, i.e., moving the upper and lower profiles over each other so that no white areas remain; then

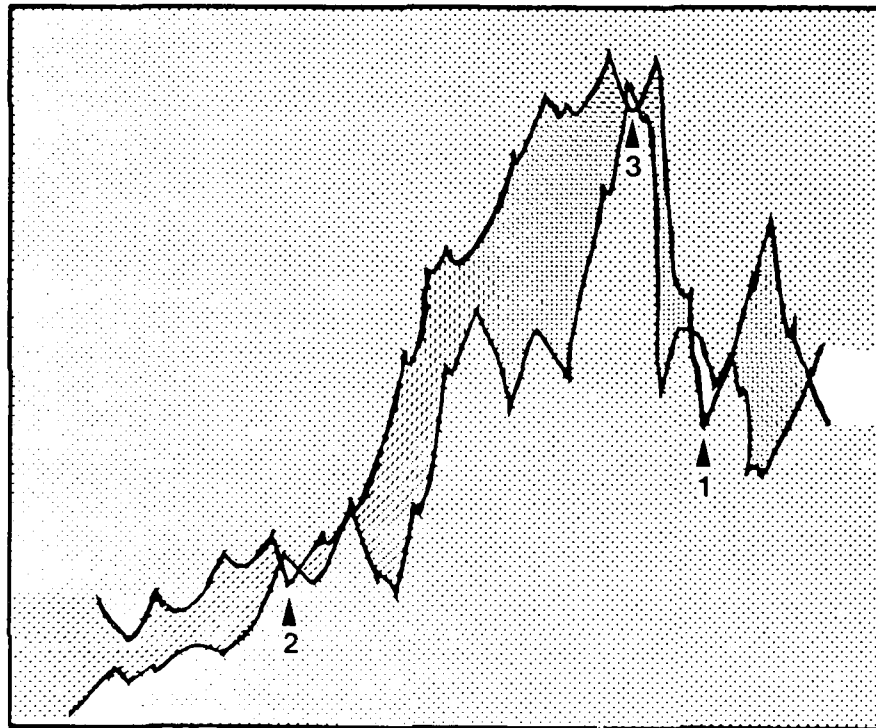


Figure 12. Use of fracture surface profiles for determining void initiation time sequence. Vertical axis magnified by a factor of five for clarity.

moving the profiles apart, one can monitor the initiation sequence (see Figure 12 for the appearance of initiation of voids [1-3]). Measuring the whole sequence of 16 initiation sites yields an average distance between sites of nearly 10  $\mu\text{m}$ . With an average grain size of 13  $\mu\text{m}$  in this specimen the claim of triple points as primary initiation sites (see Figure 1) is verified within the error limits. This determination was made under the assumption that void growth is proportional to time, and that the profile would be going through the center of the dimples which is, of course, not fulfilled. A more careful analysis would involve profiling at close intervals which, if done for a larger part of the fracture surface, would contribute to the quantitative topographical characterization of the time sequence of void initiation. This measurement is adding the dimension of time to the study of voids in fracture surfaces at microscopic resolution for the first time.

#### 5. CONCLUSIONS

- (a) In specimens up to grain sizes of 50  $\mu\text{m}$ , grain boundary triple points are primary void initiation sites.
- (b) When grain sizes range between 200  $\mu\text{m}$  and 1,300  $\mu\text{m}$  additional void initiation sites are provided by twin intersections, glide band intersections, dislocation interactions with grain boundaries, and grain boundary ledges.
- (c) Microvoids are seen at the rims of dimples and between dimples; they are due to initiation at dislocation cell walls and occur during rupture at the final separation.
- (d) The time sequence of void initiation can be derived from fracture surface profiles which were constructed from quantitative topographical information.
- (e) It has been demonstrated that quantitative stereo-photogrammetry for the characterization of fracture surfaces is mandatory.

## REFERENCES

1. D. Brock, Eng. Fract. Mech. 5 (1973) 55.
2. J.D. Boyd and R.G. Hoagland, in Titanium Science and Technology, Plenum Press, NY (1973) pp. 1071.
3. J.N. Greenwood, D.R. Miller and J.W. Suiter, Acta Metall. 2 (1954) 250.
4. R.D. Gifkins, Acta Metall. 4 (1956) 98.
5. H.C. Chang and N.J. Grant, Trans. Met. AIME 206 (1956) 545.
6. C. Zener, in Fracturing of Metals, ASM, Metals Park, Ohio, 1948, p. 3.
7. A.N. Stroh, Phil. Mag. 3 (1958) 597.
8. J.J. Gilman, Trans AIME 212 (1958) 783.
9. E.S.P. Das and M.J. Marcinkowski, J. Appl. Phys. 45 (1972) 4425.
10. A.S. Argon and E. Orowan, Nature 192 (1961) 447.
11. D. Hull, in Fracture of Solids, Wiley, NY, 1963, p. 417.
12. J.J. Gilman, Trans AIME 200 (1954) 621.
13. C. Zener, Elasticity and Anelasticity in Metals, Univ. Chicago Press, Chicago, IL, 1948, p. 158.
14. J.P. Hirth, Met. Trans. 3 (1972) 3047.
15. H.G.F. Wilsdorf, Structure and Properties of Thin Films, Wiley and Sons, New York, NY, 1959, p. 151.
16. R. M. Douthwaite and G. T. Evans, Acta Metall. 21 (1973), 525.
17. K.J. Kurzydowski, R.A. Varin and W. Zielinski, Acta Metall. 32 (1984) 71.
18. K. Kurzydowski, Z. Celinski and M.W. Grabski, Res Mechanica 1 (1980) 283.
19. B. Ralph, R.C. Ecob, A.J. Porter, C.Y. Barlow and N.R. Ecob, Deformation of Polycrystals: Mechanisms and Microstructure, Riso Ntl. Lab., Roskilde, Denmark, 1981, p. 111.
20. P.G. Partridge, Metall. Rev. #118 (1967).

21. W. Truszkowski, A. Latkowski and A. Dziadon, Deformation of Polycrystals: Mechanisms and Microstructure, Riso Natl. Lab., Roskilde, Denmark, 1981, p. 383.
22. M.F. Amateau, W.D. Hanna and E.G. Kendall, AF Rep. SAMSO TR-71-268 (1971).
23. F.D. Rosi, C.A. Dube and B.H. Alexander, Trans, AIME 197 (1953) 257.
24. F.D. Rosi, Trans AIME 200 (1954) 58.
25. R.N. Gardner, T.C. Pollock and H.G.F. Wilsdorf, Mater. Sci. Eng. 29 (1977) 169.
26. T.C. Pollock, Ph. D. Dissertation, U. Virginia, Charlottesville, VA 1977.
27. R.N. Gardner and H.G.F. Wilsdorf, Metall. Trans. A, 11 (1980) 653.
28. R.N. Gardner and H.G.F. Wilsdorf, Metall. Trans A, 11 (1980) 659.
29. H.G.F. Wilsdorf, Mater. Sci. Eng. 59 (1983) 1.
30. H.G.F. Wilsdorf, ZS. Metallkd. 75 (1984) 154.



SECTION III  
THE EFFECT OF THERMAL-MECHANICAL COUPLING  
AT THE HEAD OF A RAPIDLY LOADED CRACK TIP

Based on a Ph.D. Thesis (Materials Science) by J. Daniel Bryant, UVA, 1987\*

ABSTRACT

An analytical method has been developed to quantify the effect of deformational heating in the near crack tip region of a material subjected to rapid loading. The finite element method (FEM) has been employed to model the changes in the stress and strain fields near the crack tip due to the effects of strain induced temperature rises for a material undergoing elastic-plastic behavior. The effects of these temperature rises are manifested in both altered material properties, i.e. thermal softening, and in thermal expansion. The dynamic interaction between the evolving stress, strain, and temperature fields incurred during rapid loading is approximated by dividing the loading history into discreet steps. By using the nodal displacements and elemental temperatures developed in the previous load step as initial conditions for the subsequent step the model emulates the true thermal-mechanical coupling experienced during shock loading.

Comparison of the stress and strain fields of the thermal-mechanically coupled and uncoupled models has shown the effects of temperature rise to be present well in advance of the crack tip; significant effects include diminished maximum stress and increased maximum strain in the coupled model. By incorporating the results obtained from instrumented test specimens used in the determination of loading parameters, insights have been gained into the effects of nonadiabatic conditions and the applicability of the method to the case of the propagating crack.

\*Now at Martin-Marietta Research Laboratories, 1450 South Rolling Road, Baltimore, MD 21227



## TABLE OF CONTENTS

	<u>Page</u>
1. INTRODUCTION .....	39
2. THEORETICAL AND EXPERIMENTAL PROCEDURE .....	41
(i) Experimental Method .....	41
(ii) Modeling Method .....	42
(a) The Uncoupled Model .....	51
(b) The Coupled Model .....	51
3. RESULTS AND INTERPRETATION .....	51
(i) Analysis of Stress and Strain Fields .....	52
(ii) Transient Thermal Analysis .....	58
(iii) Predicted Temperature Field .....	58
(iv) One-Dimensional Transient Thermal Analysis .....	61
4. CONCLUSIONS .....	65
REFERENCES .....	66



## THE EFFECT OF THERMAL-MECHANICAL COUPLING AT THE HEAD OF A RAPIDLY LOADED CRACK TIP

### 1. INTRODUCTION

Deformational heating has long been acknowledged as having a significant influence on the process of dynamic fracture. Early works by Zener and Hollomon describing the effect of strain rate on plastic flow in steel elucidate the opposing roles played by the well known phenomenon of strain rate hardening and that of thermal softening as a result of adiabatic heating. More recent works have concentrated on the effects of the instability reached when adiabatic softening dominates the fracture process. The formation of adiabatic shear bands in metals discussed by Rogers in his review and by Stelly et al and others in the field is associated with the instability dictated by the slope of the adiabatic stress-strain curve. Evidence of rapid temperature rises during adiabatic heating has presented itself in the form of transformation bands and incipient melting of the fracture surface. Figure 1 shows such a heat affected area on the fracture surface of a beta titanium alloy subjected to high strain rates.

A detailed numerical model of the propagation of adiabatic shear bands was recently accomplished by Kuriyama and Meyers [1]. In their analysis, the region ahead of a crack is modeled for a material obeying an adiabatic stress-strain relation and subjected to pure shear (Mode II) stresses. In concentrating on the near crack tip region, the model is thus analogous to the approach of fracture mechanics. The case of a crack tip experiencing a Mode I type opening stress was addressed by Hoff, Rubin and Hahn [2]. A compact tension specimen subjected to dynamic loading was modeled using finite element analysis (FEM); the results describe the changes in the stress and strain fields produced by strain rate sensitive and insensitive materials. The model, however, did not account for the effects of adiabatic heating in the rapidly strained region at the crack tip.

In the present study, the stress and strain fields at the crack tip in a compact tension specimen are calculated for the case of deformation dominated by adiabatic heating effects. To address the problems of strain rate sensitivity, an experimental testing program has been run in parallel and thus acts to supply the parameters needed to describe both the material response to accelerated deformation rates and the loading

(a)

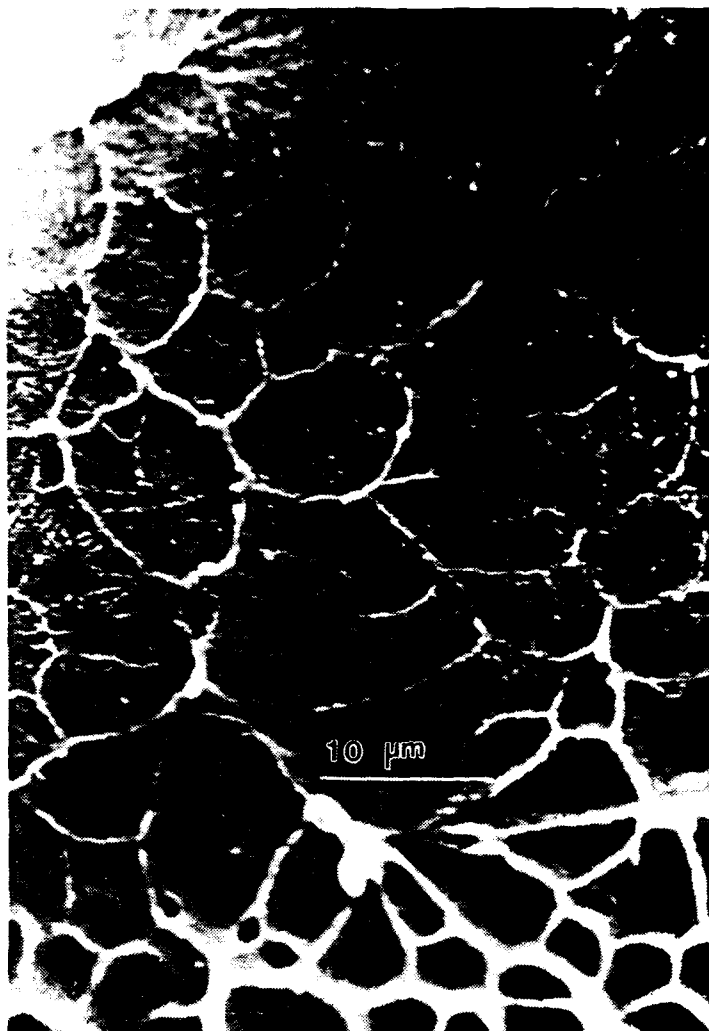


Figure 1a. The change in dimple structure as the shear lip is approached is shown in this micrograph. The dimples on top are seen to become shallower and more Mode I in character.

(b)

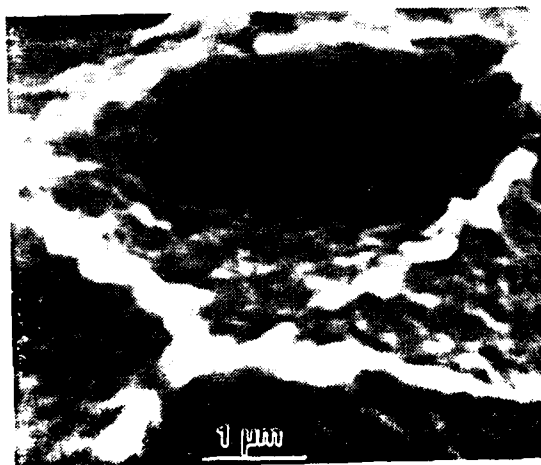


Figure 1b. The globularized, "knobby" features within the fracture surface, associated with rapid temperature rise at fracture, are shown in detail.

history for the specimens being modeled. Two manifestations of adiabatic heating on the stress-strain distribution are considered: thermal softening and thermal expansion. The effects of the dynamic interaction of the stress, strain and temperature fields are determined for an elasto-plastic temperature dependent material using the finite element method. In this approach, the thermal-mechanical coupling relating these three fields is determined by the modulation of the elemental temperatures at discrete intervals, these temperatures being determined by heat generated through plastic deformation. By studying a rapidly loaded stationary crack undergoing adiabatic heating, the stress and temperature fields derived can be used to predict the response of more complicated systems, including the nonadiabatic case and that of the propagating crack.

## 2. THEORETICAL AND EXPERIMENTAL PROCEDURE

### (i) Experimental Method

Specimens for tensile and  $K_{Ic}$  tests were machined from a billet of Ti-10V-2Fe-3Al of the composition given below.

Table 1: Chemical Composition (weight percent)

C	N	Fe	V	O	Al	Y	Ti
.03	.013	1.8	9.9	.095	3.4	10 ppm	balance

Specimens were homogenized above the beta transus temperature at 825°C. This was followed by a furnace cool to 780°C and a quench to room temperature water. A subsequent aging treatment was performed at 500°C for one hour.

Fracture toughness tests were made through  $K_{Ic}$  testing of compact tension and three point bend specimens. Testing was performed on a closed loop hydraulic testing unit. As the loading rates used in these experiments were far higher than could be recorded using pen and chart, a high speed data acquisition system was developed. The load signal was recorded using an ATT 6300 computer at intervals determined by the on-board clock. To determine the exact moment of crack propagation (and hence the load at the onset of crack motion) a strain gage was cemented directly ahead of the pre-crack and the signal monitored using the same

equipment. In this way, the fracture toughness  $K_{IC}$  could be determined as well as the loading rate parameter  $\dot{K}_1$  where  $\dot{K}_1 = K_{IC}/t_c$  and  $t_c$  is the critical time to reach crack growth. Loading rate was varied from  $1.5 \text{ MPa}\sqrt{\text{ms}}^{-1}$  to  $1.28 \times 10^4 \text{ MPa}\sqrt{\text{ms}}^{-1}$ . The data recorded provided the required loading history used in the finite element model developed. The same data acquisition system was used to measure crack propagation speed; using a crack propagation gage (an array of parallel conductors) the resistance drop was measured as the advancing crack severed the gage. The instrumented compact tension specimens, as well as instrumented tensile specimens used in high strain rate tests, are shown in Figure 2.

(ii) Modeling Method

The finite element method (FEM), a system of mathematical modeling which, for static stress problems, determines the displacements of the nodes contained within the element mesh in response to forces and displacements impressed upon that mesh as boundary conditions. The mesh is constructed by the user to emulate the geometry of the system to be analyzed. In this analysis, the stress and strain fields near the crack tip in a compact tension (CT) specimen were modeled with the aid of the ANSYS finite element codes [3]. This mesh configuration was chosen for two reasons. First, the stress field near the crack tip of such a specimen has been extensively studied; this allows for comparison of the current model results with previous work. Secondly, by performing mechanical tests upon specimens of this same configuration, the parameters of the model, namely the loading history and the time indicating the onset of crack growth, can be determined directly from experimentally measured quantities.

In the present work, a four noded isoparametric stress solid was chosen as the element type. This two-dimensional model was made to emulate a three-dimensional model of unit thickness undergoing plane strain. A diagram of the element mesh is given in Figure 3. The load is applied at the node marked in the upper left portion of the diagram; this corresponds to the center point of the load pin in the actual CT specimens. As shown, the direction of crack propagation is to the right. As is standard in finite element analysis, the total specimen being modeled is divided along its lines of symmetry and a single

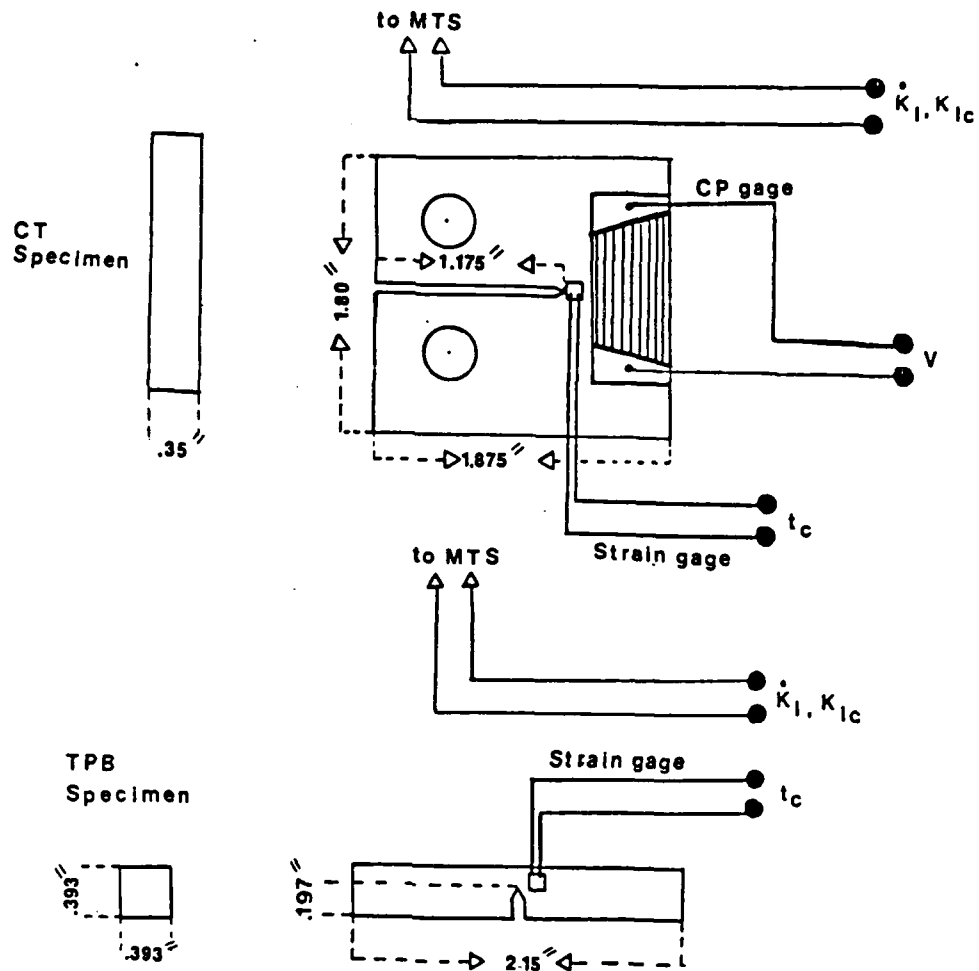


Figure 2a. Specimen configurations used for fracture toughness testing by  $K_{Ic}$  determination. The upper diagram shows the specifications of the compact tension (CT) specimens, while the lower shows that of the three point bend (TPB) specimens. In each diagram, the instrumentation used to obtain experimental parameters is shown on the right.

**Tensile Specimen**

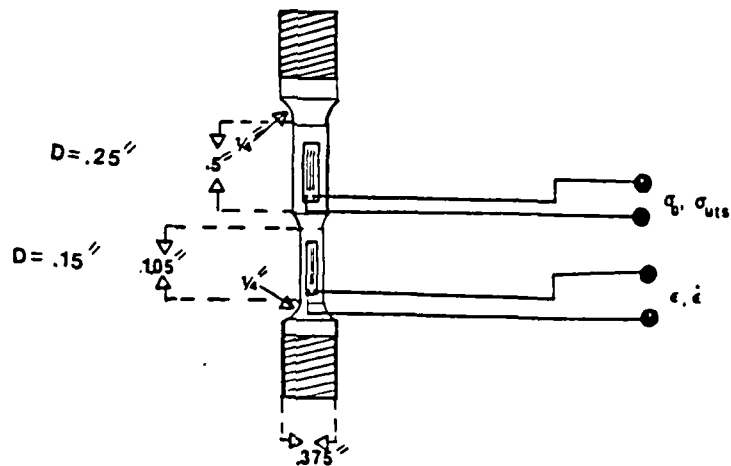


Figure 2b. Specimen configuration used in tensile tests. The double gage design allows for the determination of stress acting on the specimen without the use of a load cell.

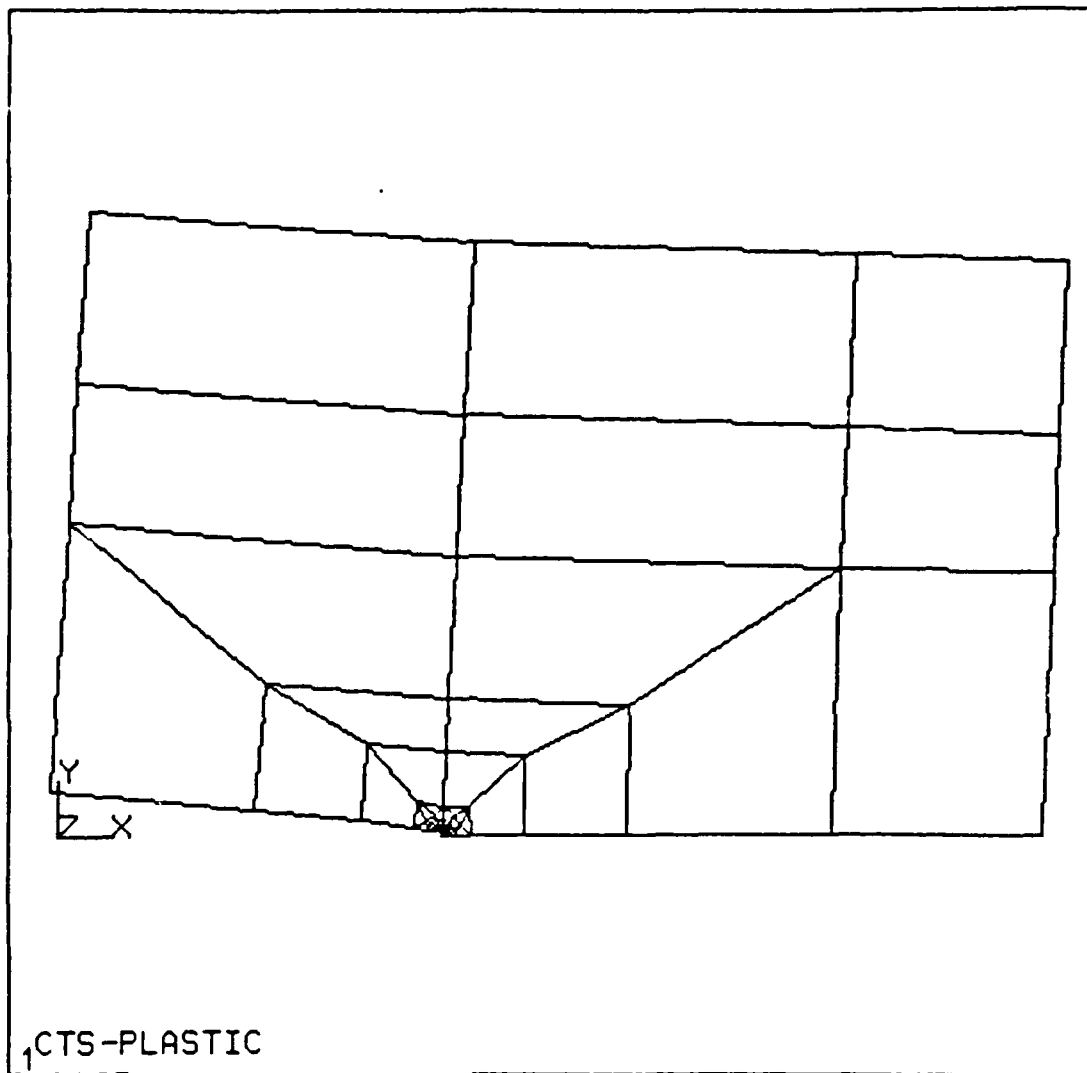


Figure 3. The element mesh used to model the rapid loading of a compact tension specimen. The load is applied at the node marked, and the crack is to propagate to the right. Only the upper half of the CT specimen is modeled, due to symmetry.

section analyzed. The line of symmetry in this problem is along the line  $Y=0$ , which includes the crack tip itself. To preserve the equilibrium of the mesh in response to the loading force, displacement constraints are placed upon the series of nodes along the X axis to the right of the crack tip. The mesh generated consists of 144 nodes forming 125 elements. In the region close to the crack tip, the density of the elements increases, as it is here that the greatest stress gradients will occur. An enlargement of the near crack tip region is shown in Figure 4, with the nodal numbers marked. Concentric semicircles surround the crack tip itself (node 1) providing an elemental spacing of one micron directly next to the crack tip, which is represented in this model as sharp and unblunted.

The compliance of the element mesh in response to an external force or imposed displacement is translated into nodal displacements via the stiffness matrix. The stiffness matrix incorporates the material properties; for the elasto-plastic model developed here a bi-linear stress-strain curve was used to describe the alloy's mechanical properties, as shown in Figure 5. The temperature dependence of the elastic and plastic portions of the lower stress-strain curves in Figure 5 is approximate and based upon empirical data taken from another titanium alloy for which high temperature data was available, namely Ti-6Al-4V.

A single nodal force, situated at node number 82, acts in the vertical direction, thereby simulating the action of the load pin in the actual specimen. The maximum load applied at this node was determined from one of the  $K_{IC}$  tests run at a loading rate near the center of the range studied. In both the coupled and the uncoupled model, this load is applied in discreet load steps; the maximum load is applied over a series of 10 steps. There are two reasons for this. Firstly, by its very nature, a problem incorporating plasticity is nonlinear; the solution, therefore, can only be arrived at through a process of iteration. By dividing the total load into a series of steps, the problem of nonconvergence may be avoided. The second reason lies in the method used in the thermal-mechanically coupled model to produce a dynamic interaction between the elemental temperature and the stress and strain fields. Incrementing the load to the maximum load over ten steps

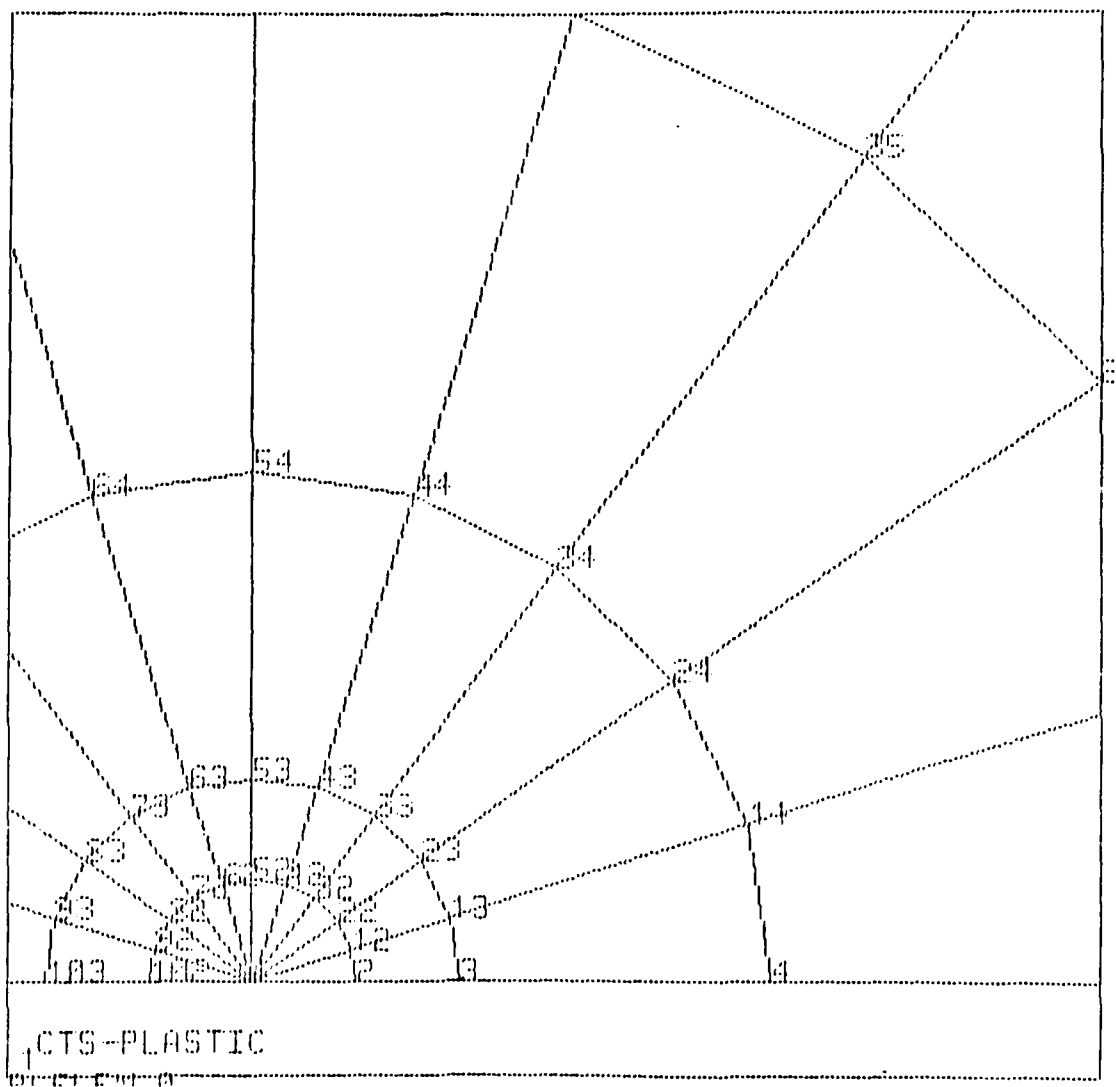


Figure 4. The near crack tip region of the element mesh. The density of the elements increases, as the stress gradients near the crack tip will be higher.

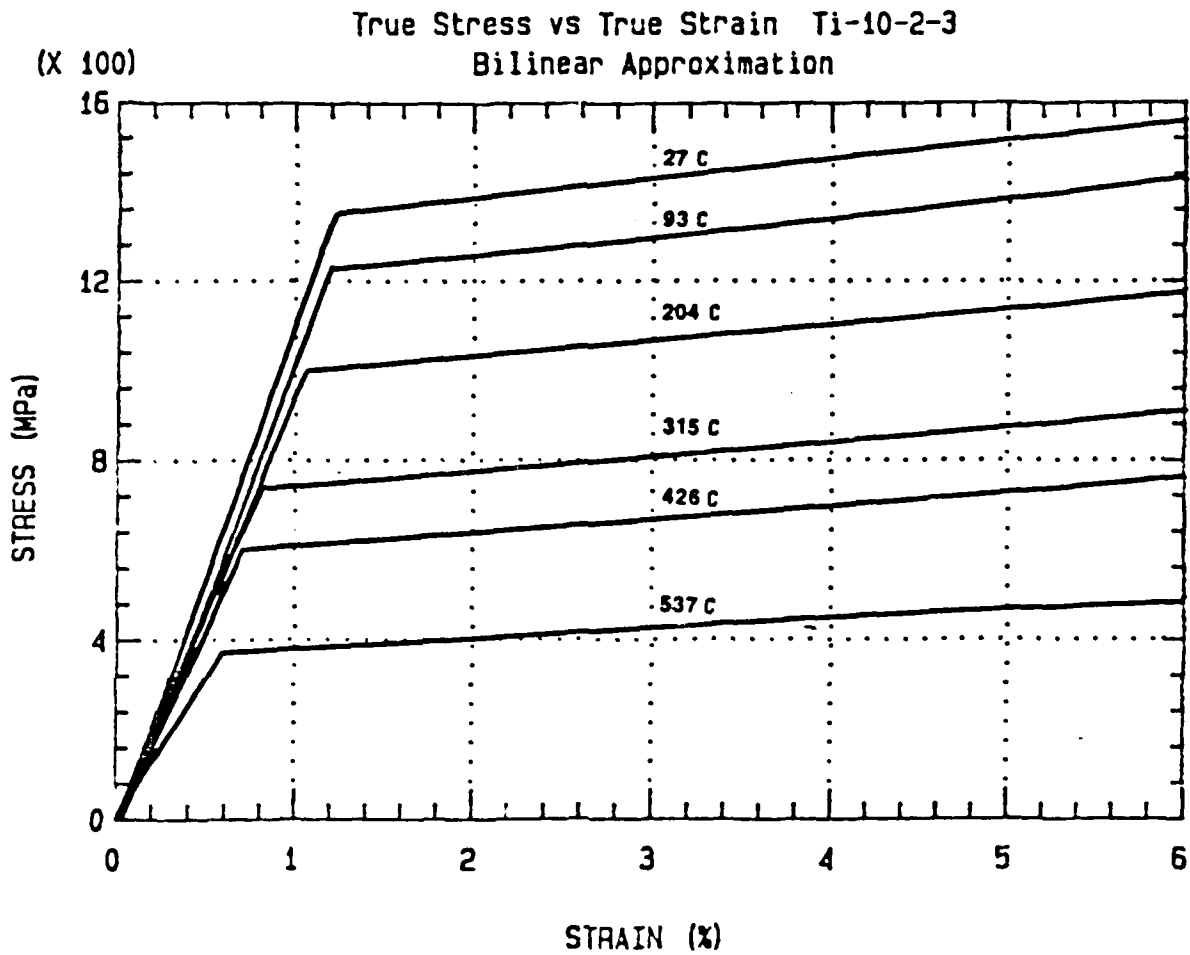


Figure 5. The bilinear stress - strain curves used to describe the compliance of Ti-10V-2Fe-3Al at elevated temperatures.

allows for the periodic adjustment of the elemental temperatures, as determined by the plastic strain energy expended in the previous load step.

The number of iterations required to reach a particular margin of error within a load step is controlled in the program through a convergence criterion. For a stress solid element type, the convergence criterion is defined by the ratio:

$$C = \Delta \epsilon_p / \epsilon_e$$

where  $\epsilon_e$  is the elastic strain and  $\Delta \epsilon_p$  is the change in the plastic strain with the previous iteration. Obviously, the smaller the convergence criterion set, the greater precision with which the model will simulate a material described by a given elasto-plastic stress-strain curve. The disadvantage lies in the greater computational time and expense for this added precision. A convergence criterion of  $C = .05$  was chosen in both models. Depending on the load step, between 5 and 20 iterations were required to match this criterion.

As stated in the introduction, the deformation induced heating in an element near the crack tip acts to change the defined temperature of the element involved, and this in turn affects the relationship of the stress and strain. At this point the method used to determine the temperature rise and the effects of that temperature rise will be discussed.

While a formal, analytical expression relates the stress and strain in an elastic material to the stored energy per unit volume, this expression is not exact for the case of an elasto-plastic material because of the path dependence of the integral. In a plastically deforming material, the stored energy per unit volume is approximated by the expression:

$$\Delta E = \int_{\epsilon}^{\epsilon_f} \sigma d\epsilon$$

where  $\epsilon_y$  and  $\epsilon_f$  are the yield strain and fracture strain respectively. The associated temperature rise within this element is given by:

$$\Delta T = \frac{R}{\rho c} \int_{\epsilon_y}^{\epsilon_f} \sigma d\epsilon$$

where  $C$  is the specific heat,  $\rho$  is the density and  $R$  is the proportion of energy converted directly to heat. From previous works,  $R$  is generally accepted to have a value between .90 and .95. This equation cannot be used analytically to describe the temperature rise for a material undergoing plastic deformation given the path-dependent nature of plastic deformation. Because of this, only an approximate relation can be made between the stress and plastic strain acting in an element and the energy expended per unit volume. The actual amount of energy expended is of course dependent upon the size of the element; a larger amount of energy will be expended in deforming a larger element. This problem of determining elemental volume (actually, elemental area with a given unit thickness) can be avoided by directly determining the temperature rise within each element. As the density and specific heat are both on a per unit basis, the volume of a given element is not required for establishing the elemental temperature. The plot shown in Figure 6 shows graphically the method used to determine the elemental temperature rise. An approximation is made that the area beneath the stress-plastic strain curve is described by a rectangle with an area equal to the product of the stress and plastic strain. The area beneath this curve, as well as the similar curves for stress and plastic strain acting in the  $Y$  and shear directions, is equated to the energy per unit volume expended in the action of plastic flow. The associated temperature rise within an element is given by the equation:

$$\Delta T = \frac{1}{\rho c} \left| (\sigma_x \epsilon_{px}) + (\sigma_y \epsilon_{py}) + 2(\sigma_{xy} \epsilon_{pxy}) \right|$$

where the absolute value functions have been employed to account for the positive, scalar nature of the heat generation.

The elemental temperatures for those elements inside of the elasto-plastic boundary are defined using the above equation at 10 points during the loading history, i.e., the final iteration of the 10 load steps. The subsequent load step is affected by this modulation of elemental temperatures in two ways. First, the appropriate

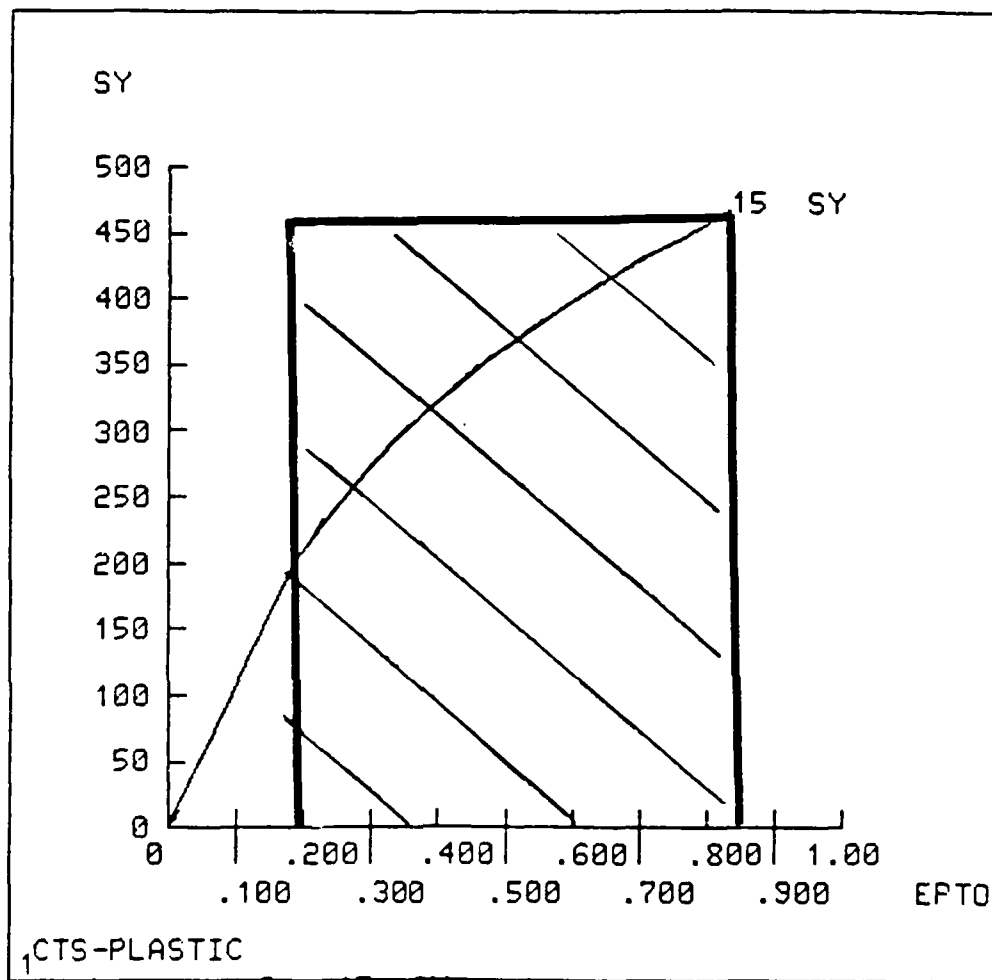


Figure 6. The method used to determine the heat generation within an element is shown graphically in this diagram. The area beneath the stress-plastic strain curve was approximated by the area of the shaded rectangle.

stress-strain curve will be selected for an element at that defined temperature. Secondly, the thermal expansion of that element will be incorporated, and this will be reflected in the stress and strain values for that element and those neighboring it.

(a) The Uncoupled Model. In the uncoupled model, the elemental temperatures are maintained at a constant, ambient temperature of 300°C throughout the loading history. This temperature was set in the pre-processing stage of the analysis, and as a result the material properties relating the imposed loads to the nodal displacements are prescribed by the upper most curve in Figure 5.

(b) The Coupled Model. In the coupled model, the requirement imposed by the modulation of the elemental temperatures at the end of each load step necessitates a different approach than that used for the uncoupled model. The first load step applied is identical to that of the uncoupled model, and in the subsequent load steps the load is applied to element mesh using the nodal displacements and stresses from the previous step as initial conditions. In the coupled model the elemental temperatures are adjusted for each element subjected to plastic strain in the previous load step. This process is repeated at the end of each load step. With the iterations required to reach a convergence criterion of .05, a total number of 192 iterations with a running time of approximately eight hours was required.

### 3. RESULTS AND INTERPRETATION

The objective of performing this analysis was to gain insight into the role which deformation induced heating plays in dynamic fracture. Specifically, there are two subjects which are to be addressed. The effect of thermal-mechanical coupling at the crack tip on the stress and strain fields is to be discussed. In addition, an associated temperature field is predicted under the assumption of adiabatic deformational heating. In the model, adiabatic boundaries are imposed between elements; no transfer or heat is permitted away from the crack tip area. The adiabatic temperature field predicted by the model can then be analyzed from the standpoint of transient heat generation and heat transfer.

The nodal displacements determined from the analysis are used to

predict the elements of the stress and strain matrices at each node. In addition, the stress and strain values of the four nodes defining the perimeter of an element can be averaged to yield the elemental, or centroidal, stresses and strains. The stress and strain data, as well as temperature profiles, are graphically presented in the form of connected contour plots determined from centroidal values.

(i) Analysis of Stress and Strain Fields

In the first set of plots, Figures 7 and 8, the plastic strain in the Y, or vertical, direction is compared for coupled and uncoupled models. The higher values of plastic strain in the thermal-mechanically coupled model are reflected in the difference in maximum plastic strain: 19.5% for the uncoupled model as compared to 26.6% for the coupled model. The higher plastic strain levels reached in the coupled model are a consequence of the thermal softening in the near crack tip region. The perimeter of the plastically deformed region, or the elasto-plastic boundary, can be interpolated from the stress-data printout. For both models, plasticity is seen only to occur within the fifth semi-circular regime of elements; this defines an approximate plastic zone radius of 42 micrometers. This is in good general agreement with the plastic zone radius defined by Dugdale for the plane strain case, given by:

$$r_p = \frac{1}{6\pi} \left( \frac{K^2 I_c}{\sigma^2} \right)$$

Using experimentally determined values for the yield stress and critical stress intensity, this is calculated at 56 micrometers.

The shape of the contour plots of von Mises' stress for the coupled and uncoupled models are seen to be roughly the same (Figures 9 and 10). A lower stress in the near crack tip region, as well as a lower maximum stress, can be seen in the coupled model. This is a result of not only the thermal softening, which lowers the stress bearing capacity of the element, but also of the thermal expansion. In the elements under positive stress, the thermal expansion caused by the increased elemental temperature acts to reduce the stress by providing additional compliance to the imposed forces at the nodes.

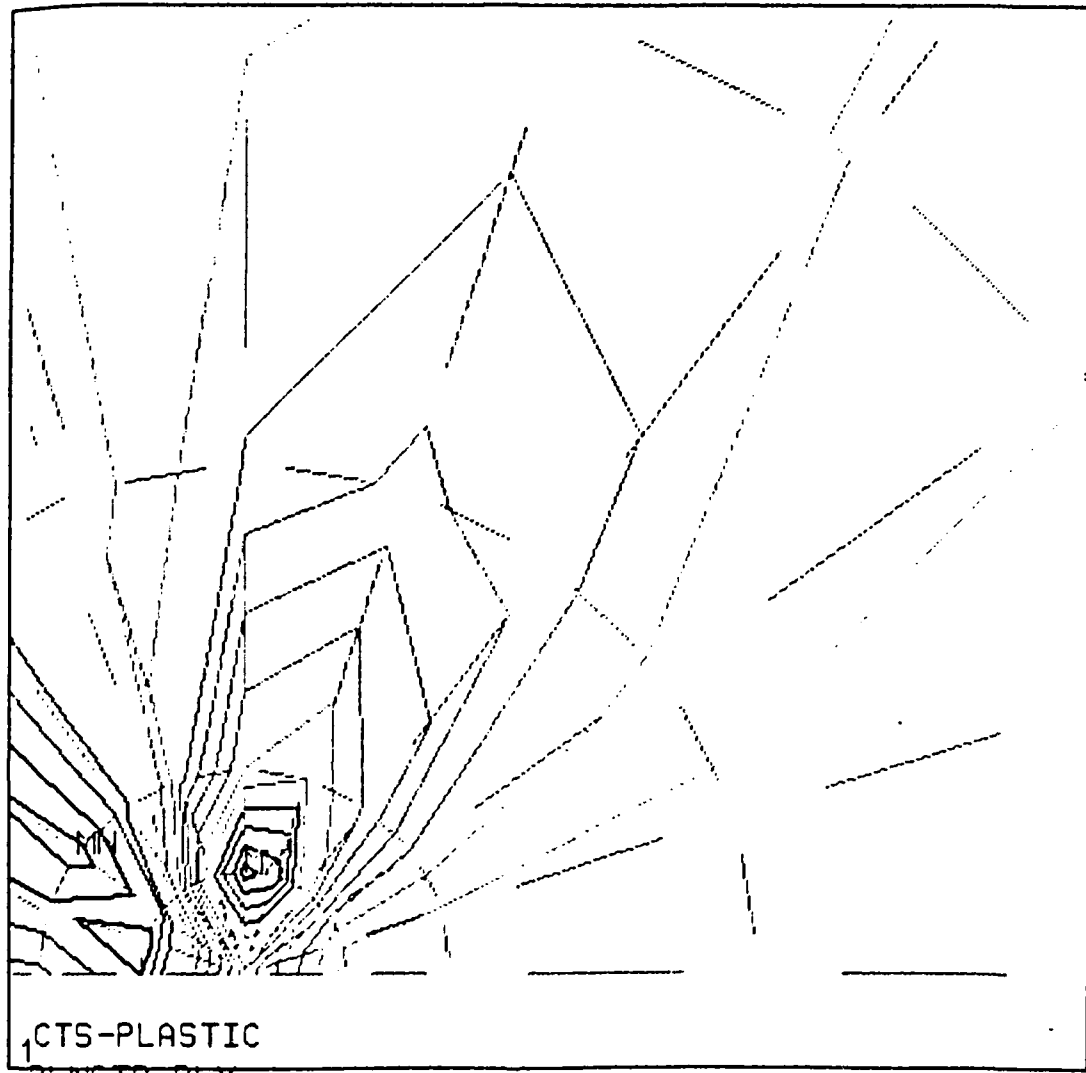


Figure 7.

The contour plot showing the plastic strain in the Y, or vertical, direction for the uncoupled model. The data column on the right lists the maximum strain (MX), the minimum strain (MN), the number of contours (NCON) and the strain increment between contours (VINC).

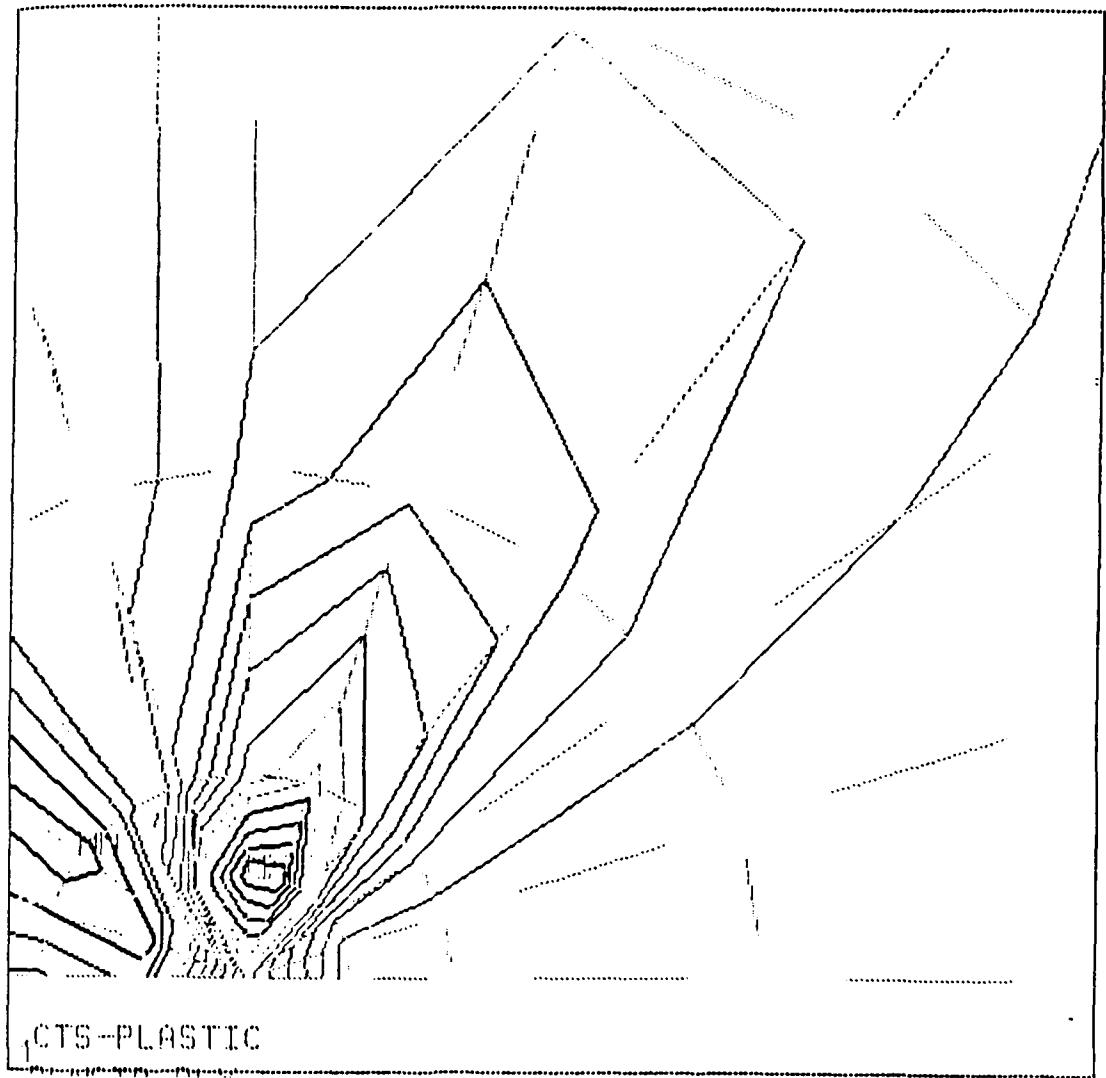


Figure 8. The contour plot showing the plastic strain in the Y, or vertical, direction for the thermal-mechanically coupled model.

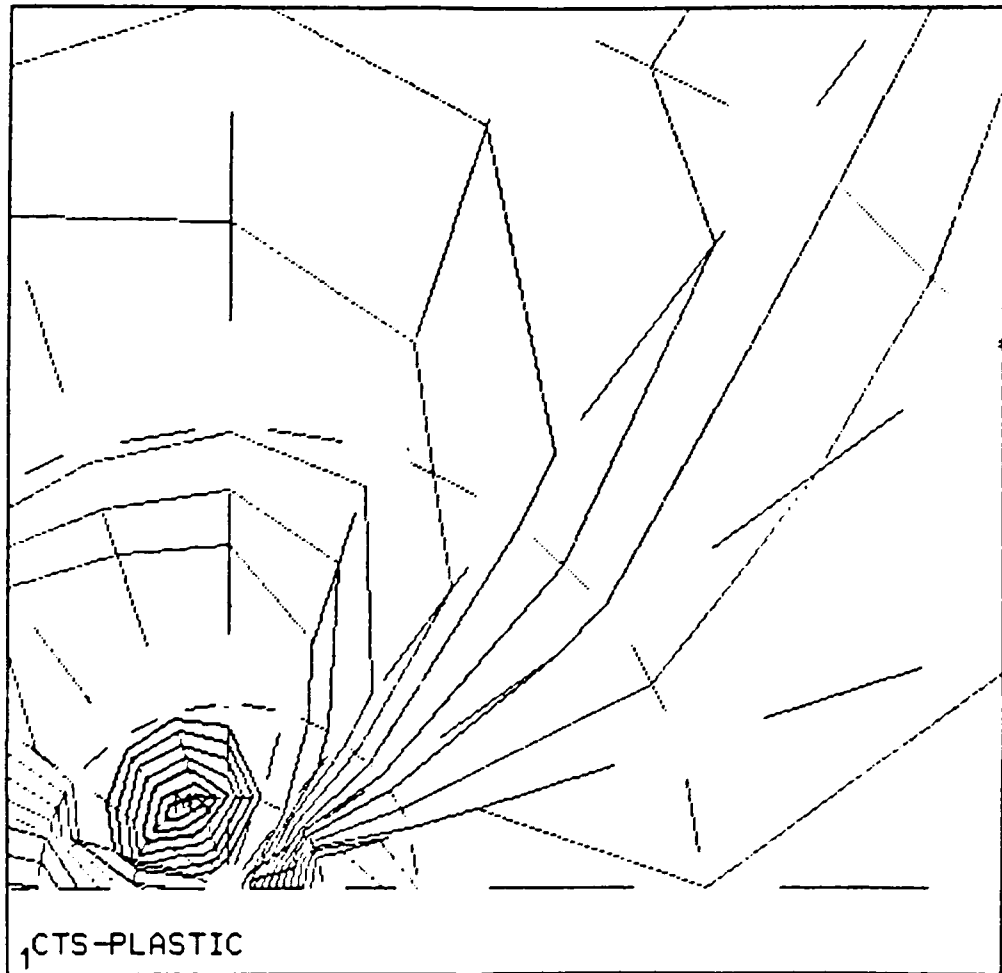


Figure 9. The contour plot of the van Mises stress near the crack tip for the uncoupled FEM model.

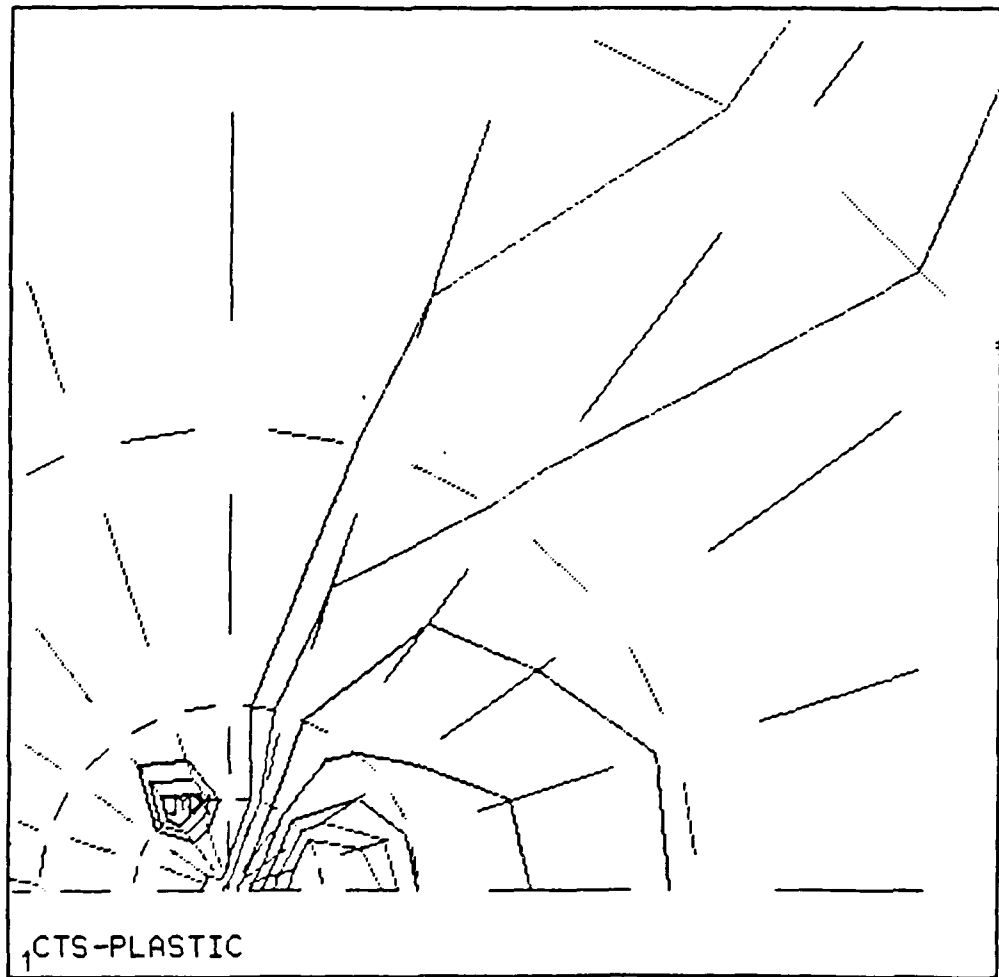


Figure 10. The contour plot of the von Mises stress near the crack tip for the thermal-mechanically coupled FEM model.

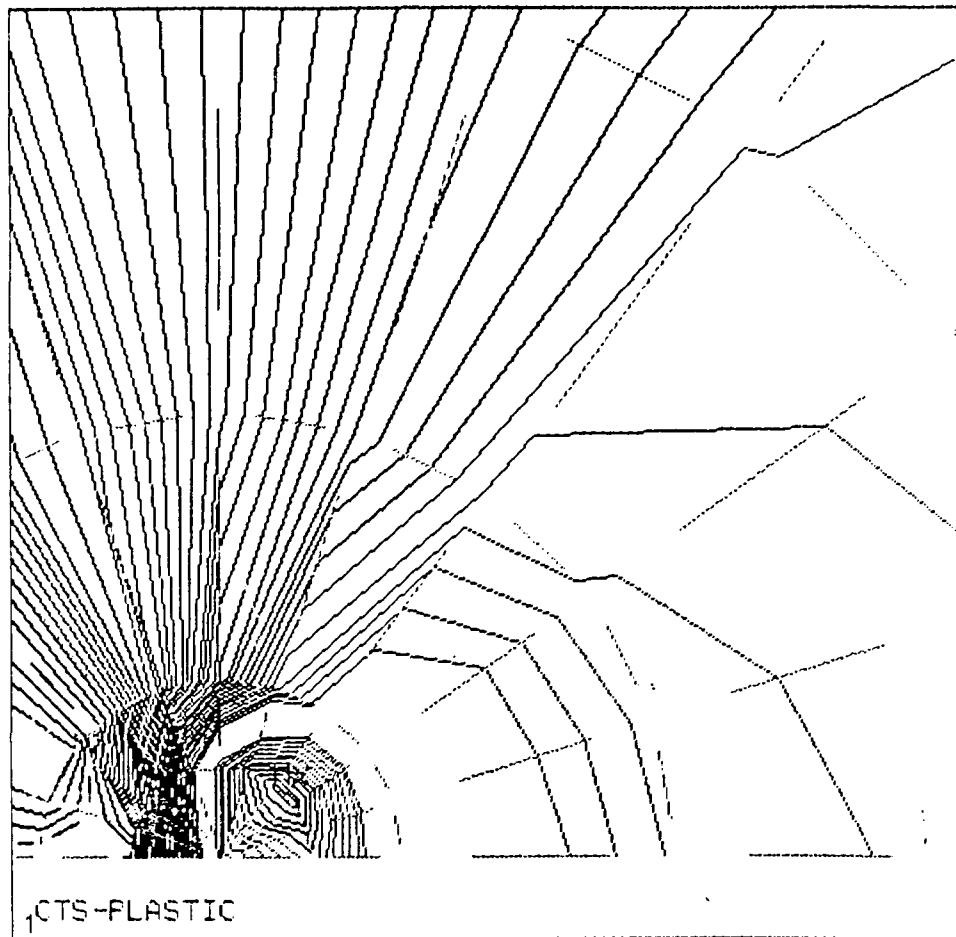


Figure 11. The Mode I, or vertical stress field is described in this diagram for the uncoupled FEM model. Important points to note are the shape of the stress contours ahead of the crack tip, and the maximum predicted stress in the Y direction of  $553 \text{ Kgf-mm}^{-2}$ .

The most interesting result of the analysis can be seen in the stress fields in the Y, or vertical direction, as it most clearly depicts effects of Mode I type loading. In Figure 11, the stress field for the uncoupled model is shown. This can be compared to the stress field for the thermal-mechanically coupled model in Figure 12, and several important differences can be noted. The intensity of the gradient in the stress directly ahead of the crack tip is greatly reduced in the model which incorporates thermal softening. The maximum value of stress in the Y direction (in the units used in the model of Kgf/mm) in the uncoupled model is seen to be 553 kgf/mm, while in the coupled model the maximum stress is reduced 35 percent to a value of 360 kfg/mm.

(ii) Transient Thermal Analysis

Using the thermal-mechanically coupled finite element analysis done for a compact tension specimen, the temperature fields generated through deformational heating can now be subjected to an analysis of the thermal flow as a function of position and time. The model described in the previous section is specifically for the case of a rapidly loaded compact tension specimen where the heat of plastic flow is allowed to perturb the material properties in that element alone. No attempt has been made to consider nonadiabatic conditions; the heat generated in elements undergoing plastic deformation was not allowed to dissipate to the neighboring elements. This was an unavoidable consequence of the modeling method used. Rather than running a thermal finite element analysis using simply the temperature field predictions from the final iteration, a one dimensional thermal analysis was performed based upon heat generation rate. It is the author's belief that this method more clearly elucidates the role of heat conduction in the near crack tip region.

(iii) Predicted Temperature Field

The temperature field predicted through the thermal-mechanically coupled stress model is shown in Figure 13. In the right hand column next to the diagram is the information required to interpret the diagram. The colored contours are at levels of 95°K, and the ambient temperature of the specimen was defined at 300°K (this is of

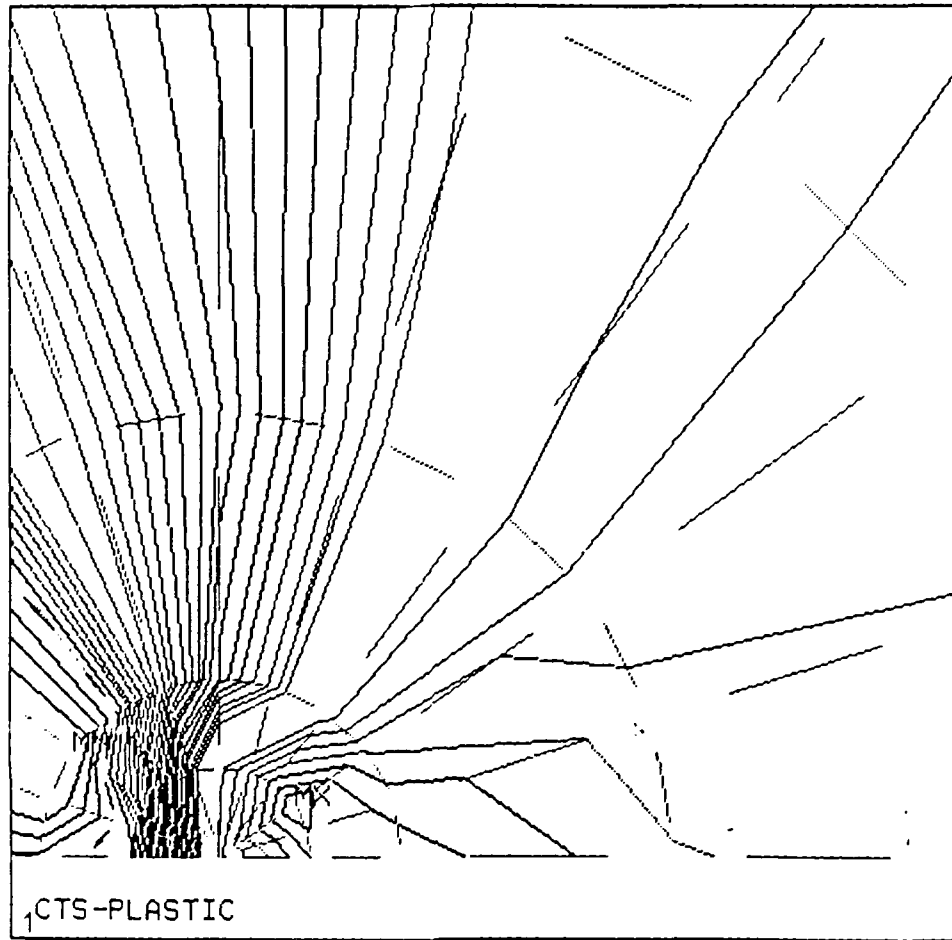


Figure 12. The Mode I type stress plotted for the uncoupled model in Figure 11 can be compared with the equivalent plot for the thermal-mechanically coupled FEM model. Important points to note are the shape of the stress contours, and the maximum stress near the crack tip, which has been reduced to  $360 \text{ Kgf-mm}^{-2}$  on account of the thermal softening and thermal expansion due to deformation induced heating.

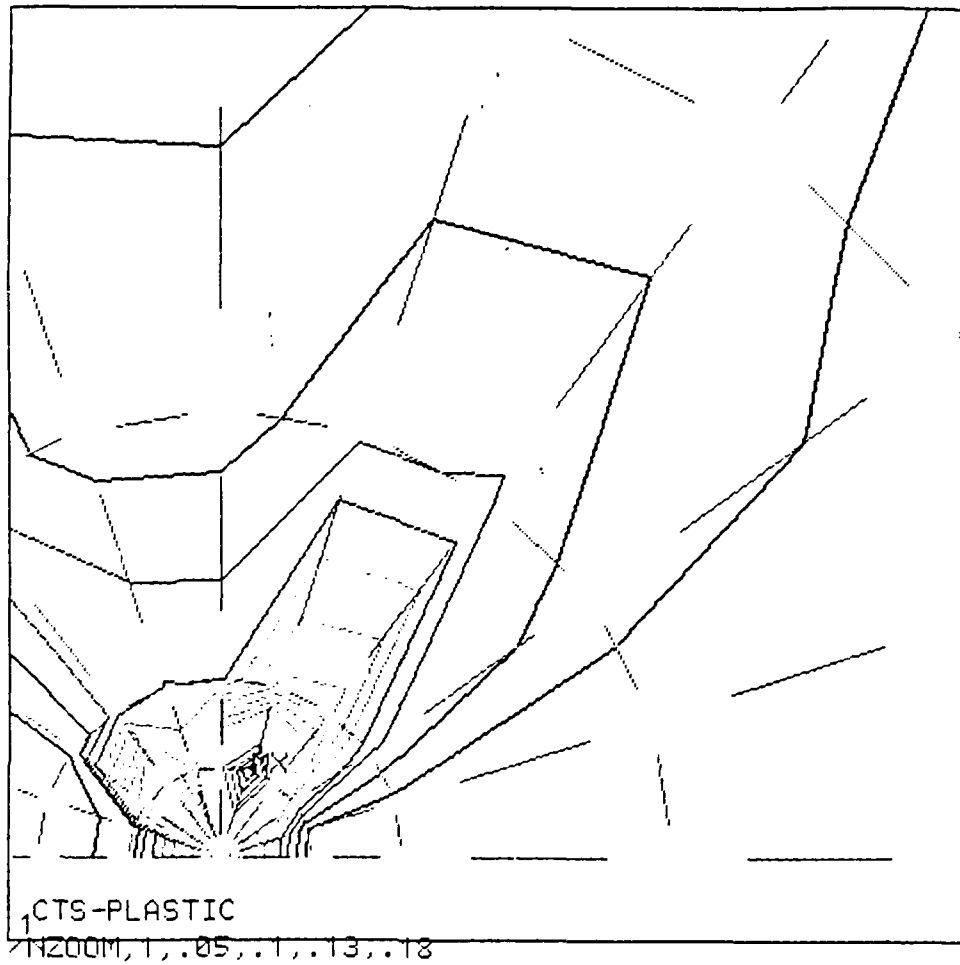


Figure 13. The temperature field predicted in the thermal-mechanically coupled finite element model. Temperature values are in degrees Kelvin, with a maximum predicted temperature increase of 852°C.

course the minimum temperature value, as shown in the right hand data column). The maximum temperature of 879°C (1152°K) occurs near the boundary between the first and second regime of semicircular element arrays; this places the position of maximum temperature rise at a position approximately 1.5 microns from the crack tip. The split in the shape of the temperature field, which can be seen near the vertical position, is a consequence of the shape of the field describing the plastic shear strain near the crack tip. The plastic shear strain changes sign near this region. This results in a smaller heating contribution due to plastic flow under this component of stress.

It should be noted that this model does not incorporate the very large strains present in an actual crack tip within the process zone. The process zone, which may have a radius of less than a micrometer, has been described as a region within the plastic zone characterized by very large strains, which may be more than 500 percent. The finite element analysis here was restricted to plastic strains of less than 35 percent. It is logical, therefore, that the analysis of the heating effects within the process zone developed in a previous work are applicable to this case and may be superimposed upon those predicted by the FEM.

#### (iv) One-Dimensional Transient Thermal Analysis

The temperature field predicted by the thermal-mechanically coupled stress analysis provides the spatial distribution of temperature on which the thermal analysis may be performed. The experimentally determined loading history and critical time (the time from initial loading to initial crack growth) gives the times over which the thermal model will be applied. The analysis done here is based on a treatment originally proposed by Carslaw and Jaeger.

Heat generation near the crack tip can best be modeled in one dimension as a semi-infinite plate. The near crack tip region in which heat is being generated is modeled as a band, of width  $L$ , located at the left hand edge of the plate, extending from  $X=0$  to  $X=L$ . The heat generation rate per unit area, defined as  $A$  is set to the average heat generation rate within the elasto-plastic boundary. This can be determined from the finite element results by averaging the heating contributions (on a per unit area basis) for those elements undergoing

plastic strain. The equation describing the temperature field as a function of time and position for any point X within the heat generating zone is given:

$$\Delta T = \frac{\kappa A_0 t}{K} \left[ 1 - 2i^2 \operatorname{erfc} \left( \frac{L-X}{2\sqrt{\kappa t}} \right) - 2i^2 \operatorname{erfc} \left( \frac{L+X}{2\sqrt{\kappa t}} \right) \right] \quad 0 < x < L$$

where  $A_0$  defines a constant heat generation rate,  $K$  the coefficient of thermal conduction, and  $k$  the thermal diffusivity. For any point X outside of the heat generating zone, the temperature is described by:

$$\Delta T = \frac{2\kappa A t}{K} \left[ i^2 \operatorname{erfc} \left( \frac{X-L}{2\sqrt{\kappa t}} \right) - i^2 \operatorname{erfc} \left( \frac{X+L}{2\sqrt{\kappa t}} \right) \right] \quad X > L$$

Obviously, the condition of uniform heat generation rate is approximate, and only valid for the case of a stationary crack tip at times less than  $t_c$ . At times greater than  $t_c$ , the crack has propagated away from this region and those heat generation sites active during loading are now quiescent. If the value of  $L$ , the width of the heat generating zone, is estimated from Figure 13, the equations can be applied to the case of the stationary crack tip undergoing rapid loading. Using the physical properties of Ti-10-2-3 and the relation of the thermal diffusivity to the other parameters given by:

$$\kappa = \frac{K}{\rho c_p}$$

the first equation may be rewritten in the form:

$$\Delta T = \frac{1}{\rho c_p} \left[ 1 - 2i^2 \operatorname{erfc} \left( \frac{L-X}{2\sqrt{\kappa t}} \right) - 2i^2 \operatorname{erfc} \left( \frac{L+X}{2\sqrt{\kappa t}} \right) \right]$$

The temperatures predicted under adiabatic restrictions are simply the values defined by the first coefficient of the equation. Expressed as a ratio:

$$\frac{\Delta T}{\Delta T_{Ad}} = 1 - 2i^2 \operatorname{erfc} \left( \frac{L-X}{2\sqrt{\kappa t}} \right) - 2i^2 \operatorname{erfc} \left( \frac{L+X}{2\sqrt{\kappa t}} \right)$$

Plot of  $T/T_{Ad}$  vs Time

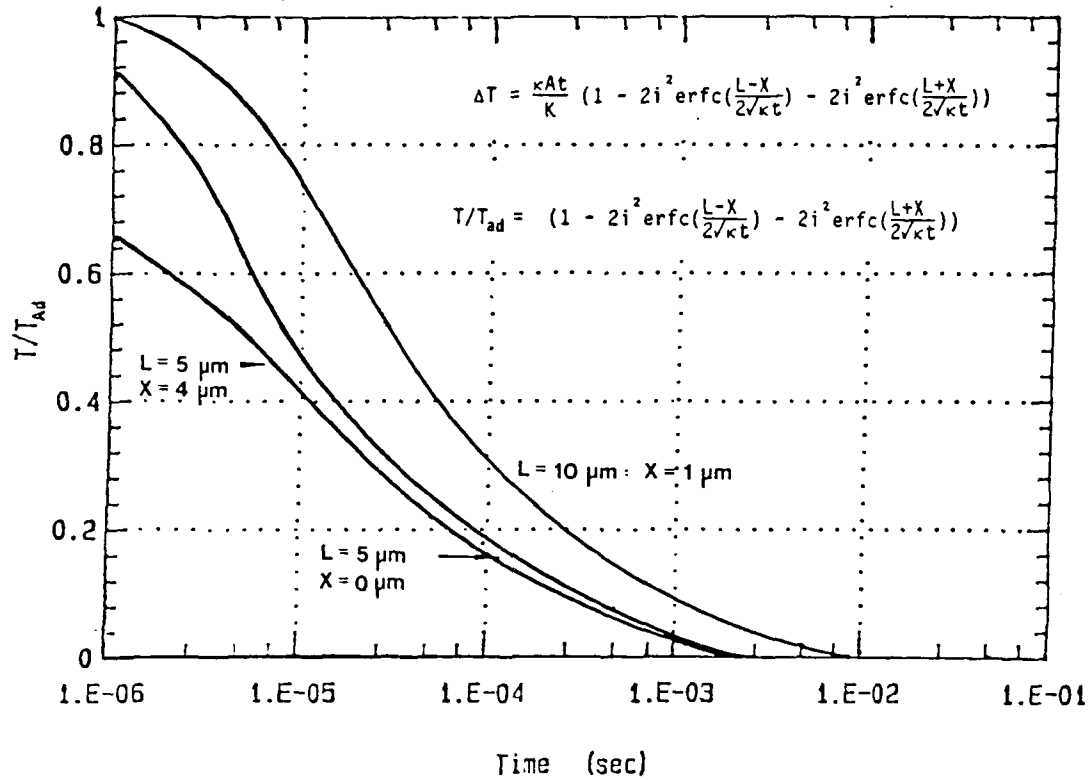


Figure 14. The effect of thermal conduction on the temperature field predicted by the finite element analysis for Ti-10V-2Fe-3Al can be judged using the curves shown above. The ratio of the actual temperature to the adiabatic prediction is read off of the ordinate. The effective loading time is read off of the abscissa.  $L$ , the width of the heat generating zone, was taken at values of 5 and 10 micrometers, from Figure 13.

The impact of thermal conduction away from the heat generating region is controlled by the arguments of  $i^2 \text{erfc}$  functions. As the right hand side of the equation approaches unity (the second and third terms on the RHS approach zero), the temperature field approaches the adiabatic case predicted by the finite element model. In Figure 14, this function is plotted for several values of  $L$  and  $X$  estimated from the spatial distributions in Figure 13.

Several conclusions can be made about the shape of these curves. First, at very short times, on the order of 1 to 10 microseconds, there is very little effect of thermal diffusion in the near crack tip region. At larger times, the effect of thermal conduction becomes great, lowering the temperature to nearly the ambient level in a time of a millisecond. This is a consequence of the very narrow width of the heat generating region.

When the critical times taken from the test results using compact tension specimens are applied to the equation above, it is apparent that thermal conduction plays a heavy role in the determination of the temperatures reached near the crack tip. The smallest experimentally determined critical time  $t_c$  of 2.2 milliseconds places the temperature within the heat generating zone at a value much closer to the ambient temperature than that predicted by the adiabatic model. The thermal transfer model, together with the experimental data, leads one to conclude that the effect of deformational heating on a rapidly loaded stationary crack tip is slight.

This result is not surprising considering the relatively large amount of time required to load a specimen to critical stress intensity for crack growth. If the model, though constructed for the case of a stationary crack, is applied to the case of a propagating crack, quite a different conclusion is reached. If one may safely ignore the effects of inertia, as a recent finite element work has shown, the finite element model developed here may be applied to the case of a moving crack tip. The parameter describing the time scale of loading may now be deduced from the experimentally measured crack propagation speeds and the stress calculations discussed in the previous section.

From Figure 11, the Mode I type stress drops off from its peak

value near the crack tip, to a value roughly half of this at a distance 20 micrometers ahead of the crack tip. For a point ahead of the propagating crack, the increasing stress at that point as the crack advances closer is equivalent to a loading rate directly proportional to the speed of the advancing crack. Using the distance over which the imposed stress drops to half of its peak value and the measured crack velocity, one calculates equivalent loading times for points ahead of a propagating crack. For a crack speed of  $10 \text{ ms}^{-1}$ , the argument within square brackets in equation 6 takes a value of .95, or 95 percent of the temperature rise value predicted by the adiabatic model.

#### 4. CONCLUSIONS

A finite element model has been developed and used to quantify the dynamic interaction between the stress, strain and temperature fields near a rapidly loaded crack tip undergoing deformational heating. The model has predicted the following:

1. The action of deformation heating acts to increase the maximum plastic strain within the plastic zone by 36 percent.
2. The von Mises and Mode I type stress are diminished between 30 and 35 percent in the thermal-mechanically coupled model. The lowered load bearing capacity caused by thermal softening is assisted by thermal expansion in the near crack tip elements.
3. The temperature field produced through deformational heating has been determined for the adiabatic case. Temperature increases of up to  $830^{\circ}\text{C}$  are predicted for some regions within the plastic zone (excluding the process zone).
4. The effect of non-adiabatic conditions has been gaged using the temperature field calculated from the FEM and the equations for heat transfer. It has been determined that only under exceedingly high loading rates ( $10^5 \text{ MPa}\sqrt{\text{m}}/\text{s}$ ) will adiabatic type heating play a predominant role on the stress and strain fields of a stationary crack.
5. In the case of the propagating crack, it was found that the effective loading rate at which adiabatic heating effects become significant occurs when crack propagation speeds reach the realm of 10 m/s and over.

#### REFERENCES

1. S. Kuriyama and M. A. Meyers, *Met. Trans.* 17A (1986) 443.
2. R. Hoff, C. A. Rubin and G. T. Hahn, *STP 868* (1983), 409, ASTM, Philadelphia, PA.
3. ANSYS, The Swanson Corporation, Pennsylvania; Version 42.
4. H. C. Carslaw and R. Jaeger, Conduction of Heat in Solids, Oxford Univ. Press (1984), 224.

SECTION IV  
A GEOMETRICAL MODEL OF THE STRAIN RATE  
DEPENDENT FRACTURE OF Ti-8Mn

Based on a Ph.D. Thesis (Materials Science) by David D. Makel, UVA, 1987

ABSTRACT

During the examination of the fracture surfaces of primarily plane stress Ti8Mn tensile samples, regions were found which have a finely roughened texture and are covered with small spheroidized volumes of material. The high strength and low thermal conductivity of this titanium alloy suggest that these unusual features may result from adiabatic type heating effects during the final separation.

To investigate the possibility of high temperatures being generated during straining to fracture, tensile samples were tested over a range of strain rates and the resulting fracture surfaces were thoroughly characterized with stereo pairs of scanning electron micrographs. After characterization, the surfaces were nickel plated, imbedded in resin and sectioned to reveal the microstructures underlying the various surface structures. These sections reveal highly localized zones of shear directly below the unusual surface features.

Localized shear and high temperatures are two of the basic components needed for adiabatic shear, a deformation mechanism generally associated with considerable compressive stresses and, therefore, not usually considered as playing a role in tensile testing. To determine whether or not the unusual surface features are caused by local melting due to adiabatic shear, the effects of high surface temperatures were investigated, as well as the possible role of oxidation. A geometrical model of adiabatic shear is presented in this report.

Analyses of the heating effects which occur during straining and separation indicate that temperatures as high as the melting temperature are reached at separation, and that elevated temperatures play an important role in the material instability and strain localization which lead to fracture.



TABLE OF CONTENTS

	<u>Page</u>
1. INTRODUCTION .....	71
2. INITIAL TESTING AND OBSERVATIONS .....	71
(i) Tensile Testing .....	71
(ii) Microscopic Examinations .....	79
3. VERIFICATION OF ADIABATIC SHEAR .....	85
4. APPLICATION OF ADIABATIC SHEAR TO THE FRACTURE SEQUENCE .....	91
5. ADIABATIC SHEAR AND THE SEQUENCE OF TENSILE SEPARATION .....	93
6. CONCLUSIONS .....	96
7. REFERENCES .....	98



A GEOMETRICAL MODEL OF THE STRAIN RATE  
DEPENDENT FRACTURE OF Ti-8Mn

1. INTRODUCTION

The primary thrust of this study has focused on the effects of strain rate on the strength, toughness and fracture mode of high strength, low heat conductivity materials, in this case, titanium 8 w% manganese. A synopsis of the results of this research can be broken down into three major categories:

- (1) Observation of apparent high temperature fracture surface features;
- (2) Identification and verification of adiabatic shear as the primary mechanism responsible for the temperature rise; and
- (3) The application of the concept of adiabatic shear to the overall fracture sequence.

A brief description of the experimental methods used in our studies will be given followed by the significant results and a discussion of the implications and conclusions which can be drawn.

2. INITIAL TESTING AND OBSERVATIONS

(i) Tensile Testing

The primary alloy used in this research, titanium 8 w% manganese, was chosen because it is easily heat treated to a condition of high strength and moderate toughness, it has a very low thermal conductivity thereby enhancing any adiabatic-type effects, and it is a binary alloy with a well-defined phase diagram and thoroughly investigated microstructures. The use of a standard commercial alloy eliminated the necessity of exhaustive microstructural classifications prior to the mechanical testing and post-fracture examinations.

A single rolled sheet of Ti 8 w% Mn was used for all of the samples so that the results of different samples could be confidently compared without worrying about variations in chemistry and initial microstructure. Sheet samples were used to emphasize the shear nature of the fracture since shear separation is dominant in plane stress. The sample configuration used is shown in Figure 1. The surfaces of the

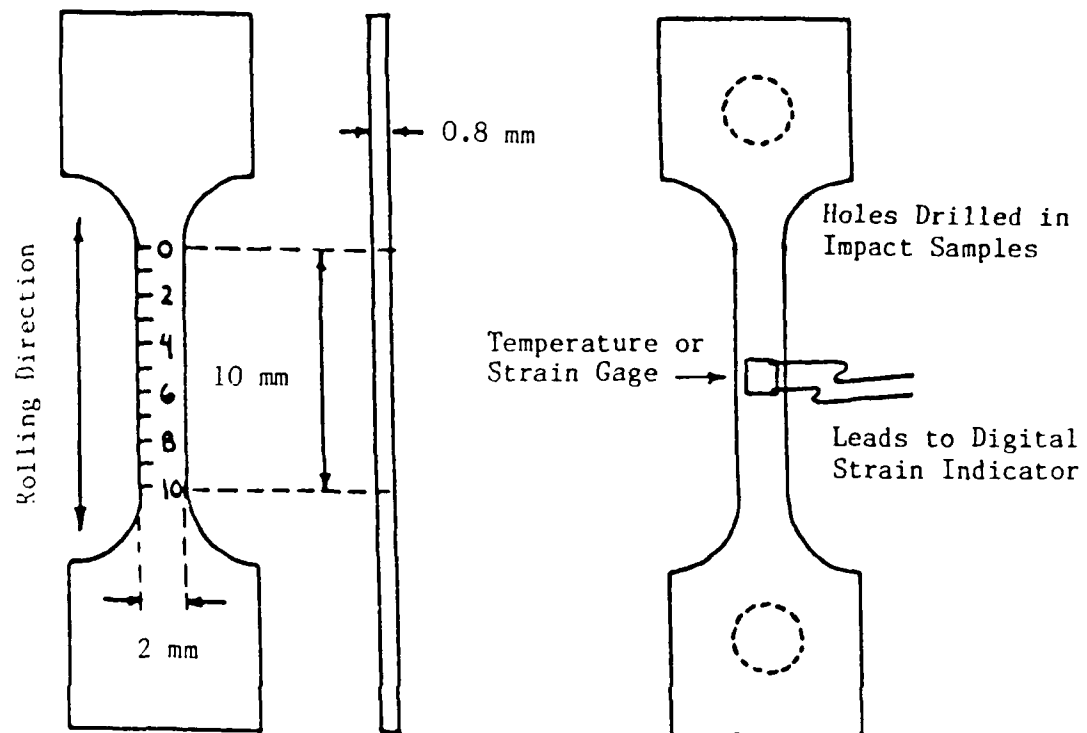


Figure 1. Tensile sample configuration.

samples were wet ground down to grit size 600 to reduce the stress concentration caused by surface scratches.

Two heat treatments were used for the samples; solutionizing for one hour at 800°C, water quench, three day aging at 600°C, air cool (wq-a), and solutionizing one hour at 800°C, 20 minute furnace cool to 600°C, three day aging at 600°C, air cool (fc-a). Both of the heat treatments result in acicular + grain boundary  $\alpha$  in a  $\beta$  matrix, but the furnace cooled samples have considerably larger  $\alpha$  platelets, as shown in Figures 2 and 3. Although the strength and elongation is comparable for both treatments, the furnace cooled samples were used for the low-to-moderate strain rate tests because the coarser platelets facilitate the determination of local strain values, as will be seen later on.

Tensile tests were performed on two different machines, low rate ( $8.75 \times 10^{-4} \text{s}^{-1}$ ) tests on an Instron twin screw frame and the low-to-medium rate ( $6.26 \times 10^{-3} \text{s}^{-1}$  to  $8.54 \times 10^{-2} \text{s}^{-1}$ ) tests on an MTS servo-hydraulic system in stroke control. Even at the moderate rates used in these tests, data acquisition was a considerable problem due to the slow chart pen response. To record the load-elongation data, a personal computer with an a/d board with a data storage rate of 10,000 hz was used in conjunction with a storage oscilloscope with a writing speed of 10  $\mu\text{sec}$  per dot. The combination of the oscilloscope traces and the digital data files proved an effective means of recording the tests, the results of which are summarized in Figure 4.

Figure 4 shows the slightly positive strain rate dependence of the material. This rate dependence is understandably small, since the dramatic increases in strength demonstrated at high rates generally do not appear until strain rates above approximately  $5 \times 10^3 \text{s}^{-1}$ .

The load-elongation curves recorded in the low-to-medium strain rate tests showed a marked decrease in the strain hardening rate with increasing strain rate. At the highest rates tested the true stress/true strain curves actually had a negative hardening slope indicating that work softening occurs. This result suggested that (1) the mechanisms which caused hardening at lower rates are not as effective in decreasing the effective dislocation link length, and

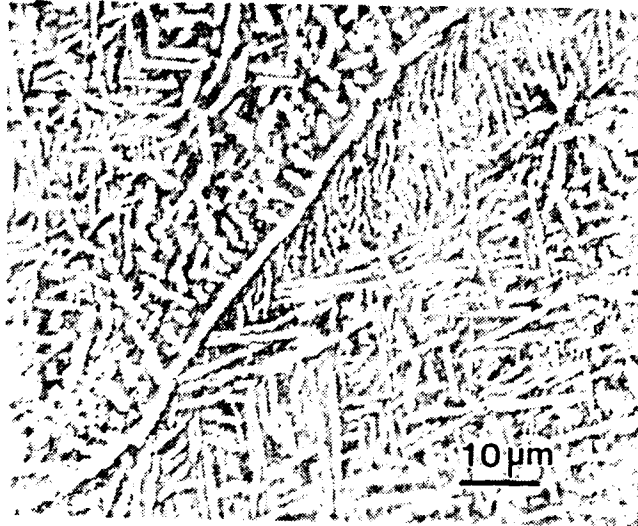


Figure 2. Typical microstructure of water quenched and aged (wq-a) Ti 8w% Mn samples.

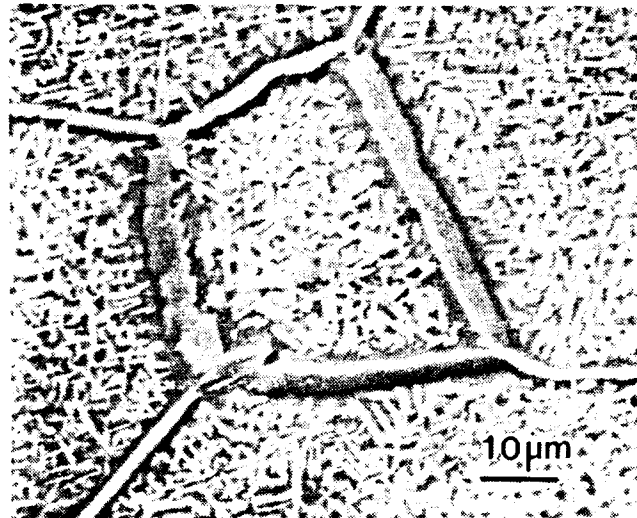


Figure 3. Typical microstructure of furnace cooled and aged(fc-a) Ti-5wt% Mn samples.

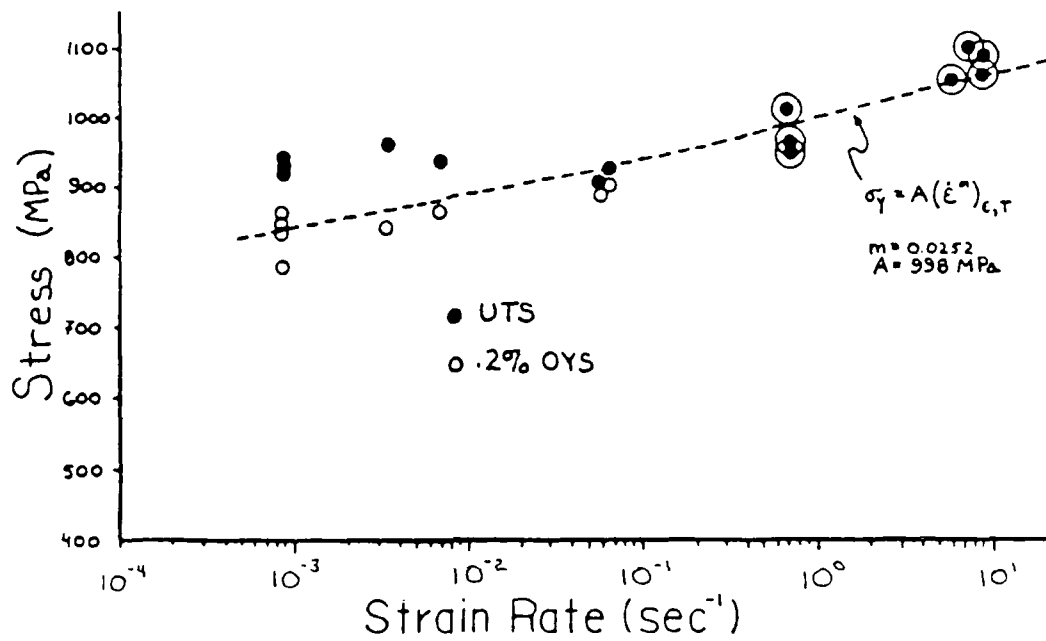


Figure 4. Variations of UTS and 0.2% OYS with strain rate for furnace cooled and aged (fc-a) samples.

therefore the instantaneous yield strength of the material and (2) thermal softening of the whole gage length might play a significant role in lowering the yield strength at increasing rates. Dislocation drag mechanisms were not considered because these effects are generally not detected at rates below approximately  $1 \times 10^3 \text{ s}^{-1}$ .

Temperature measurements of the gage length were desirable to test the second of the these possibilities. Thin film resistance-type surface temperature gages were applied to a selected group of samples which were strained to fracture at  $5.7 \times 10^5 \text{ s}^{-1}$ . A typical temperature vs. time curve is shown in Figure 5 showing a maximum surface temperature rise of about  $38^\circ\text{C}$ . Considering that the test took only 38 msec to fracture, it is clear that there is considerable thermal lag in the measuring system. This test does, however, confirm the adiabatic nature of the overall temperature rise in the gage, in complete agreement with the strain rate window for "quasistatic adiabaticity," as determined by Olsen et al. [1] and Culver [2].

Since the calculations and experimental results indicate that a fully adiabatic model can be effectively used to describe the temperature increase in the overall gage, previously measured yield strength vs. temperature information [3] was used to determine an approximate differential strain softening rate due to thermal softening. When the theoretical softening rate was compared with the measured softening rates at elevated strain rates it was found that thermal softening could only account for the decrease in work hardening rate up to strain rates of  $6 \times 10^7 \text{ s}^{-1}$ , above which other mechanisms must also contribute.

Stress-time traces of the tensile tests also show an interesting phenomenon, the decrease in strength with time after the critical instability. The dots are written at a rate of 1 dot per 10 msec and we can confidently say that the complete separation event occurs in approximately 10 msec or less. Even more interesting is the fact that three different samples at  $1.6 \times 10^7 \text{ s}^{-1}$ ,  $6.0 \times 10^7 \text{ s}^{-1}$  and  $6.0 \times 10^7 \text{ s}^{-1}$  all display identical load drops with time after the final instability. This is a clear indication that whatever stored energy must play a role in the final separation, since the applied strain rates are so high that the event has no appreciable effect over three orders of magnitude.

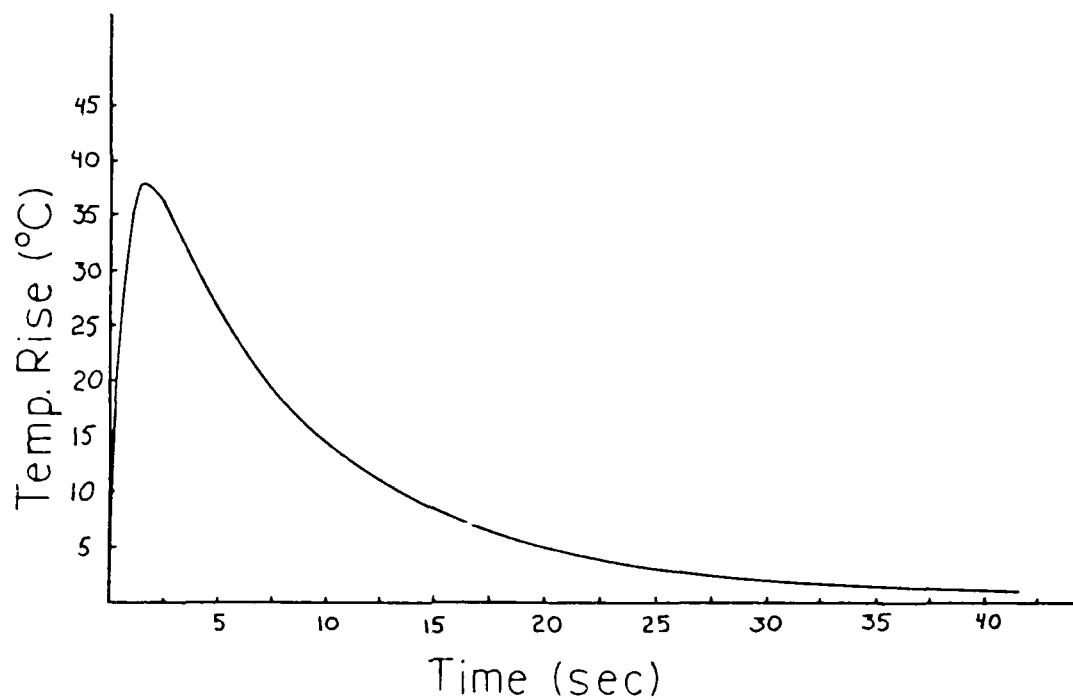


Figure 5. Plot of temperature versus time as measured with a resistance-type temperature gage. Recorded temperature is integrated over an area of approximately  $4\text{mm}^2$  on the surface of the tensile sample.

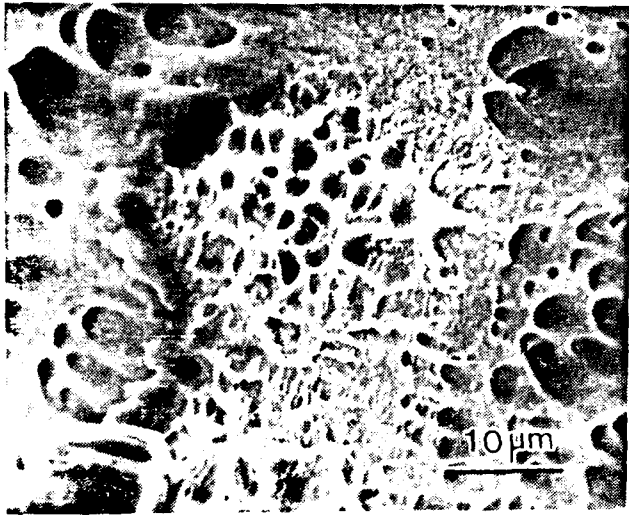
By reconstructing the samples after fracture and measuring them on a profile projector, total elongation measurements were made. These were complimented by pre- and post-fracture measurements of gage marks shown in Figure 1. By measuring the gage marks outside of the slightly necked regions of the gage lengths uniform elongation measurements were also taken. Elongation data demonstrate a decrease in elongation with increasing strain rate.

(ii) Microscopic Examinations

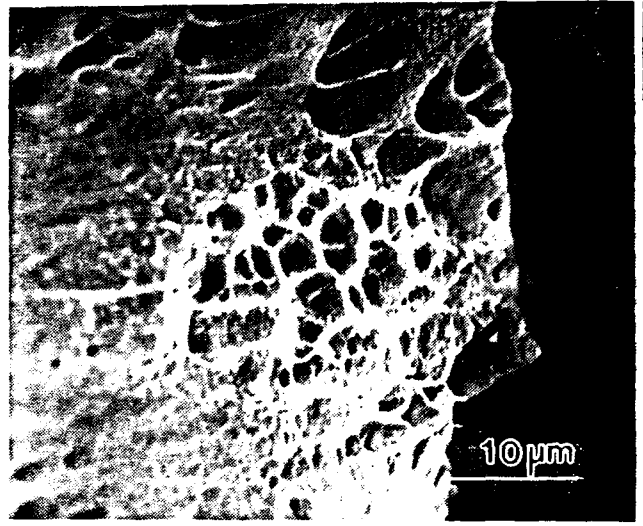
Analysis of the fracture surfaces in the scanning electron microscope consisted of two steps (1) complete characterization of the various features found on the surfaces using stereo microscopy techniques and (2) nickel plating of the surfaces followed by sectioning, grinding, polishing and etching to reveal the microstructures beneath the various surface features. The combination of surface and subsurface micrographs provides significant insight into the final fracture sequence.

A low magnification overview of the fracture surfaces shows the typical features one might expect; central crack areas covered with mode I and III ductile dimples and lamella resulting from separation along grain boundaries, and shear lip regions covered with regular mode I, II and III ductile dimples lying in directions of high shear relative to the tensile axis. Although the relative amounts of central and shear lip areas showed no dependence on strain rate, the water-quenched and aged samples display consistently more central crack area (on the order of 50%) as compared to the furnace cooled and aged (on the order of 10%).

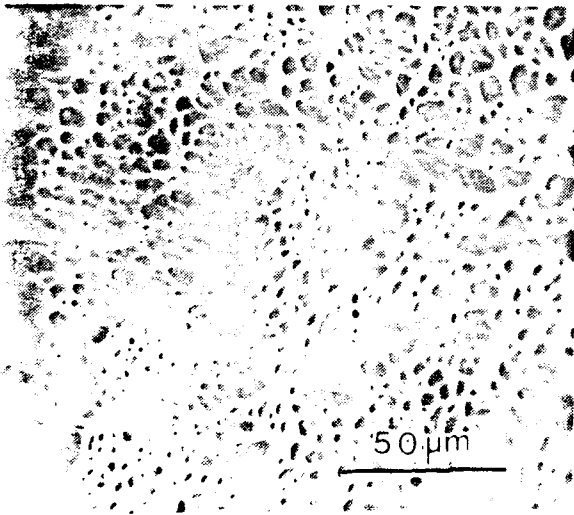
At higher magnifications other unusual and unexpected features become apparent. The most dramatic of these features are spheroidized surface debris, which are found primarily along the dimple walls at the borders of the shear lip areas. An example of this debris is displayed in Figure 6, which shows matching dimples from both of the fracture surfaces. As can be seen in Figures 6c and 6d, spheroidized debris is also found scattered across the neighboring surface.



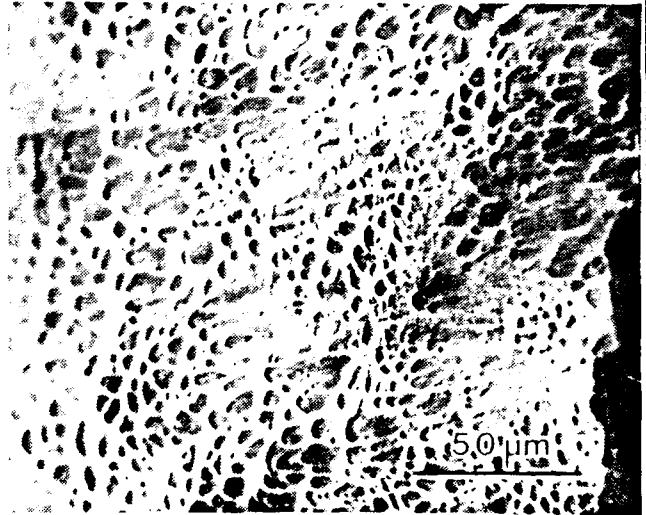
(a)



(b)



(c)



(d)

The surface areas where the spheroidized debris is found show another interesting feature at high magnifications, a fine roughening ("microroughening"). This "microroughening," shown in Figure 7, is always found in the areas containing the spheroidized debris. Because it has a grey tint in the SEM at low magnifications, "microroughening" facilitates the location of the regions containing the unusual features which, for reasons which will later become apparent, are called Inner Surface Shear Zones (ISSZs).

Dimple-free bands of material are found adjacent to some but not all of the ISSZs. These areas, an example of which is shown along the right side of Figure 8, are unusual not only because of their almost complete lack of dimples, but also because they contain striations which are oriented generally in the directions parallel to the shear directions, as indicated by the shear dimples around the spheroidized debris covered areas. When matching fracture surfaces are compared, the dimple-free bands, which will be called Open Surface Shear Zones (OSSZs), almost completely surround the shear lip areas, with approximately one half of the OSSZs on each of the matching fracture surfaces.

To get a better idea of the relative positions of the various features just described, overall maps of the surface structures were constructed, an example of which is given in Figure 9. This diagram also demonstrates that the matching surfaces of the samples can be divided into a small number of major areas, each of which display a predominant shear direction, as indicated by the arrows. The fact that these areas display common shear directions, as determined by the matching shear dimples and the striations on the OSSZs, is a clear indication that the final separation occurs as a small number of major shear events, three in the case of Figure 9. It should also be noted that the major shear directions displayed on the fracture surfaces are in every case compatible with the overall motion of the separating sample segments, i.e. adjacent major shear segments never display opposing shear directions. In Figure 9 this compatibility is maintained across the surface by the interior region of twist which requires different shear directions on either side.

The next step in the microscopic investigation was to coat the

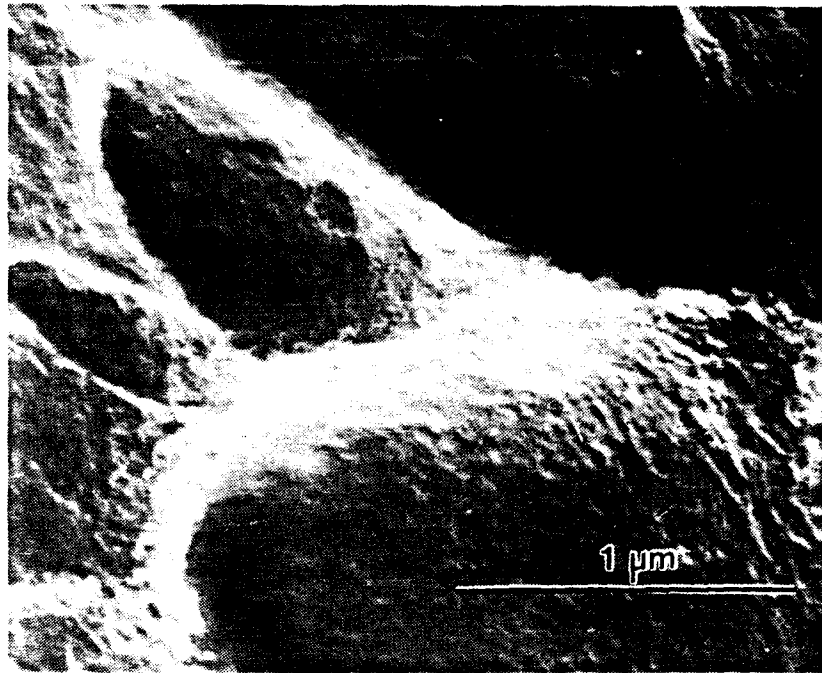


Figure 7. Micrograph showing "microroughening" of surfaces in the Inner Surface Shear Zones.

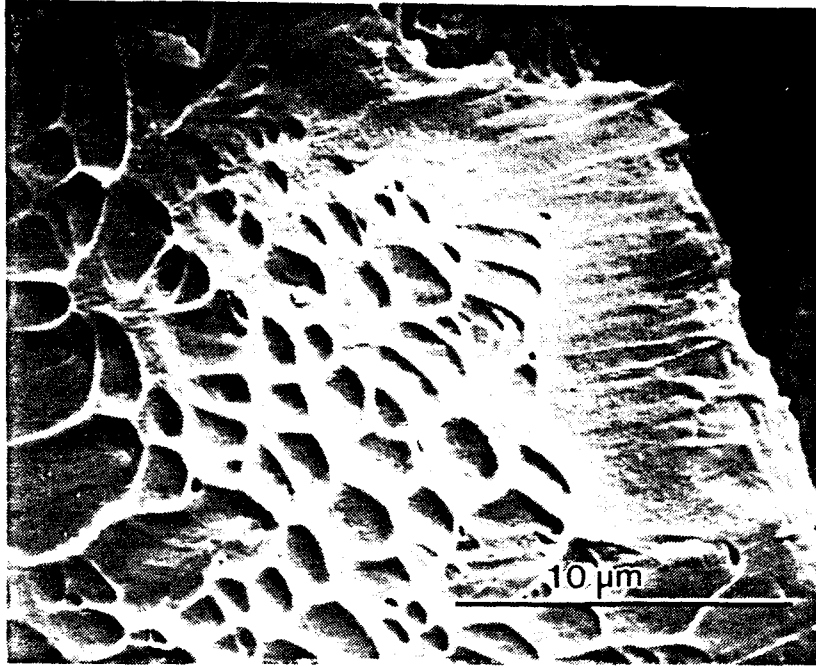
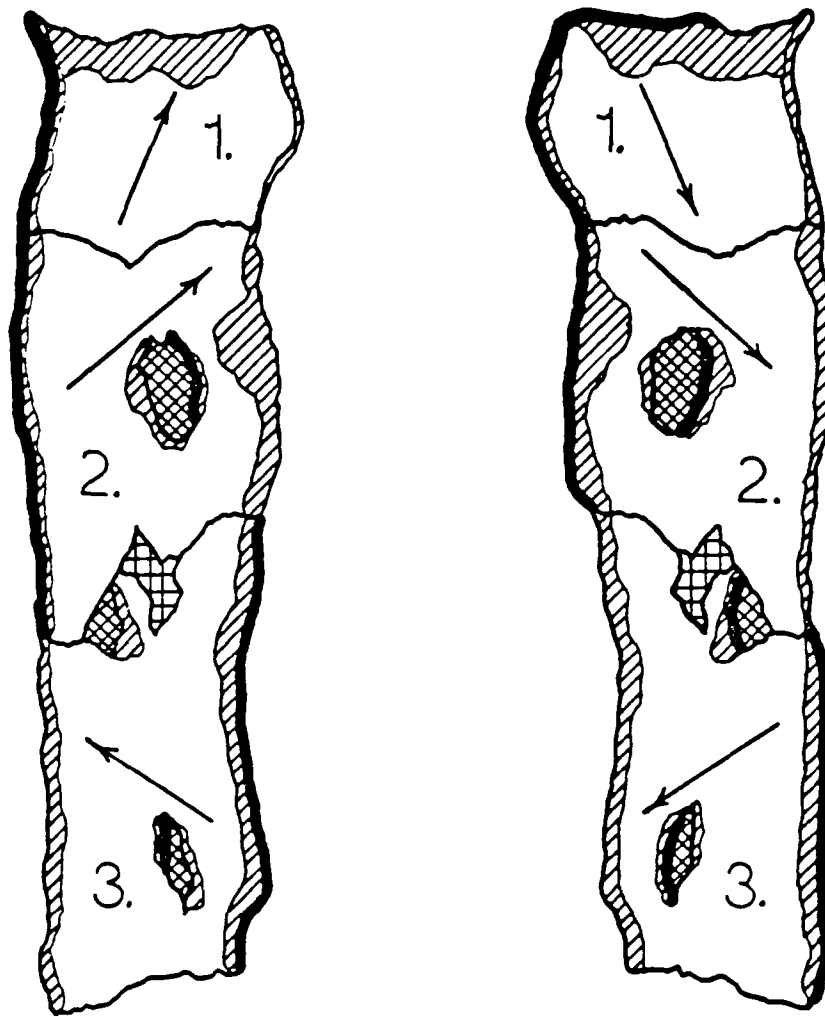


Figure 8. Micrograph showing an example of transition dimples and dimple-free area at right.



Inner Surface Shear Zone (ISSZ) locations



Outer Surface Shear Zone (OSSZ) locations



Mode I (tensile) separation regions



Mode III (twist) central crack region

Numbers indicate matching shear lip surface areas

Arrows show the overall shear directions on the major shear lip regions

Figure 9. Schematic diagram of matching fracture surfaces containing the major fracture surface types found in our samples.

characterized fracture surfaces with a heavy layer of nickel to preserve the fine surface structures and then section the samples parallel to the tensile axis. After grinding, polishing and etching, the subsurface microstructures were examined and compared with the corresponding stereo surface micrographs. In the case of the typical ductile dimples, the sections demonstrated that the crack path is influenced by the acicular  $\alpha$  precipitates and also by grain boundary  $\alpha$  with the  $\alpha$ - $\beta$  interfaces serving as preferred sites for separation, as demonstrated in Figure 10. This result is in agreement with earlier studies of Ti 8w% Mn and other  $\alpha$ - $\beta$  titanium alloys.

When the material under the unusual surface features (ISSZs and OSSZs) was investigated, an unexpected phenomenon was observed; the microstructures clearly showed extremely high shear strain localized into thin layers, as depicted in Figure 10a. These shear bands range in thickness from 1 to 3  $\mu$ m under the surface and are occasionally found to intersect each other under surface irregularities, as shown in Figure 10b, leaving regions of rotated material between the two bands. These bands of concentrated shear provide a critical clue to the explanation of the unusual features.

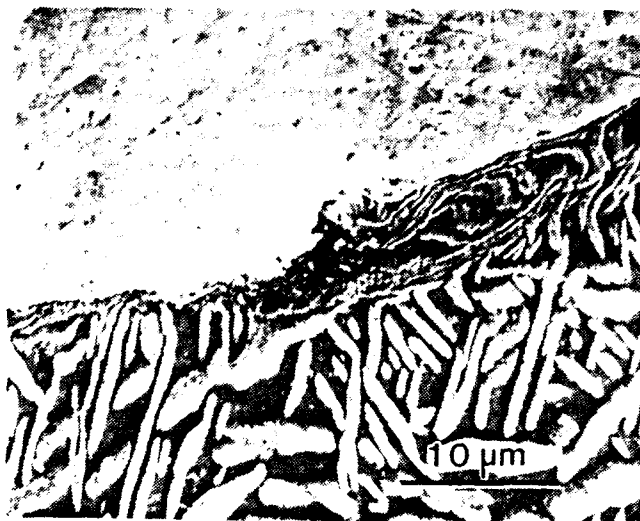
### 3. VERIFICATION OF ADIABATIC SHEAR

The presence of spheroidized surface debris posed an intriguing question as to the nature of its formation. Spheroidization due to the reduction of surface area of molten material and high temperature oxidation were selected as the two most probable causes of these unexpected surface features. In both cases, very high surface temperatures are required, but in the case of oxidation, the temperature rise is on the order of 600°C, as compared to approximately 1400°C for melting. For this reason it became important to determine whether or not the material had to reach the melting temperature to form the spheroidized surface structures.

To determine the role of oxidation, samples were strained to fracture in a chamber which was evacuated and backfilled with argon four times, effectively eliminating almost all of the available oxygen and nitrogen. In every case, the samples tested in this inert atmosphere display the same features as those fractured in air, clearly indicating



(a)



(b)

Figure 10. SEM micrographs of sections cut through unusual surface features. 10a shows a localized shear band typical of those found below the Inner Surface Shear Zones. 10b is an example of rotated volumes of material found at the intersections of different shear bands.

that oxidation does not play the primary role in spheroidization of the surface debris.

It was also important to determine if the "microroughening" found on all of the ISSZs could be considered a temperature effect. Unfortunately, the situation of a high temperature surface layer lying over a much lower temperature substrate is very difficult to reproduce under controlled conditions. As a rough approximation of this condition, areas of ductile dimples which did not display "microroughening" after fracture were characterized in the SEM, flash heated to a bright white color with a neutral hydrogen-oxygen flame, and cooled in flowing argon. With this technique it was possible to reproduce the fine surface roughening found in the ISSZs, as displayed in Figure 11. The success of the flash heating in causing "microroughening" strengthened the concept that the formation of the unusual features is closely related to very high local temperatures.

When the conditions of concentrated shear and high temperatures are present, adiabatic shear is a logical explanation. Although concentrated shear was clearly demonstrated in the subsurface sections, the presence of high temperatures had not been directly observed in any of the experiments, and this was a critical step to confirm the presence of adiabatic shear bands.

After ruling out oxidation, melting of the newly forming surface areas was the most likely cause of the observed spheroidization, and the local surface temperatures required for this to occur must reach at least 1400°C. Temperatures this high not only promote luminescence by chemical reactions at the fresh surface but also cause the emission of visible light by black body radiation. It was reasoned that if black body radiation does occur during final separation this radiation should be visible to the naked eye and also recordable by means of fast photographic film.

Direct observation of light emission during separation is complicated by two factors: (1) the flash is very short in duration and is, therefore, easily missed and (2) separation is generally accompanied by a sharp report which causes the eyes to naturally blink and miss the small, short flash. Even with these complicating factors, certain samples were seen to emit a clear light flash at separation when the

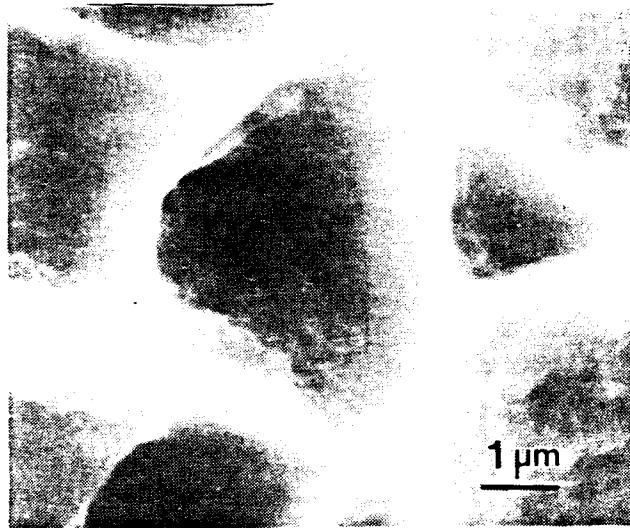


Figure 11. Fine surface roughening ("microroughening") produced by rapidly heating initially smooth dimples with a neutral propane-oxygen torch for approximately 1.5 seconds.

tests were conducted in a totally blacked out room.

To record the observed light flash, ASA 1000 film (Kodak Recording Film 2475) was used with a 35mm camera and a Vivatar macro lens. Prior to testing, all of the lights in the room, including the indicator lights on the tensile testing system and the CRT of the computer were blacked out or turned off to make the room as dark as possible. This made taking the photographs a simple matter of opening the shutter prior to the test and closing the shutter after separation. The initial images recorded by this method clearly show bright particles apparently ejected from a localized region in space. To more directly link these bright objects to the newly forming fracture surfaces, a variety of backlighting conditions were tested until one was found which gave the location of the light relative to the samples. Figure 12 is an example of the dim profile of the sample along with the bright particles ejected during separation.

In the case of the test shown in Figure 12, three bright areas could be seen at the newly formed surfaces, and when the surfaces were examined with the SEM it was found that these three regions contained the only areas of considerable spheroidization. This is a very important result, since it clearly links the formation of the unusual spheroidized dimple walls and surface debris with the emission of light. An extensive literature search into light emission of separating metals turned up a short report of this effect in the tensile fracture of another titanium alloy [4]. In this study it was found that light emission could be enhanced by enriching the oxygen content of the surrounding atmosphere but, more importantly, it also showed that the flash persisted under vacuum, in complete agreement with our inert atmosphere results.

The light emission results are confirmation of the tremendous local temperatures which are generated at separation, and, when combined with the observed localized subsurface shear, corroborate the concept of adiabatic shear bands playing a vital role in the formation of the unusual surface features. This constitutes the first experimental evidence of adiabatic shear in tensile tests and also discounts the concept that considerable compressive stresses are necessary for

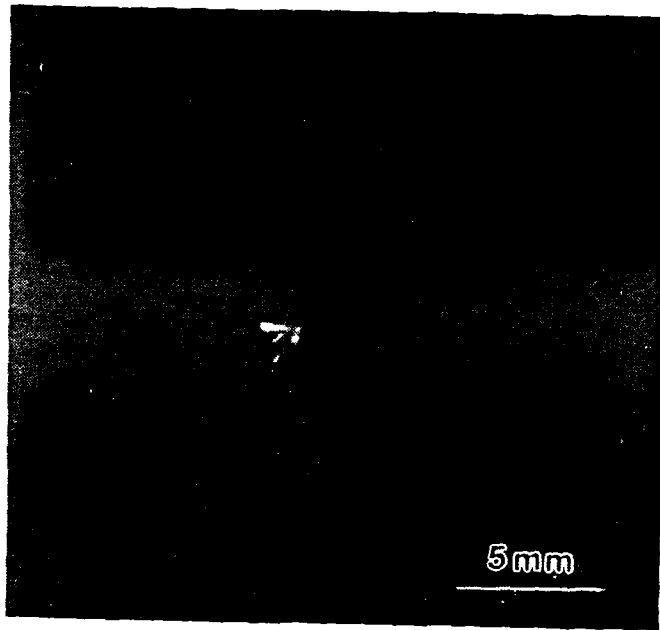


Figure 12. Image of light emission at separation in a tensile test including dimly backlit image of the sample.

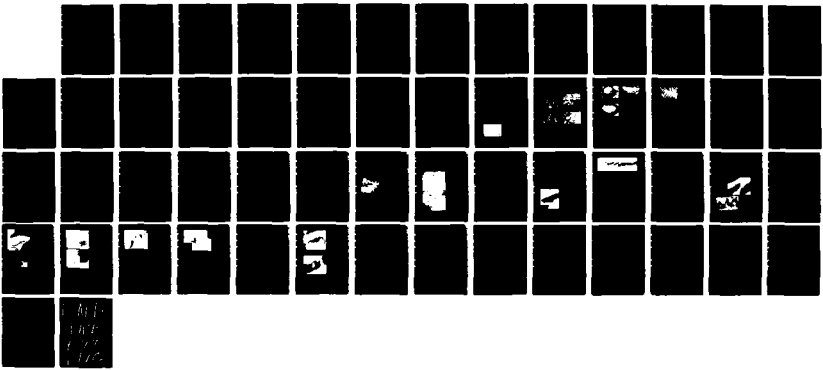
NO-A197 514

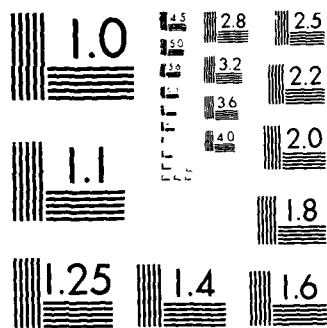
THE INVESTIGATION OF THE FRACTURE OF TITANIUM ALLOYS BY  
IN-SITU AND ANALY (U) VIRGINIA UNIV CHARLOTTESVILLE  
DEPT OF MATERIALS SCIENCE H G WILSDORF JUN 88  
UVA/525375/MS88/103 N88014-82-K-0389

272

UNCLASSIFIED

F/G 11/6 1 NL





MICROCOPY RESOLUTION TEST CHART  
NATIONAL BUREAU OF STANDARDS 1963 A

adiabatic shear initiation, since these forces are obviously not present in these tests.

#### 4. APPLICATION OF ADIABATIC SHEAR TO THE FRACTURE SEQUENCE

The relative positions of the various fracture surface features, as indicated in Figure 9, when combined with the concept of adiabatic shear at final separation can be used to generate a model of the sequence of events which occur during fracture. Calculations of the maximum possible temperature rise during uniform elongation clearly point out that prior to localization, only small (on the order of 60°C) temperature increases are possible. During localization, which, in our case, occurs in the form of primarily plane stress localization, this value can be increased approximately by an order of magnitude. This still leaves a tremendous increase unaccounted for if the melting temperature is to be reached.

Local strain values on the order of 12 are found under the unusual features and strains this high can be used to compute temperature increases far exceeding the melting point if constant material properties and fully adiabatic conditions are assumed. At these elevated temperatures, however, the strength of the material decreases tremendously, thereby decreasing the possible temperature rise. As an approximation of the possible temperature increases which can be expected under fully adiabatic conditions, yield strength versus temperature data for Ti-8w% Mn sheet was approximated by a linear and a bilinear curve, and this was then used to approximate the realistic temperature rise limit with strain. The results of these calculations are shown in Figure 13. These results, however, do not include any consideration of the strain rate hardening effects which are doubtless important during final separation and serve to increase the maximum achievable temperature.

The presence of spheroidized features on the fracture surfaces of samples strained at quasi-static rates is an indication that the applied strain rate of the test system does not necessarily provide an accurate measure of the rate of separation. Elastic energy stored in the testing system can be released into the final deforming volume at a rate controlled only by the elastic wave propagation velocity. When this

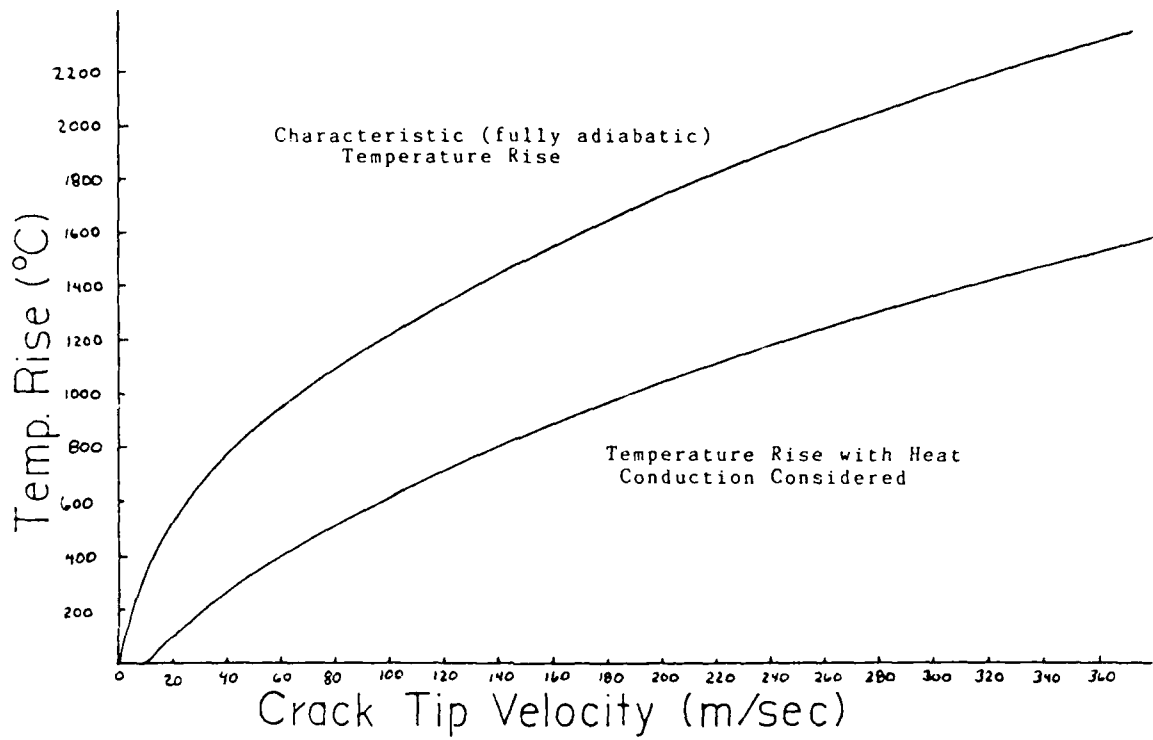


Figure 13. Characteristic (fully adiabatic) and predicted temperature increases with crack propagation at velocity  $v$  for a 10 micron process zone in Ti8Mn. Approximations used for predicted curve according to Rice and Levi [4].

stored elastic energy is considered, the final deformation rate can be seen to be nearly independent of the applied strain rate, even at the highest possible applied rates. This clearly agrees with our experiments and points out the importance of the elastic compliance of the loading system, be it a load frame or an engineering structure, in the initiation of adiabatic shear in this type of tensile fracture.

#### 5. ADIABATIC SHEAR AND THE SEQUENCE OF TENSILE SEPARATION

If the sequence of events which occur during separation culminate with adiabatic shear in high shear directions, the following model can be used to consolidate all of the proposed mechanisms after the final instability.

1) After necking begins, the central region of the sample begins to develop voids, further increasing the effective stress on the local cross section.

2) "Sample scale" shear bands begin to develop, greatly localizing the continuing deformation into high shear directions and increasing the local strain rate, as depicted in Figure 14a.

3) As the central voids grow and coalesce, the central crack extends towards the outer surfaces and the effective cross section continuously decreases.

4) When the effective stress and the resulting effective strain rate reach high enough values, adiabatic shear is initiated. At this point, as shown in Figure 14b, the strain rate and the strain increase to very high values, causing the temperatures to increase dramatically.

5) Final separation occurs along the thermally and geometrically softened high shear regions, forming the ISSZs and the OSSZs, as shown in Figure 14d.

The fact that Open Surface and Inner Surface Shear Zones are found at the interior and exterior edges of the shear lip areas can be explained by considering two configurations during final separation. In the first situation, depicted in Figure 15, the void sheet has grown to the outer edges of the shear lip and the final shear separation occurs through the outer edges of the sample and also through the neighboring voids which have not yet grown to coalescence. Figure 16 shows a more

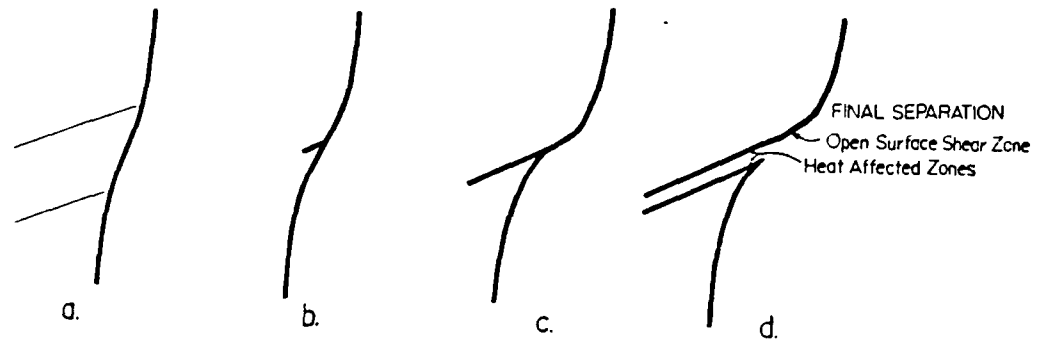


Figure 14. Model of formation of unusual surface features. a) Shear is localized into zone lying in high shear direction. b) Adiabatic shear is initiated at the intersection of the concentrated shear with an open surface. c) Propagation of adiabatic shear creates a narrow band of softened material. d) Separation along the softened region leaves Heat Affected Zones in localized areas adjacent to Open Surface Shear Zone.

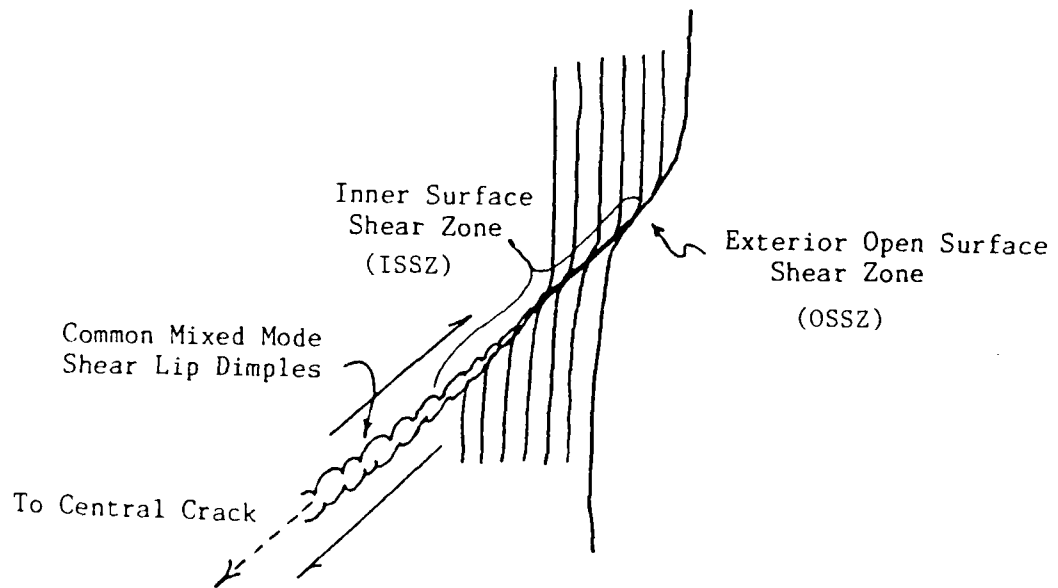


Figure 15. Final separation along adiabatic shear band located at the intersection of a separating shear lip and an external surface.

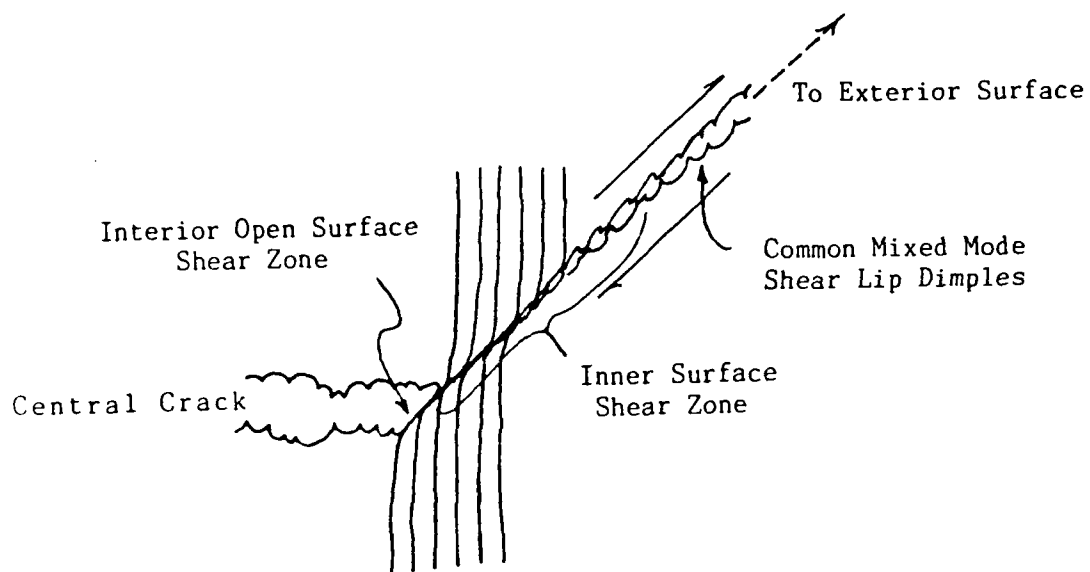


Figure 16. Final separation along adiabatic shear band located at the intersection of a separating shear lip and an internal crack which has been blunted at a grain boundary.

unusual situation, that of a void sheet which has not grown from the central crack directly outward and has, instead, has grown from the interior of the incipient shear lip towards the interior and exterior open surfaces. This situation is unusual if one considers the traditional moving crack tip model of separation, but it is consistent with the "double cup and cone" fracture process reported by earlier examinations of the various separation modes in tension [6].

A final mechanism which contributes to the high temperatures which cause the spheroidized surface structures found in this study, is the heating effect of the numerous dislocations needed to form the dimple walls during void coalescence. Dimple walls, which are universal in ductile fracture, have been demonstrated to result from cooperative slip in the final ligaments between growing voids, and this rupture of micro-ligaments requires a large number of dislocations concentrated into a very small volume. The resulting high local strains and strain rates provide the necessary requirements for considerable adiabatic temperature increase. Calculations [7] indicate that the temperature rise from dislocation motion during rupture of micro-ligaments amounts to several hundred degrees Celsius leading to local melting.

## 6. CONCLUSIONS

1) There is a continuous decrease in the workhardening rate of our Ti8Mn sheet tensile samples as the strain rate is increased from  $8.75 \times 10^{-4} \text{ sec}^{-1}$  to  $8.54 \times 10^0 \text{ sec}^{-1}$ .

2) Adiabatic heating of the gage length during uniform straining causes a measurable increase in the gage temperature, and in the Ti8Mn samples tested, this increase has a maximum value of approximately  $60^\circ\text{C}$ . Fully adiabatic thermal softening from this heating is not sufficient to account for the decrease in workhardening rate above strain rates of approximately  $6 \times 10^{-1} \text{ sec}^{-1}$ .

3) Stereo Scanning electron micrographs of the fracture surfaces show local regions which have a finely roughened (microroughened) surface texture and contain spheroidized dimple walls and surface debris. These unusual features always form at the boundaries of shear lip zones adjacent to dimple free bands (Open Surface Shear Zones).

4) Sections cut through the fracture surface show that these unusual features lie above localized bands of highly concentrated shear. Shear strain values greater than 12 have been measured in these bands, and the average width of the bands is approximately 2 microns.

5) The microroughened surfaces and spheroidized surfaces debris are formed in tests performed in an argon atmosphere, ruling out oxidation as the primary mechanism responsible for their formation.

6) Distinct flashes of light are emitted at separation, and the sources of emission can be localized to the surface areas containing the spheroidized surface features.

7) Initiation and propagation of adiabatic shear bands occurs during final separation in localized regions of some of the shear lip areas.

8) Adiabatic temperature increases during uniform extension, localization, crack propagation, adiabatic shear and final separation can combine to cause the final separating material to exceed the melting temperature in localized areas.

## REFERENCES

- [1] G. B. Olson, J. F. Mescall and M. Azrin, Shock Waves and High-Strain-Rate Phenomena in Metals, Plenum Press, New York (1981) p. 221.
- [2] R. S. Culver, Metallurgical Effects at High Strain Rates, (eds. R. W. Rhode, B. M. Butcher, R. J. Holland and C. H. Karues), Plenum Press, New York (1973) p.519.
- [3] D. E. Miller, "The Determination of Physical Properties of Ferrous and Non-Ferrous Structural Sheet Materials at Elevated Temperatures", AF Technical Report 6517, Wright Air Dev. Center (June 1954).
- [4] J. R. Rice and N. Levy, Physics of Strength and Plasticity, (ed. A. S. Argon), MIT Press, Cambridge, Mass. (1969) p.277.
- [5] E. A. Borisova, R. D. Glebova, A. A. Platnov and N. M. Sklyarov, Sov. Phys. Dokl., 20 (1975) p. 345.
- [6] G. Y. Chin, W. F. Hosford, Jr. and W. A. Backofen, Trans. TMS-AIME, 230 (1964) p. 437.
- [7] D. D. Makel, "Fracture Processes of Ti8Mn", Ph.D. Dissertation, University of Virginia (August 1987).

SECTION V  
A NUMERICAL MODEL FOR CALCULATING THE TEMPERATURE  
RISE AT CRACK TIPS IN A TITANIUM ALLOY

K. Jagannadham\* and H. G. F. Wilsdorf

ABSTRACT

Previous attempts to calculate the temperature rise at a moving crack tip used the continuum approach. The current model is based on the plastic deformation behavior in the process zone which is a smaller volume element within the classical "plastic zone." The essential elements of the new model are loading rate, plastic work rate, dislocation density, dislocation velocity, and plastic strain. The effects of the temperature rise at the tip simultaneous with crack propagation have been determined. The model predicts correctly the temperatures which developed during fracture as determined by experiment. In addition, new insights of the time-temperature relationship during fast crack growth were obtained.

\*Department of Materials Engineering, North Carolina State University,  
Raleigh, N. C. 27695-7916



A NUMERICAL MODEL FOR CALCULATING THE TEMPERATURE  
RISE AT CRACK TIPS IN A TITANIUM ALLOY

In first estimates of the temperature rise ahead of the crack tip by Krafft and Irwin [1,2], the plastic work term within the plastic zone was averaged and the uniform heat generated was used to determine the temperature rise. A refinement in the analysis by Rice and Levy [3] consisted of solving the heat equation with the integrated plastic work term over the entire plastic zone. The stresses and strains within the plastic zone obtained from the small scale yielding solutions of the Dugdale model were employed [4]. However, the analysis is still incomplete in the sense that the temperature at the crack tip is obtained using static crack approximations without including the effect of a simultaneous temperature rise. It is our opinion that the plastic work term changes in the region ahead of the tip in the plastic zone so that special emphasis should be given to the changes that occur within the process zone.

We have reconsidered the problem of determining the temperature rise in the region ahead of the crack tip. Our calculations, instead of using the continuum approach make use of the dislocation density and the associated plastic work term. The present formulations take into account the work hardening nature of the plastic zone through the equations connecting the flow stress and the dislocation density. Thus the process zone where the dislocation density far exceeds its magnitude elsewhere is clearly distinguished. The strain rate dependence of the frictional stress, the temperature dependence of the flow stress, the frictional stress and that of the thermal conductivity are also included in the present analysis to fit the experimental conditions. The expressions for the tensile component of the stress field associated with the Broberg dynamic elastic crack configuration [5] are used and further resolved for the shear stress component along the slip planes to account for the orientation by a factor equal to 0.5. The stress field expressions for the plastic crack configuration can be modified by shifting the crack tip stress singularity into the middle of the plastic

zone. The dimensions of the plastic zone are determined from

$$\tau = \tau_0 + \alpha G b \sqrt{\rho}$$

where  $\tau$  is the shear component of the stress field,  $\tau_0$  the frictional stress against movement of dislocations in the lattice,  $\alpha$  a numerical factor equal to 0.5,  $G$  the shear modulus,  $b$  the Burgers vector and  $\rho$  the dislocation density. When the stress associated with the crack is lower than the lattice frictional stress, no plastic deformation takes place. The plastic work rate,  $\dot{f}$  defined as the work done by the crack tip stress field in generating the plastic strain, is calculated from

$$\dot{f} = \sigma \dot{\epsilon} = \sigma \rho b v$$

where  $\dot{\epsilon}$  is the plastic strain rate and  $v$  the dislocation velocity in the plastic zone. The velocity of the dislocations in the region of the plastic zone also varies with the distance from the tip in the form,

$$v = (\tau - \tau_0) C_t \beta / G$$

where  $C_t$  is the transverse wave velocity,  $\beta$  is an adjustable parameter depending on the velocity of the crack itself. The parameter  $\beta$  can be varied to adjust the dislocation velocity and thus determine its effect on the temperature. The experimentally correlated expression for the velocity of the crack as a function of the loading rate parameter  $p$  in the form

$$V_c = (p/968)$$

is used where  $p$  is expressed in megabascals (meter)<sup>1/2</sup>/sec and  $V$  in meters/sec. A finite difference formulation of the one dimensional heat equation in the form,

$$\delta T / \delta t = (k/d C) \delta^2 T / \delta x^2 + \dot{f} / d \cdot C$$

is used where  $k$  is the thermal conductivity,  $d$  the density and  $C$  the specific heat. The region ahead of the crack tip in the plastic zone is divided into several intervals and the plastic work rate  $\dot{f}$  is determined

as a function of time at each point. Further substitution of the plastic work rate into the finite difference scheme (Korhonen and Kleemola [6]) enables the temperature at each point to be determined as a function of time.

Our analysis is applied to the Ti-10V-2Fe-3Al alloy for which the material parameters may be prescribed by the following values: the shear modulus,  $G = 41.9$  GPa, Poisson's ratio  $\nu = 0.32$ , the thermal conductivity  $k = 10.90$  w/m°C, density  $d = 4.65$  Mgm/m<sup>3</sup>, specific heat  $C = 4.9 \times 10$  J/Kg°C, and the Burgers vector  $b = 2.86 \times 10^{-8}$  cm. The frictional stress which opposes dislocation generation and movement is taken to be one tenth of the yield stress at  $\epsilon = 0.002$ . The dislocation drag force used in calculation of dissipated plastic energy, is assumed to be arising from phonon scattering. This term which is estimated to be the major contribution to the viscous forces acting is given by

$$\tau_{\text{drag}} = Bv = \frac{3kT}{10C_L b^2} \frac{v}{(1-v^2/c^2)^{\frac{1}{2}}}$$

which already includes the temperature dependence and the relativistic effects. The temperature and strain rate effects on the frictional stress opposing dislocation movement in the lattice are given by

$$\tau_0 = (1300 + 21.28 \ln \dot{\epsilon}) f(T)$$

where  $f(T) = (1 - 0.4 T/350)$  for  $0 < T < 350^\circ\text{C}$ , and  $f(T) = (0.75 - 0.5T/1200)$  for  $350 < T < 1200^\circ\text{C}$ .

The temperature dependence of the shear modulus is taken in the form

$$G(T) = G(0) (1 - 0.5T/1200) \text{ for } 0 < T < 1200^\circ\text{C}$$

whereas that of the thermal conductivity and specific heat is given by

$$k(T) = k(0) (1 + 0.6T/1200),$$

$$C(T) = C(0) (1 + 0.6T/1200).$$

Crack growth takes place initially elastically until the frictional stress is exceeded. Then crack growth will start and the crack will proceed into its own plastic zone. The width of the plastic zone generated at the crack tip is a function of the velocity of the crack, loading rate and the temperature dependent frictional stress. In order

to ascertain the influence of the crack velocity and loading rate, we have determined the various parameters: temperature at the crack tip, dislocation density at the tip, plastic work dissipated at the tip, dislocation velocity at the tip, and the plastic strain at the tip. These are shown in Figures 1 to 4 for two crack velocities. In this comparison it becomes clear that the softening arising from the dissipation of energy at the tip has a major influence on the various parameters. At slower crack velocity, the crack tip moves into the plastic zone at a speed slow enough so that it continues to increase the temperature rapidly. However, when the crack velocity is higher, the crack tip moves into a region where the temperature is lower which has the effect to slow down the temperature increase in relation to the origin of the time scale. Further, faster crack growth leads to higher strain rates and therefore, the frictional stress is higher also. As a result, the region of plastic zone formation is reduced. The effects on various parameters are illustrated in Figures 1 to 4. We have chosen two crack velocities  $V_c = 0.4$  m/sec and  $V_c = 0.8$  m/sec at the loading rates of  $p = 680 \text{ MPa}\sqrt{\text{m}} \text{ sec}^{-1}$  and  $p = 890 \text{ MPa}\sqrt{\text{m}} \text{ sec}^{-1}$  respectively. The dislocation velocity ahead of the crack tip is chosen such that  $\beta = 10$  for  $V_c = 0.4 \text{ m sec}^{-1}$  and  $\beta = 20$  for  $V_c = 0.8 \text{ m sec}^{-1}$ .

It is seen from Figures 1 and 2 that the temperature ahead of the crack tip for  $V_c = 0.4 \text{ m sec}^{-1}$  is higher than for  $V_c = 0.8 \text{ m sec}^{-1}$ . This leads to a lowering of the frictional stress and the shear modulus whereas the thermal conductivity and specific heat increase. As a result, the dislocation density (Figures 1 and 2), plastic work dissipated (Figures 1 and 2), dislocation velocity (Figure 3) and the plastic strain (Figure 4) are higher at slower crack growth rates.

These results are important in understanding the formation of molten regions at the dimple walls of fractured surfaces. High crack velocities are indeed responsible for exceeding the melting point at specific regions. These experimental results do not follow from the previous analytical calculations which predicted only the changes of a temperature rise that occurs in the plastic zone. Those previous calculations do not give the adiabatic temperature changes that take place around voids and the rupture of microligaments. It is clear from

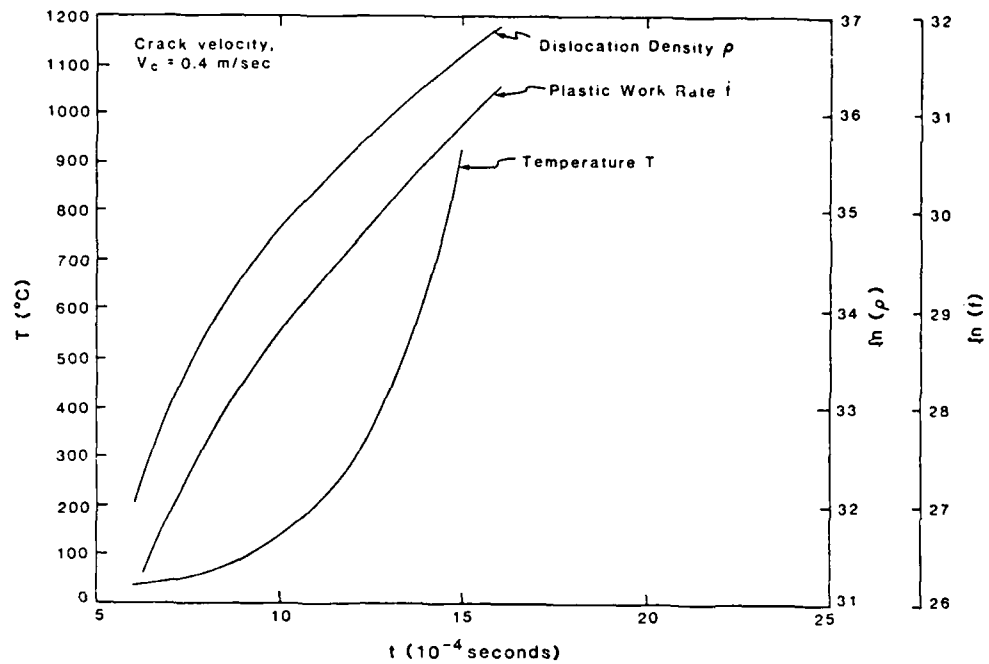


Figure 1. Calculated temperature rise for crack velocity  $V_c = 0.4$  m/sec. Also shown is dislocation density  $\rho$  and plastic work rate  $\dot{f}$ .

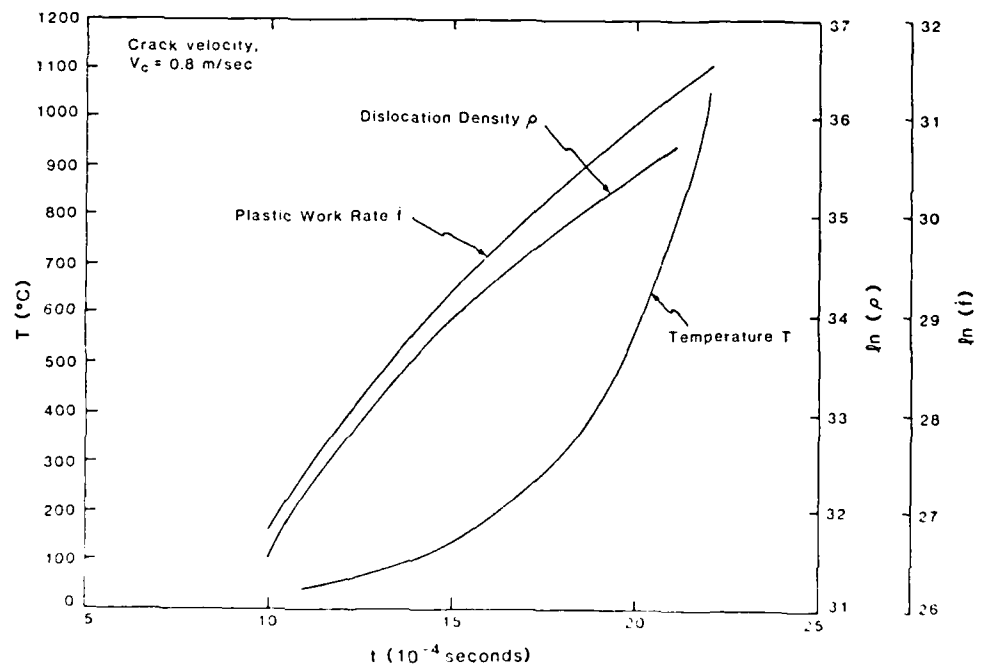


Figure 2. Calculated temperature rise for crack velocity  $V_c = 0.8$  m/sec. Note the shift to higher values on the time scale.

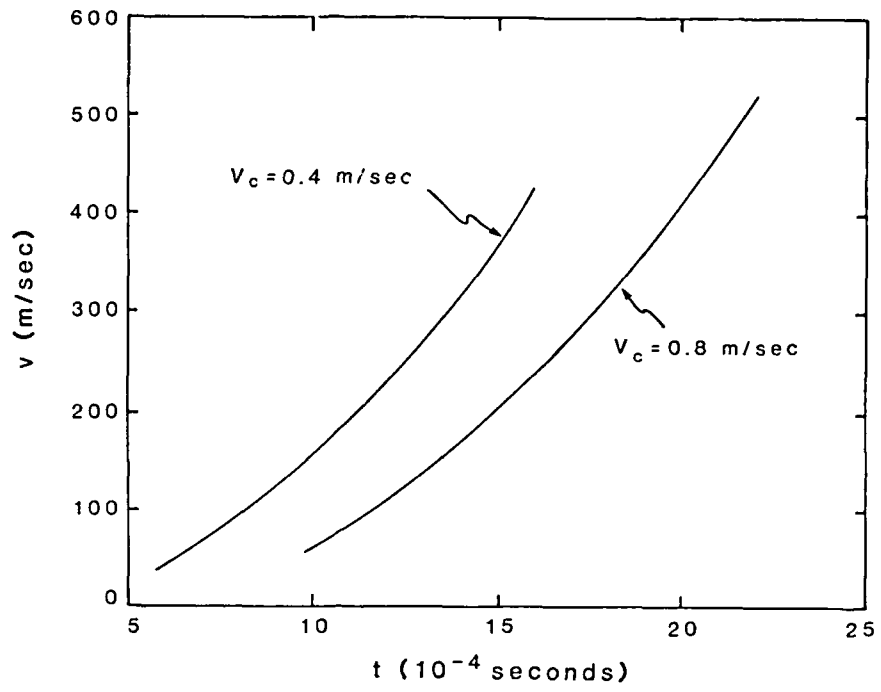


Figure 3. Calculated increase of dislocation velocities in time for two crack velocities.

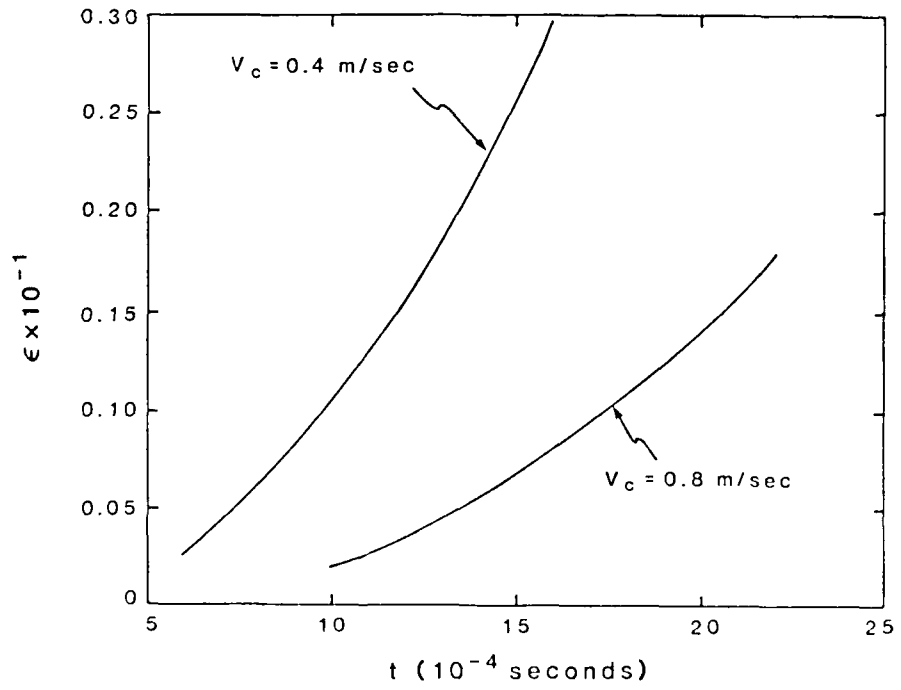


Figure 4. Calculated increase in strain vs. time for two crack velocities.

our calculations that the melting point can be exceeded only at ligaments involved in the coalescence of voids at the crack tip where the strain rate is exceedingly high. If the temperature rise in the crack tip plastic zone alone were to explain the formation of molten zones, the result should be that such molten zones are formed everywhere along the edge of the crack. When the crack tip moves very fast, the size of the "plastic zone" is very small and as a result the width of the molten areas formed before the final failure occurs should also be smaller. This general result is born out by the distribution of molten areas on the fracture surface. Rapid glide processes within the ligaments associated with the crack tip contribute the additional temperature increase in the order of 300°C to 500°C [7,8]. The temperature increase calculated from the model alone is well below the melting point since these calculations have not included the rupture of microligaments between voids which are reduced in thickness at this stage to about 1 μm. Earlier work has shown that the deformation to final rupture follows strictly the rules of crystal plasticity, i.e., shear is as predicted along crystallographic glide planes and glide directions [9]. Modifying a model for the calculation of heat production through dislocation avalanches by Freundenthal and Weiner [10] the following equation was used:

$$T = \frac{\tau v b N}{2 \pi k} \left( \frac{\pi \kappa}{\lambda v} \right)^{\frac{1}{2}},$$

again  $v$  is the dislocation velocity,  $N$  is the number of dislocations,  $\lambda$  is the length of travel, and  $\kappa = k/d \cdot C$ . Estimating the shear stress for this alloy at a temperature of 1200°C to be 190 MPa and assuming that dislocation avalanches are moving on glide planes 20 nm apart which corresponds to a maximum dislocation density of  $10^{12} \text{ cm}^{-2}$ , one finds a temperature increase of 540°C. This brings the localized heating above the melting point.

## REFERENCES

1. J. M. Krafft, Correlation of plane strain crack toughness with strain hardening characteristics of a low, a medium, and a high strength steel. Appl. Mater. Res. 3 (1964) 88-101.
2. J. M. Krafft, and G. R. Irwin, Symposium on Fracture Toughness Testing. ASTM, STP No. 381 (1965) 114-129; Philadelphia, PA.
3. J. R. Rice, and N. Levy, In Physics of Strength and Plasticity. Ed. A. S. Argon (1969) 227-293. MIT Press, Cambridge, MA.
4. D. S. Dugdale, J. Mech. Phys. Solids 8 (1960) 100.
5. K. B. Broberg, Arkiv for Fysik 18 (1960) 159.
6. A. S. Korhonen and H. J. Kleemola, Met. Trans. 9A (1978) 979.
7. J. D. Bryant, D. D. Makel and H. G. F. Wilsdorf, Mater. Sci. Eng. 77 (1986) 85-93.
8. J. D. Bryant, D. D. Makel and H. G. F. Wilsdorf, In Metallurg. Appl. of Shock-Wave and High-Strain-Rate Phenomena. Eds. L. E. Murr, K. P. Staudhammer and M. A. Meyers, pp. 723-739. M. Dekker, New York (1986).
9. H. G. F. Wilsdorf, Acta Metall. 30 (1982) 1247-1258.
10. A. M. Freudenthal and J. H. Weiner, J. Appl. Phys. 27 (1956) 44.

Appendix I  
Appendix II  
Presentations  
Publications  
Degrees Awarded

## Observations on the Effect of Temperature Rise at Fracture in Two Titanium Alloys

J. D. BRYANT, D. D. MAKEL and H. G. F. WILSDORF

Department of Materials Science, University of Virginia, Charlottesville, VA 22901 (U.S.A.)

(Received February 27, 1985; in revised form April 26, 1985)

### ABSTRACT

Two titanium alloys, the  $\alpha$ - $\beta$  alloy Ti-8Mn and the metastable  $\beta$  alloy Ti-10V-2Fe-3Al (where the compositions are given in approximate weight percent), were strained to fracture at strain rates of up to  $28 \text{ s}^{-1}$  at room temperature. Investigation of their fracture surfaces by scanning electron microscopy revealed droplet-like features at the rim of dimples and raised features in the regions between and inside dimples. These were interpreted as molten remnants of micro-ligaments. A calculation of the affected volume, taken from stereo-photogrammetry data, confirmed this view. It was clear from experimental evidence that the melting point was exceeded in micro-ligaments only at the moment of the final separation, and a model is proposed to explain the temperature rise from contributions of three mechanisms which can be distinguished phenomenologically. Numerical calculations have shown that the melting point can be exceeded under adiabatic conditions on account of the alloys' high yield stress, low heat conductivity and high stress concentration factor.

### 1. INTRODUCTION

Metals which fail by tensile forces in the ductile fracture mode initially undergo uniaxial deformation until necking occurs, followed by cup-and-cone fracture or rupture. At least 90% of the plastic deformation is transformed into heat which, in standard specimens and at normal strain rates, hardly affects the test. However, at strain rates  $\epsilon$  higher than  $10^{-2} \text{ s}^{-1}$  the test may be influenced by a temperature rise

[1] if the flow stress of the material is temperature sensitive.

For fracture tests at high strain rates the temperature rise in the specimen due to uniform straining almost coincides with the development of heat at the crack tip. Local heating at the crack tip has been investigated theoretically by Priest [2] and by Rice and Levy [3]. The relationship between stress intensity factor  $K$  and strain-hardening exponent  $n$  at high crack propagation rates was treated by Krafft and Irwin [4]. Reliable measurements of the temperature at a moving crack tip in metals are unavailable and this lack of experimental data seems to have prevented progress in the understanding of this important problem.

The objective of this investigation is to elucidate the energy dissipation at the crack tip in two titanium alloys by concentrating on the temperature rise in a rapidly moving crack. A study of fracture surfaces using scanning electron microscopy (SEM) has been carried out and the novel features seen have been interpreted. It appears that for the first time the temperature rise in a rapidly moving crack, final separation in alloys has been obtained from experimental data within a narrow range. A model is being advanced to explain the temperature rise at the crack tip for ductile metals.

### 2. EXPERIMENTAL PROCEDURE

Tensile specimens were prepared from the metastable  $\beta$  titanium alloy Ti-10V-2Fe-3Al and the  $\alpha$ - $\beta$  alloy Ti-8Mn (where the compositions are given in approximate weight percent). The Ti-10V-2Fe-3Al specimens were fabricated with a 19.05 mm  $\times$  4.4 mm gauge section, with the diameter increasing to

9.53 mm in the threaded section. Flat bar specimens were made from Ti-8Mn, with a gauge length of 8.9 mm, a thickness of 0.68 mm and a width of 2.4 mm. The heat treatments were chosen to maximize the ductility of the specimens. To accomplish this, a solution treatment temperature of 780 °C was used to transform the as-received Ti-10V-2Fe-3Al materials into a two-phase alloy with roughly 10% of the alloy left in the  $\alpha$  phase in the form of large (10-50  $\mu\text{m}$ ) plates. The formation of smaller strengthening precipitates was accomplished during a 500 °C aging. For the Ti-8Mn specimens a solution temperature of 800 °C was used, followed by a furnace cooling to 600 °C. This alloy developed large acicular  $\alpha$  precipitates. Specimens with identical thermomechanical histories were subjected to different strain rates, the slowest of which was 0.0031  $\text{s}^{-1}$  up to 7.8  $\text{s}^{-1}$ . The tests were performed on an MTS hydraulic tester. As stress-strain data at the higher strain rates could not be recorded on the standard  $x$ - $y$  plotter, a retention tube oscilloscope was used which read the signals of the load and stroke outputs directly. Calibration was provided through the  $x$ - $y$  plotter by simultaneous recording during a low strain rate test. Typical oscilloscope traces are given in Fig. 1.

Fracture surfaces were examined in a scanning electron microscope and stereo-micrographs were taken of different regions. In addition, the deformation underlying the



Fig. 1. A retention tube oscilloscope was placed in the  $x$  vs.  $y$  mode and used to display the load cell output against the stroke output directly. Stress-strain data could thus be recorded up to the highest strain rate achievable on the MTS (cross head speed, 0.25  $\text{m s}^{-1}$ ). See Table 2.

fracture surface was examined using a profile technique. The upper portion of the gauge length containing the fracture surface was plated with nickel to preserve details of the surface. The sample was then mounted in Bakelite and ground down to expose the central core of the tensile specimen. Through the action of two different etchants, the nickel plating could be brought down to the level of the titanium alloy, allowing an unobstructed view of the microstructure and plastic region directly below the fracture surface.

### 3. RESULTS

The features of the fracture surface were seen to vary with the strain rate employed. While both the rapidly strained and the slowly strained specimens failed primarily by transgranular fracture, the features within the transgranular regions were strikingly different. While the slowly strained specimens exhibited an undulating terraced surface (there was evidence of decohesion along  $\alpha$  phase precipitates), at higher strain rates the fracture path appeared unperturbed by the precipitate morphology. In these regions the fracture surface is more uniform, in both the size and the shape of the dimples on the surface as well as in the smoother overall topography. Figure 2 compares the transgranular fracture surfaces of Ti-10V-2Fe-3Al specimens subjected to high and low strain rates. Complete tensile data are given in Table 1.

Larger shear lips were found on more rapidly deformed specimens, as well as an increase in the reduction in area. Failure through the void sheet mechanism was more prevalent in the specimens strained at higher rates. Several of the high speed tests resulted in fracture by the cup-and-cone mode usually associated with more ductile metals.

Some anomalous features within the shear lips of the fracture surface were found. In Figs. 3 and 4 the typical dimple structure and surface texture from a transgranular region can be compared with regions within the shear lip. The surface in this region, although dimpled, is rougher in appearance. Higher magnification shows the surface to be populated with small hemispherical bumps (Figs. 5

and 6) in the regions between and inside the dimples. In addition, the perimeter of the dimples in this region is decorated with small spherical globules. The smoothness of these features suggested that they represent the globularized remains of micro-ligaments. They were found not only on the specimens subjected to the higher strain rates but also, occasionally, on the fracture surfaces of the

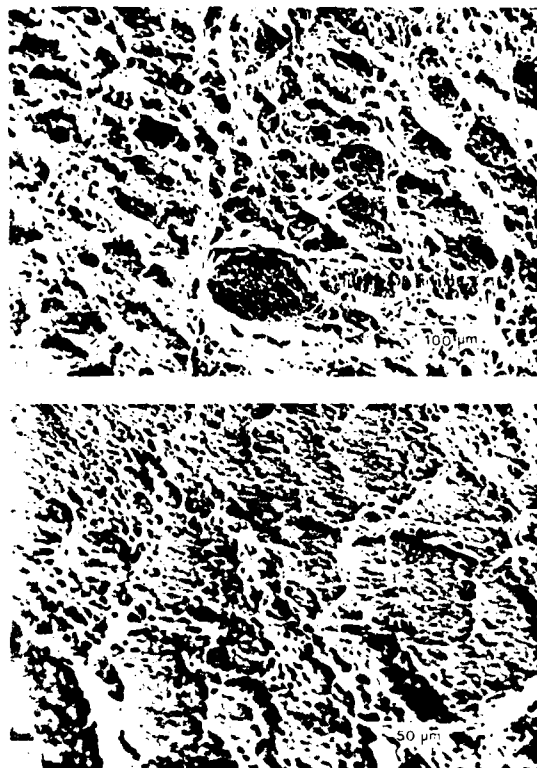


Fig. 2. The variation in fracture mode for Ti-10V-2Fe-3Al can be seen by comparing these two micrographs. (a) The slowly pulled ( $\dot{\epsilon} = 0.0053 \text{ s}^{-1}$ ) specimen shows a perturbed undulating fracture surface, compared with the (b) smooth uniformly dimpled surface of the rapidly pulled specimen ( $\dot{\epsilon} = 13 \text{ s}^{-1}$ ).

TABLE I

Results of tensile tests

Specimen	Crosshead speed (mm s <sup>-1</sup> )	$\dot{\epsilon}$ (s <sup>-1</sup> )	$\epsilon$ (%)	Reduction in area (%)	Yield strength (MPa)
Ti-8Mn	250	28.1	14.0	15.0	1369
Ti-10V-2Fe-3Al(E7)	100	5.3	17.2	12.0	1180
Ti-10V-2Fe-3Al(E8)	250	13.2	14.7	19.6	1180

samples strained at lower strain rates. In both cases, these features were always found only near the outer edge of the specimen, within the shear lip.

A reasonable postulate as to the origin of the rough textured surfaces within and

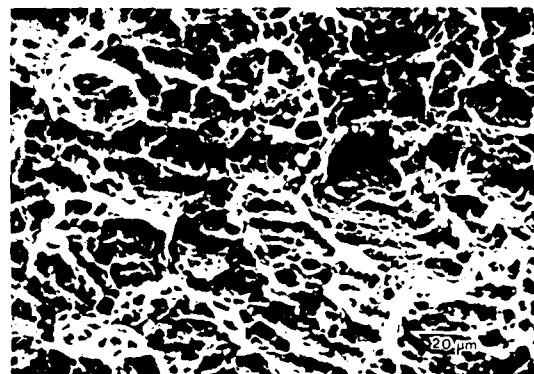


Fig. 3. A higher magnification shows the deep irregular dimpled surface typical of a transgranular fracture surface for Ti-10V-2Fe-3Al.

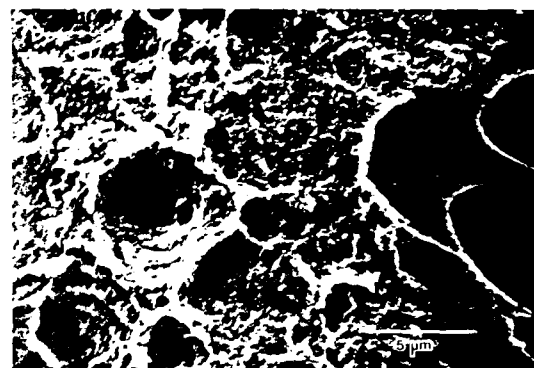


Fig. 4. The dimple structure in the shear lip is markedly different. This micrograph shows the transition of normal transgranular fracture surface topography to the shallow roughened surface near the perimeter of the tensile Ti-8Mn specimen.

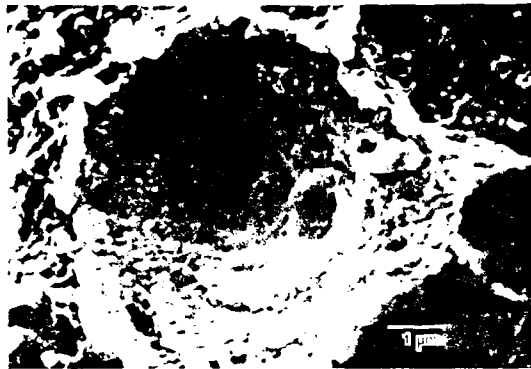


Fig. 5. The globularized features in the shear lip are evidenced in this micrograph of the fracture surface of Ti-8Mn deformed at a strain rate of  $28 \text{ s}^{-1}$ .

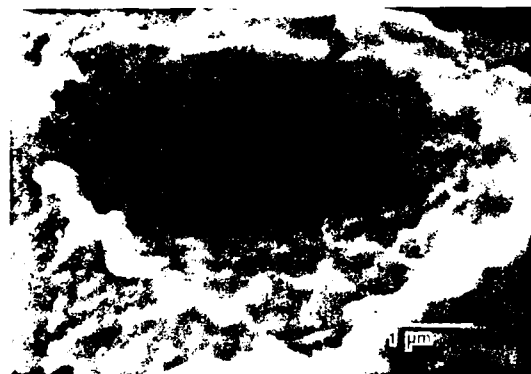


Fig. 6. The remnants of micro-ligaments in Ti-10V-2Fe-3Al on the perimeter of the dimples are seen to be globularized. The area between and inside the dimples is populated with small hemispherical irregularities.

between the dimples is that the fracture surface in these regions has been coated with the molten remains of micro-ligaments. The hemispherical features would result from the action of surface tension, as in splat cooling. To test the feasibility of this interpretation, the volume of material in the micro-ligaments was estimated and compared with the minimum volume of material required to yield the hemispherical surface features. On the assumption of a triangular ligament cross-section with a height and a base of  $0.3 \mu\text{m}$ , the volume of material within this ligament, if it is imagined to extend to the perimeter of the entire dimple would be sufficient to coat the area completely within the dimple with hemispherical fragments of radius  $0.1 \mu\text{m}$  or less.



Fig. 7. The depth of the plastic zone can be quantified by noting the deformation of the  $\alpha$  primary precipitates in the Ti-10V-2Fe-3Al alloy directly below the fracture surface.

The profile technique allowed for quantitative measures of the plastic zone beneath the fracture surface by noting the distortion of the underlying precipitates (Fig. 7). As with the features on the fracture surface itself, the size of the plastic zone was seen to be a function of the strain rate. Measurements showed the plastic zone to vary widely even within a single specimen. The higher strain rates, however, tended to produce shallower plastic zones.

To obtain a better view of the underlying microstructure in the regions characterized by the globularized features, a technique was developed wherein the nickel plating was selectively etched away from the fracture surface such that the direction of the shear which operated in that region could be determined (Fig. 8). It was seen that in these regions the precipitates immediately beneath the fracture surface were heavily deformed, with shear strains as high as 5.

#### 4. DISCUSSION

The experimental evidence from SEM stereo-micrographs suggested convincingly that in some areas of the fracture surface the alloy's melting point had been exceeded at the moment of final separation. However, it is clear from an analysis of fracture surfaces studied in this investigation that the overall fracture surface must have been well below the melting temperature of the alloy. Only small patches from a few micrometers to



Fig. 8. By overetching the protective nickel plating of the fracture surface, the direction and magnitude to the strain in the immediate region below the fracture surface of Ti-8Mn can be estimated.

about 20  $\mu\text{m}$  in diameter showed droplet-like features, and these observations were made on the shear lips only. Therefore, the calculation of the temperature rise  $\Delta T$  will be made by estimating and summing the temperatures produced by (i) the overall plastic deformation before the crack develops, (ii) the plastic deformation at the crack tip and (iii) the rupture of micro-ligaments.

It will be assumed that the temperature increase due to the plastic deformation preceding fracture is adiabatic. This seems to be justified since (i) the alloys have a limited ductility, (ii) the time from the start of the test to fracture is for most specimens

of the order of a fraction of a second and (iii) the heat conductivity of titanium alloys is very low. The adiabatic temperature rise for a homogeneous solid and uniform deformation is usually given by

$$\Delta T_1 = \frac{1}{\rho c} \int_0^{\epsilon} \sigma \, d\epsilon \quad (1)$$

where  $\rho$  is the density,  $c$  is the specific heat,  $\sigma$  is the stress and  $\epsilon$  is the strain. If work hardening is assumed to occur according to the usual power law,  $\Delta T_1$  can be calculated as follows:

$$\Delta T_1 = \frac{1}{\rho c} \frac{\sigma}{n+1} \epsilon^{n+1} \quad (2)$$

with  $n$  being the strain-hardening exponent. When the values listed in Table 2 were used and eqn. (2) was employed, a temperature increase  $\Delta T_1$  of 21  $^{\circ}\text{C}$  for Ti-8Mn was found. The value for  $\epsilon_1$  is of course estimated, but it appears to be reasonable in view of the relatively small strain to fracture. Since  $\Delta T_1$  is small compared with the melting point of the alloys, a variation in  $\epsilon_1$  is of little consequence to the final result. From an equation that has been employed in a more general approach to the temperature rise in tensile specimens [1], *i.e.*

$$\Delta T_1 = \frac{\sigma \epsilon}{\rho c} \quad (3)$$

TABLE 2  
Physical data for two titanium alloys

Quantity	Symbol	Values for the following alloys	
		Ti-10V-2Fe-3Al	Ti-8Mn
Yield stress	$\sigma_0$	1180 MPa	1370 MPa
Burgers vector	$b$	$2.86 \cdot 10^{-8}$ cm	$2.95 \cdot 10^{-8}$ cm
Density	$\rho$	$4.65 \text{ Mg m}^{-3}$	$4.70 \text{ Mg m}^{-3}$ (at 1200 MPa)
Specific heat	$c$	$4.9 \cdot 10^2 \text{ J kg}^{-1} \text{ }^{\circ}\text{C}^{-1}$	$4.95 \cdot 10^2 \text{ J kg}^{-1} \text{ }^{\circ}\text{C}^{-1}$
Thermal conductivity	$k$	$1.09 \cdot 10 \text{ W m}^{-1} \text{ }^{\circ}\text{C}^{-1}$	$1.09 \cdot 10 \text{ W m}^{-1} \text{ }^{\circ}\text{C}^{-1}$ (at 1200 MPa)
Poisson's ratio	$\nu$	0.32	0.30
Stress intensity factor	$K$	$70 \text{ MPa m}^{1/2}$ (at 20 $^{\circ}\text{C}$ )	NA
Young's modulus	$E$	110 GPa	114 GPa
Shear modulus	$G$	41.7 GPa	43.2 GPa
Work hardening exponent	$n$	0.1	0.1
Strain to fracture	$\gamma_f$	0.18	0.14

NA, not available.

a value of 33 °C can be determined; this appears to be high. Although unimportant for the titanium alloys investigated here,  $\Delta T_1$  due to uniform straining may affect the temperature rise at crack tips for highly temperature-sensitive metals and alloys.

With the initiation of a crack in the center of the specimen, the plastic deformation becomes localized in front of the crack tip. Rice and Levy [3] have calculated this temperature increase. They assumed a non-hardening plastic solid, a small plane strain plastic zone at the tip and the absence of thermomechanical coupling effects. This model considers the case of a moving heat source ahead of the crack tip (at this point the model is converted to a moving coordinate system). For the stationary crack the plastic work rate  $f(x, y, t)$  is determined as

$$f(x, y, t) = \frac{4(1-\nu)\sigma_0^2}{\pi G} \cdot \left(1 - \frac{x}{\omega}\right)^{1/2} \delta_D(y) \frac{d\omega}{dt} \quad (4)$$

where  $\omega$  is the maximum dimension of the plastic zone. For the moving coordinate system the plastic work rate is

$$g(x, y) = \frac{2(1-\nu)\sigma_0^2}{\pi G} \cdot \log \left\{ \frac{1 + (1-x/\omega)^{1/2}}{1 - (1-x/\omega)^{1/2}} \right\} \delta_D(y) V \quad (5)$$

In this equation,  $\delta_D(y)$  is the Dirac delta function employed to account for the discontinuity in displacement at the plastic zone and  $V$  is the crack speed. For the running crack with a growing plastic zone, the work rate would be the sum of  $g(x, y)$  and  $f(x, y, t)$ . Thus the  $g(x, y)$  term will dominate under the condition that  $V$ , the speed of the crack tip, greatly exceeds the plastic zone growth rate  $d\omega/dt$ . When the equations for the configuration of localized heat generation are combined, the temperature rise  $\Delta T(r, \theta, \tau)$  at the stationary crack tip is

$$\Delta T_2 = \frac{\tau_0^2}{2\pi K G} \int_0^\tau \int_0^{\omega(\tau)} \left[ 1 - \left\{ \frac{r}{\omega(\tau)} \right\}^2 \right]^{1/2} \cdot \exp \left\{ -\frac{r^2}{4a^2(t-\tau)} \right\} dr \frac{d\omega(\tau)}{d\tau} \frac{d\tau}{t-\tau} \quad (6)$$

The equivalent equation for the temperature rise near the head of a moving crack tip is more sensitive to the distribution of the work rate (sites of heat generation) and is described by

$$\Delta T_2 = \frac{\pi^{1/2} (1-\nu^2) K^2}{2 E(\rho c k)^{1/2}} \left( \frac{V}{\omega} \right)^{1/2} = 0.886 \frac{(1-\nu^2) K}{E(\rho c k)^{1/2}} \left( \frac{V}{\omega} \right)^{1/2}$$

By substitution of

$$\omega = \frac{\pi K^2}{8 \sigma_0} \quad (7)$$

it is found that

$$\Delta T_2 = 1.414 \frac{(1-\nu^2) K \sigma_0}{E(\rho c k)^{1/2}} V^{1/2} \quad (8)$$

In this model, it should be noted that the temperature increase is greatest at the crack tip itself and drops to a negligible level at the plastic zone boundary.

The calculations were made with the room temperature values of the stress intensity factor  $K$  and the stress  $\sigma_0$  which do not take into account the heating in front of the crack tip during the actual crack propagation. It is known that, in high strength alloys,  $K$  is increasing while  $\sigma_0$  will be lower with increasing temperature [5-10]. Since no specific measurements were found in the literature, the balance between  $K$  and  $\sigma_0$  with rising temperatures could not be assessed. In order to gain an impression of the effect of an increasing stress intensity factor on  $\Delta T_2$ , the dependence of  $\Delta T_2$  on  $V$  was calculated for the two alloys in accordance with eqn. (8). Three values for  $K$  were assumed and  $\Delta T_2$  was plotted against the speed  $V$  of the crack in Fig. 9. It is seen that at  $V = 20 \text{ m s}^{-1}$  the temperature rise is about 900 °C when  $K = 60 \text{ MPa m}^{1/2}$  for Ti-10V-2Fe-3Al. At such a steep temperature rise at a moderate crack speed it is reasonable to expect that  $K$  would approach  $140 \text{ MPa m}^{1/2}$  at the time of separation. The calculation shows that with  $K = 100 \text{ MPa m}^{1/2}$  a temperature of about 1500 °C would have been reached. In Fig. 10,  $\Delta T_2$  has been plotted against  $K$  for three crack speeds. When a reasonable value for  $V$  of  $50 \text{ m s}^{-1}$  for Ti-10V-2Fe-3Al is taken, it is found that  $\Delta T_2$  equals the

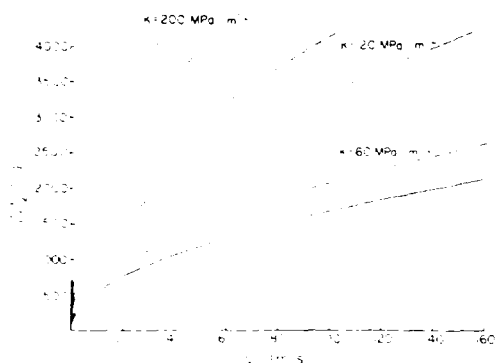


Fig. 9. Temperature rise at the crack tip dependent on the crack speed  $V$  for three stress concentration factors  $K$ : ---, Ti-10V-2Fe-3Al; —, Ti-8Mn.

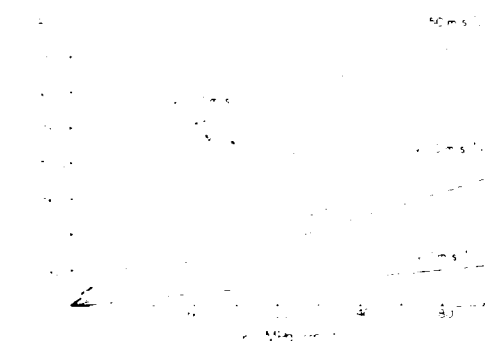


Fig. 10. Dependence of the temperature rise at the crack tip on the stress concentration factor  $K$  for three crack speeds  $V$ : ---, Ti-10V-2Fe-3Al; —, Ti-8Mn.

melting point with the room temperature  $K$  value of  $70 \text{ MPa m}^{1/2}$ . Despite the uncertainty of the changes that will affect  $K$  and  $\sigma_0$  during crack propagation, the calculations show convincingly that the temperature rise at the crack tip is substantial and can approach the melting temperature.

The final contribution to the temperature increase is caused by deformation, leading to the rupture of many micro-ligaments that completes the fracture. After the growth of voids to a maximum size the remaining micro-ligaments were reduced in thickness to about  $1 \mu\text{m}$  with lengths of a few micrometers as judged from earlier studies on a variety of metals and alloys [11, 12]. The deformation of these micro-ligaments can be estimated to be an order of magnitude larger than during macro-necking [13]. On

account of the small size of micro-ligaments, it is appropriate to use a dislocation model for calculating the temperature rise at the point of their rupture.

A number of attempts have been made to calculate the temperature that can be obtained from the energy release of moving dislocations on glide planes [14, 15]. These models assume a dislocation to be a moving source of heat. Freudenthal and Weiner [14] define the heat flux  $q$  for  $n$  dislocations producing a total slip distance  $\delta = nb$  as

$$q = \frac{\tau \delta v}{nmb} \quad (9)$$

with  $\tau$  being the shear stress;  $v$  is the dislocation velocity and  $mb$  is the distance between dislocations. After addressing the heat conduction from a heat source of length  $\lambda$ , Freudenthal and Weiner arrive at the following equation:

$$\Delta T_3 = \frac{\tau}{mK_t} \left( \frac{\kappa \lambda v}{\pi} \right)^{1/2} \quad (10)$$

where  $K_t$  is the thermal conductivity and  $\kappa$  is the thermal diffusivity ( $\kappa = K_t/c\rho$ ). An equivalent equation for  $\Delta T_3$  was derived also by Eshelby and Pratt [15].

Actual calculations show that  $\Delta T_3$  rises by a few degrees celsius if one glide plane with, say, 500 dislocations moving at a speed of  $10^5 \text{ cm s}^{-1}$  is involved. However, Eshelby and Pratt pointed out that the temperature would rise to higher levels if more slip planes are active; clearly,  $\Delta T_3$  increases with the amount of shear and smaller distances between active planes, leaving  $\tau$  unchanged. Recently, the above model has been extended by Armstrong *et al.* [16] who considered the temperature rise when piled-up dislocations on one slip plane were suddenly released and, in addition, the relationship between shear band density and  $\Delta T_3$ . However, since the titanium alloys investigated here do not contain hard particles behind which large pile-ups could form, their model appears to be not applicable for the deformation of micro-ligaments at the point of separation.

Attempts to adopt this model without or with the proposed modifications were not successful. The problem is to accommodate a very complex geometrical shape, i.e. the rim of dimples down to a given depth, to

discrete glide planes, varying glide distances, varying distances between glide planes and varying stresses to the framework of the model. It appeared to be more appropriate in the light of the geometry of the rapidly deforming micro-ligaments to apply a form of the Freudenthal-Weiner model in which glide takes place simultaneously on the most active parallel glide planes in a given volume. In that case a group of dislocations can be considered to move on one plane between "insulating" planes (Fig. 11). Obviously, this model provides for the upper limit of  $\Delta T_3$  and a  $\Delta T_3$  calculation according to eqn. (10) would then represent the lower limit. The temperature rise for active planes near the "insulating" planes would have an intermediate value. When the heat conduction in the  $x$  direction is neglected, the temperature distribution given by Carslaw and Jaeger [17] is

$$\Delta T_3 = \frac{ql}{2K_t} \left\{ \frac{\kappa x}{vl^2} + \frac{3y^2 - 6yl + 2l^2}{6l^2} - \frac{2}{\pi^2} \sum_{n=1}^{\infty} \frac{1}{n^2} \cos\left(\frac{n\pi y}{l}\right) \times \exp\left(-\frac{\kappa n^2 \pi^2 x}{vl^2}\right) \right\} \quad (11)$$

$l$  is the distance between the active glide plane and the "insulated" boundary plane and should have a very small value; then the second term of eqn. (11) can be neglected. When  $q$  according to eqn. (9) is inserted, to

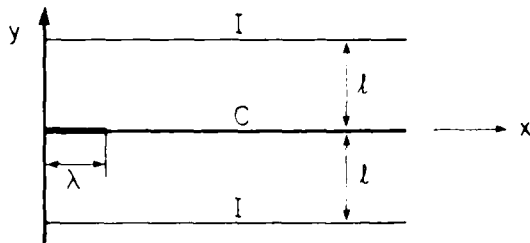


Fig. 11. Model of dislocation motion on glide plane C which takes place in a crystal volume with many active glide planes. Planes I have been called "insulating planes" by Freudenthal and Weiner [14] to signify that virtually no heat loss to the surrounding volume takes place with reference to plane C. (Drawing according to ref. [14].)

a first approximation the following equation is obtained:

$$\Delta T_3 \approx \frac{\tau \delta}{2l\rho c} \quad (12)$$

In calculating  $\Delta T_3$ , for the rupture of ligaments, values for  $\tau$ ,  $\rho$  and  $c$  have to be taken that are adjusted for operating at the increased temperature at the crack tip which with  $\Delta T_1 \approx 30^\circ\text{C}$  and  $\Delta T_2 \approx 1500^\circ\text{C}$  is estimated to be  $1530^\circ\text{C}$ . Since measurements for the three parameters above are not available for the alloys investigated, the following estimates were based on the trend of similar titanium alloys at higher temperatures.  $\tau$  is assumed to be  $350\text{ MPa}$ ,  $\rho$  to equal  $4.3\text{ g cm}^{-3}$  and  $c$  to equal  $0.8 \times 10^7\text{ erg g}^{-1}\text{ }^\circ\text{C}^{-1}$ . If it is assumed that the maximum dislocation density is involved in the rupture process (*i.e.* about  $10^{12}$  dislocations  $\text{cm}^{-2}$ ) and further a local strain for micro-ligaments is calculated ( $\gamma_m \approx 5$ ), then  $\delta = 150\text{ nm}$  and  $l = 35\text{ nm}$ . According to eqn. (12) the temperature rise  $\Delta T_3$  equals  $308^\circ\text{C}$ . This result is not claimed to be precise; however, there can be little doubt that  $\Delta T_3$  is in the range of several hundred degrees Celsius. Comparable calculations using the equation of Eshelby and Pratt [15] for a number of closely spaced active glide planes gives results for the temperature rise of the same order of magnitude.

The sum  $\Delta T_1 + \Delta T_2 + \Delta T_3$  is about  $1840^\circ\text{C}$  and thus exceeds the melting point of the alloys by about  $240^\circ\text{C}$ . If the extremely short time for the rupture of micro-ligaments is considered, it is reasonable to say that, at the moment when the melting point is exceeded, the voids contain a vacuum and a deposition of molten or vaporized material can take place on the dimple surfaces which remain in their original shape. This would explain the minute hillocks and the frozen droplet configurations observed (Figs. 5 and 6) while in border cases, where only the utmost tips have reached the melting point, no such deposits are visible (Fig. 4).

The theoretical treatment is based on the contention that the processes leading to the temperature rise are adiabatic. The low heat conductivity of the titanium alloys, which is 40 times lower than that of copper, was given earlier as an important reason. Adiabatic effects, however, should also be discernible

in the behavior of the plastic zone. Figures 7 and 8 were evaluated and in places show a shear of about 5 which is a clear indication that, within the given time interval, adiabatic conditions prevailed during crack propagation. A case for adiabatic behavior in titanium during dynamic plastic deformation has been made earlier by Culver [18].

## 5. CONCLUSIONS

Experimental evidence pertaining to the temperature at a crack tip was obtained by SEM stereo-photogrammetry of fracture surfaces. The novel features observed were droplet-like irregularities at the rim of dimples and numerous small bumps at the bottom of the corresponding dimples. An estimate of the affected volume of micro-ligaments supported the view that in certain limited areas a very small volume was heated above the melting point at the moment of final separation. The experimental conditions, *i.e.* deformation to fracture at a high strain rate, and certain properties of the alloys such as high yield stress, low thermal conductivity and high stress concentration factor made a temperature rise above the melting point a distinct possibility.

It was thought that three mechanisms could be distinguished which were associated with the temperature rise in the specimen: (i) uniform straining to necking; (ii) energy dissipation at the crack tip; (iii) deformation to fracture of micro-ligaments. Calculations of temperature increases for the three mechanisms yielded approximately 30 °C, 1500 °C and 300 °C respectively and thus supported the conclusions above. The proposed model is a first attempt to rationalize a melting phenomenon at the fracture of two titanium alloys and more detailed computer calculations are in progress.

## ACKNOWLEDGMENTS

This research was sponsored by the Office of Naval Research under Contract N00014-82-0309, NR 031-840. We wish to thank Dr. Bruce MacDonald for his interest and valuable discussions.

## REFERENCES

- 1 H. P. Stuwe, *Z. Metallkd.*, **61** (1970) 180.
- 2 A. H. Priest, *Proc. Int. Conf. on Dynamic Fracture Toughness*, Welding Institute, American Society for Metals, Metals Park, OH, 1977, p. 95.
- 3 J. R. Rice and N. Levy, in A. S. Argon (ed.), *Physics of Strength and Plasticity*, Massachusetts Institute of Technology Press, Cambridge, MA, 1969, p. 177.
- 4 J. M. Krafft and G. R. Irwin, *Proc. Symp. on Fracture Toughness Testing and its Applications*, *ASTM Spec. Tech. Publ.* **381**, 1965, p. 114.
- 5 H. G. Baron, *J. Iron Steel Inst., London*, **182** (1956) 354.
- 6 K. J. Marsh and J. D. Campbell, *J. Mech. Phys. Solids*, **11** (1963) 49.
- 7 U. S. Lindholm, A. Nagy, G. R. Johnson and J. M. Hoegfeldt, *J. Eng. Mater. Technol.*, **102** (1980) 376.
- 8 A. K. Sechdev and J. E. Hunter, *Metall. Trans. A*, **13** (1982) 1063.
- 9 S. L. Semiatin, G. D. Lahoti and S. I. Oh, in J. Mescall and V. Weiss (eds.), *Material Behavior Under High Stress and Ultrahigh Loading Rates*, Plenum, New York, 1983, p. 119.
- 10 A. Kobayashi and N. Ohtani, in K. Kawata and J. Shioiri (eds.), *High Velocity Deformation of Solids*, Springer, Berlin, 1978, p. 208.
- 11 H. G. F. Wilsdorf, *Mater. Sci. Eng.*, **59** (1983) 1.
- 12 H. G. F. Wilsdorf, *Scr. Metall.*, **17** (1983) 1209.
- 13 H. G. F. Wilsdorf, *Z. Metallkd.*, **75** (1984) 154.
- 14 A. M. Freudenthal and J. H. Weiner, *J. Appl. Phys.*, **27** (1956) 44.
- 15 J. D. Eshelby and P. L. Pratt, *Acta Metall.*, **4** (1956) 560.
- 16 R. W. Armstrong, C. S. Coffey and W. L. Elban, *Acta Metall.*, **30** (1982) 2111.
- 17 H. S. Carslaw and Jaeger, *Conduction of Heat in Solids*, Oxford University Press, New York, 1948, 224.
- 18 R. S. Culver, in R. W. Rohde, B. M. Butcher, J. R. Holland and C. H. Karnes (eds.), *Metalurgical Effects at High Strain Rates*, Plenum, New York, 1973, p. 519.

## Low Energy Dislocation Structures Associated with Cracks in Ductile Fracture

K. JAGANNADHAM

Materials Engineering Department, North Carolina State University, Raleigh, NC 27650 (U.S.A.)

H. G. F. WILSDORF

Department of Materials Science, University of Virginia, Charlottesville, VA 22901 (U.S.A.)

(Received January 31, 1986)

### ABSTRACT

Ductile fracture in metals and alloys is preceded by work hardening and necking. Microstructural processes, previously explored by *in situ* transmission electron microscopy, have been re-examined in the context of interactions between glide dislocations and crack tips. In this, the parameters which significantly influence experimental findings have been critically reviewed and theoretical aspects of ductile fracture have been examined including the principle of energy minimization. Consideration was given to the displacement of the stress singularity ahead of the crack tip on account of the plastic zone and the effects of thermal instabilities during crack growth.

Crack propagation occurs in ductile materials mostly by void coalescence. This requires the nucleation of microcracks ahead of the crack tip as was observed experimentally in agreement with theoretical expectations. Microcrack initiation was seen to take place at dislocation cell walls which represent the most frequently formed low energy dislocation configurations in work-hardened metals. As a consequence, too, the formation of a plastic crack and its growth in a virgin crystal are distinctly different from the nucleation and growth of a crack in a crystal with a well-defined cell structure that was formed through prior deformation. Dislocation multiplication is considered to take place by the supercritical bowing of the longest free link lengths present within the cell walls, as also observed experimentally. The microstructural changes that take place in the plastic zone ahead of the crack tip are found to be more important in fracture than the microscopic processes immediately at the tip itself.

### 1. INTRODUCTION

Ductile fracture of metals and alloys is more complex than other types of failure. This is so mainly because a variety of microstructural changes take place in the material long before final separation on account of the extensive plastic deformation that occurs before fracture. This causes substructural changes associated with dislocation configurations which depend on several variables characteristic of the specific materials tested, and similarly on the imposed conditions of deformation including strain rate and temperature.

The work hardening of a material during plastic deformation consists of an increase in the stress required for dislocation multiplication and movement. It is controlled by specific materials parameters including crystallography, precipitates and stacking fault energy, for example. These parameters and the resulting microstructural changes should be incorporated into theoretical models of crack initiation and propagation, since an understanding of ductile fracture of a material obtained on the basis of the work-hardening curve alone necessarily remains rather qualitative. However, using various empirical relations, it becomes possible to correlate the changes in microstructural features with the ductile behavior preceding fracture. To a considerable extent, these are derived from experiments wherein foils of metals and alloys are strained to fracture by *in situ* techniques in the transmission electron microscope with simultaneous observation of changing dislocation patterns. These have become very powerful tools in the drive towards our understanding of ductile fracture [1]. In this it has become clear that a general principle of energy minimization of disloca-

tion configurations is most useful, namely experience has shown that low energy dislocation structures are developed about cracks, so that energy minimization introduces a natural organization principle and simplification into the complex phenomena [2-4]. As a result, it becomes possible to model the crack behavior in terms of work hardening and low energy dislocation configurations.

## 2. GENERAL CONSIDERATIONS

Fracture of a material takes place when a crack can propagate on decreasing energy of the system. The total energy of the crack configuration consists of different energy terms that contribute to the system [4]. Of several stress-strain singularities that can exist in solids, cracks are among the most important. The elastic crack tip is associated with an inverse square root type of singularity of the stress field [5]. For plastic crack tips, the nature of the singularity was analytically derived and it was shown that it is of the same type but shifted into the plastic zone developed in front of the crack tip [6]. The spatial variation in the crack tip stress field is centrally important in determining the plastic deformation associated with the tip. Thus, generation and movement of dislocations in the region ahead of the tip take place under the action of the crack tip stress field.

The classification of ductile and brittle fracture is derived from the nature of the crack tip [7, 8]. If it is energetically favorable to nucleate dislocations in front of the crack tip and simultaneously to develop ledge steps, the fracture behavior is classified as ductile. A propagating crack which intermittently generates lattice dislocations and ledge steps on the crack surface represents a moving source of dislocations. Ductile fracture is conceived in the general literature as follows. In highly ductile materials, extensive dislocation generation and movement take place at the crack tip so that the stress field associated with the crack is screened by the plastic zone. In this, the sharp elastic crack tip is replaced by a rounded and blunted tip surrounded by the plastic zone. While this view is correct, it is incomplete in not taking into account the microstructural changes that actually take place ahead of the crack in the plastic zone,

even though their influence on the crack tip is most important. Specifically, quite commonly the dislocations in the plastic zone ahead of the crack tip rearrange so as to form cell walls (the classical low energy substructure) and, if so, plentiful new crack nucleation sites are thereby provided. Therefore, the importance of the principle of minimization of energy in the generation of the dislocation substructure associated with the crack tip cannot be overemphasized.

The formation of the dislocation configurations ahead of the crack tip is influenced by several parameters dependent on the nature of the metal or alloy. For example, in close-packed f.c.c. and h.c.p. metals and alloys, the formation or presence of stacking faults affects the mobility of the dislocations [9], and thence the resulting dislocation structures, in accordance with the stacking fault energy. In particular, in low stacking fault energy materials such as stainless steels, slip is confined to narrow slip zones so that dislocation cell structures cannot readily form [1]. Instead, other low energy configurations such as dipolar mats may be generated [10]. As a result, the mechanism of fracture becomes different in low compared with high stacking fault energy f.c.c. metals. Additionally, point defects generated by moving dislocations in the region close to the crack tip and their condensation to stacking fault tetrahedra provide another important microstructural feature. Its major effect is that these interfere with dislocation movement.

The above certainly does not exhaust the list of important defect effects in fracture. The interactions of dislocations with several other defect configurations have been documented especially in close-packed f.c.c. and h.c.p. structures [11]. Radiation-induced voids and void clusters interact directly with a growing crack in that the crack front cuts through spherical voids and soft coherent second-phase particles [12, 13]. Thus the resistance of the material to crack propagation is significantly altered also by these. However, hard non-coherent second-phase particles distributed in a soft matrix act as sources of dislocations which in turn react with the substructure developed in the plastic zone. The stress field associated with the crack nucleates voids along the non-coherent interface of the hard second-phase particles

because of the incompatibility of deformation [14]. Void nucleation along dislocation cell walls [15] and other high energy dislocation configurations such as two-phase interfaces [14] are accompanied by a decrease in energy of the configuration. The nucleation of voids and their coalescence constitute a major mechanism of ductile fracture. Other microstructural features such as grain boundaries and twin boundaries also are sources of dislocations [11]. At the same time, the existence of these features provides obstacles to the movement of the crack tip and, at times, significantly alters its path. Other important lattice and crystal defects affecting crack propagation are illustrated in Fig. 1.

The generation and movement of dislocations in metals and alloys cause plastic deformation, and the density of dislocations increases with increasing plastic strain. As a result the free link length of dislocations that can act as sources for further dislocations decreases. Eventually, low energy configurations such as dislocation cell structures are formed provided that the mobility of dislocations is adequate and at least two different Burgers vectors are available. In the absence of a crack tip and if a uniform stress is applied,

the stress-strain relation associated with the plastic deformation of metals and alloys has been derived from the various stages of the development of dislocation substructures [16]. The presence of a crack (and the stress field associated with it) introduces additional dislocations into the region of the plastic zone. Thus, if  $\rho_{\text{appl}}$  is the density of dislocations due to a uniform applied stress and  $\rho_{\text{crack}}$  the density of dislocations due to the crack tip stress field, assuming a simple superposition, the total density of dislocations is given by  $\rho_{\text{total}} = \rho_{\text{appl}} + \rho_{\text{crack}}$ . On the basis of much experimental evidence and the theory of work hardening the flow stress  $\tau$  is related to the total dislocation density through a simple relation

$$\tau = \tau_0 + \alpha G_1 b \rho^{1/2} \quad (1)$$

where  $\tau_0$  is the frictional stress against dislocation movement,  $G_1$  the shear modulus,  $b$  the Burgers vector of the lattice dislocations in the material and  $\alpha$  a numerical factor nearly equal to 0.5. An important application of the principle of minimization of energy is that the dislocations rearrange in the form of a cell structure. The minimization of strain energy associated with the cell structure compared with a random arrangement of dislocations [3] accounts for a similar simple relation for the cell size  $L$  which has been known empirically for a long time and is given by

$$L = \frac{K G_1 b}{\tau - \tau_0} \quad (2)$$

where  $K$  is a numerical factor equal to about 10. Thus the formation of dislocation cell structures is considered as inevitable provided that the conditions mentioned earlier exist. Other low energy dislocation arrangements are also considered possible if the cell structure cannot be formed under restricted mobility of dislocations. The dislocations generated ahead of the crack tip follow a different pattern from those in uniaxial deformation because of the specific nature of spatial stress field variations associated with the crack tip. The interaction of dislocations generated because of the crack tip stress field with those present as a result of the uniform applied stress also typically causes dislocation cells and in any event forms an important step in the growth behavior of the crack [17].

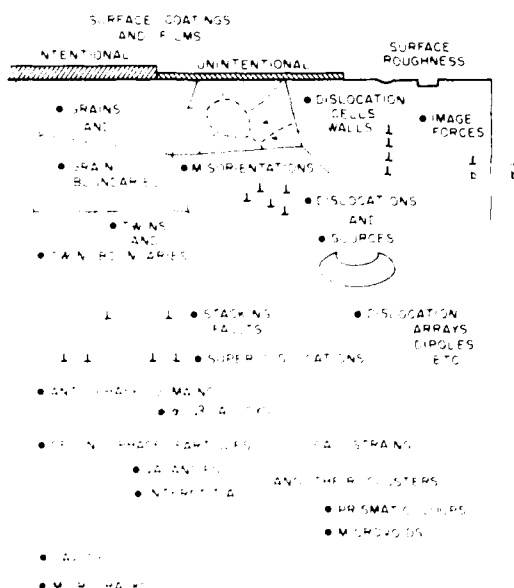


Fig. 1. Crack initiation and propagation in ductile fracture are dependent on crystal defects. The most important of these defects are depicted in this schematic drawing of the microstructural regime of ductile fracture [1].

In this paper, experimental findings are presented on *in situ* fracture carried out in the transmission electron microscope. The behavior of cracks in ductile metals and alloys in general, and the dislocation substructure developed in front of the crack tip in particular, will be given special attention. Further, the influence of several microstructural features on the ductile fracture of the material is described. The experiments on *in situ* fracture carried out in the electron microscope can provide large amounts of information depending on several important factors. For example, cracks introduced in well-annealed foils when subjected to a small deformation at very low strain rates can illustrate the mechanism of generation and movement of dislocations on the operating slip planes under these rarified conditions. Also the formation of ledge steps that are responsible for the opening of the crack surfaces and rounding of the crack tip can be illustrated [4]. However, if *in situ* experiments are carried out on foils with no perforation and initially not transparent or semitransparent to an electron beam then, as deformation progresses and the foil becomes thinner, the nucleated cracks and voids grow in the presence of a well-defined cell structure. As a result the foil becomes transparent to the electron beam because of thinning, enabling direct characterization of the dislocation substructure and its influence on the growth of the cracks formed during deformation (compare Section 5). The latter type of experiment is relatively more important in actually understanding ductile fracture in macroscopic specimens. Similarly, other *in situ* experiments are useful in understanding the influence of stacking fault energy, the number of available slip systems at the crack tip and the lattice frictional stress associated with the material. Thus, it becomes possible to understand in detail the different mechanisms of fracture as influenced by different parameters in different materials. At the same time, certain common features of crack growth behavior in ductile fracture can be obtained through these studies.

Thus, as outlined, *in situ* fracture carried out in the electron microscope with a proper choice of the experimental parameters is important to the understanding of ductile fracture. The thickness of the foil, the strain rate

and temperature at which the foils are deformed and the operating voltage of the transmission electron microscope are some of the conditions that can be controlled. The microstructural mechanisms of fracture can be correlated with the material parameters. Direct observation and simultaneous dynamic recording of the substructural changes enable this type of experiment to be very versatile. Modern analytical facilities, namely scanning and transmission attachments, microdiffraction capabilities and high voltage operating conditions for examining thicker foils, make these experiments very advantageous in gaining a better understanding of the mechanisms of ductile fracture in macroscopic specimens.

### 3. EXPERIMENTAL OBSERVATIONS OF CRACK GROWTH IN ANNEALED THIN FOILS

*In situ* deformation and fracture experiments can be classified broadly into two categories, namely the first category wherein a perforation is present as a result of jet thinning of the foil to produce an electron-transparent area, and the second wherein a non-transparent or semitransparent area is present without a perforation. In the first category, the foil area close to the perforation is fully transparent to the electron beam and is free from dislocations if the starting material was well annealed. The cracks present at the edge of the perforation move into the foil under the action of the applied load. Usually, the electron-transparent foils are so thin that plane stress conditions exist in the foil on applying the load [1]. In addition, the free surface exerts forces which affect the mobility of the dislocations. As a result, no more than one or two slip systems become operative at the crack tip in such thin foils while the formation of low energy dislocation substructures is hindered because of the constraints exerted by the free surface. The image force present in these foils also changes the orientation of dislocations with respect to the free surface such that on its slip plane (whether or not this is the one usually expected) the dislocation is normal to the surface. Macroscopic fracture is far more complex in such foils in that dislocations with several different Burgers vectors are produced because of slip on several systems.

In contrast, the simplicity of plastic deformation ahead of the crack tip in very thin foils illustrates some of the microscopic processes at the tip, namely dislocation generation and movement and simultaneous formation of ledge steps on the crack surface. Electron microscopy observations of a foil deformed *in situ* in the tensile stage shown in Fig. 2(a) illustrates the features mentioned. The two slip systems inclined to the crack and leading to ledges on the crack surfaces as revealed by the slip traces, and the resulting opening of the crack faces, are a significant feature of this micrograph. The dislocation substructure in the foil, which consists of dislocation loops and loop debris, is similar to the characteristic deformation of the matrix in b.c.c. metals irrespective of the presence of the crack.

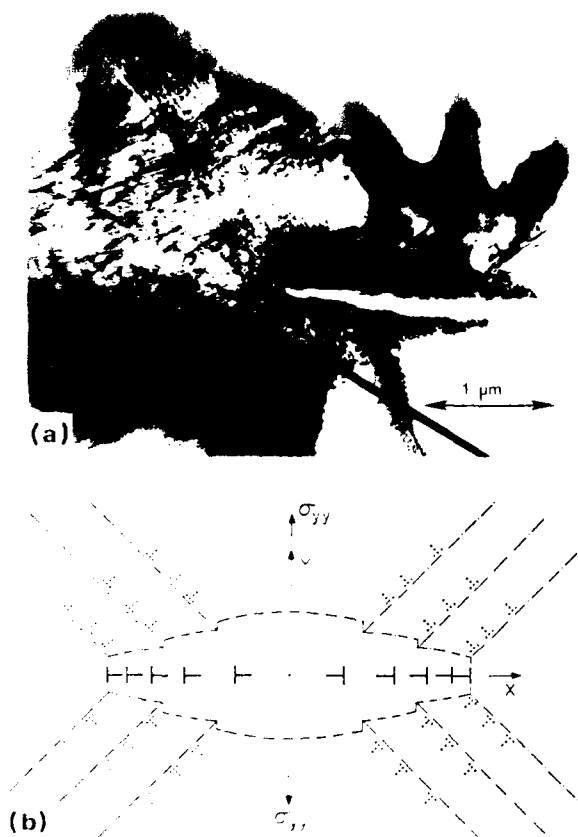


Fig. 2. (a) Crack tip in Nb-10at.%V produced by transmission electron microscopy *in situ* straining. It should be noted that two slip systems are active in front of the tip. (b) Schematic illustration for the discrete dislocation model of a continuous plastic crack (—, lattice dislocations; ---, crack dislocations. (Reprinted by permission of Internationaler Buch-Verlag G.m.b.H. from ref. 18.)

However, the dense dislocation substructure present in line with the direction of the crack in the foil is associated with the crack tip singularity [19]. A schematic illustration of this type of crack growth behavior wherein the crack tip generates dislocations intermittently and moves forward in the manner originally proposed by Orowan [20] is shown in Fig. 2(b).

The following points have to be taken into account when evaluating results obtained from *in situ* straining of very thin foils in the transmission electron microscope to fracture. The limited number of slip systems by which plastic deformation takes place prevents the formation of low energy dislocation cell structures which are found in thicker foils. Also, because of the lack of dislocations which cut each other and thus do not produce jogs, point defect production is absent. As a result, experiments carried out with very thin foils are not representative of macroscopic ductile fracture behavior of a material. Ductile fracture involves extensive plastic deformation, the generation and movement of dislocations with several different Burgers vectors, and the production and interaction of point defects.

#### 4. EXPERIMENTAL OBSERVATIONS OF CRACK NUCLEATION AND GROWTH IN DEFORMED MATERIALS

In this section, experiments in the second category wherein a foil is thinned to a thickness without producing a perforation and thus more nearly resembles a bulk sample are treated. A small area of the foil may be now semi-transparent to a high voltage electron beam or the whole foil may be left intentionally non-transparent. Now deformation in the *in situ* stage gives rise to extensive deformation of the whole foil, provided that suitable foil orientations are chosen. If so, plastic deformation on multiple slip systems generating dislocations with different Burgers vectors representative of deformation in macroscopic specimens takes place with simultaneous foil thinning to make portions of the foil electron transparent. Work hardening of the material due to plastic deformation and dislocation interaction is observed in such experiments [1]. In metals and alloys with a high mobility of dislocations, rearrangement into low energy

dislocation cell structures with alternating orientation of the lattice within the cell walls in the opposite direction has been documented [21], as shown in Fig. 3(a). A brief description of cell walls and their influence on the fracture behavior of the material is in order at this point.

In a uniformly strained material, the cell size  $L$  given by eqn. (2) is obtained, which is commensurate with the average applied stress. However, in the region near the crack tip, a

smaller cell size of dislocations is expected because of further subdivisions of cells. The cell walls are, in some way, similar to grain boundaries wherein two lattices of different orientations are joined together. When glide dislocations with different Burgers vectors rearrange and form cell walls of width  $w$ , the net Burgers vector of the dislocations in the cell wall is responsible for the misorientation and the strain energy associated with it. The larger the dislocation density and the width

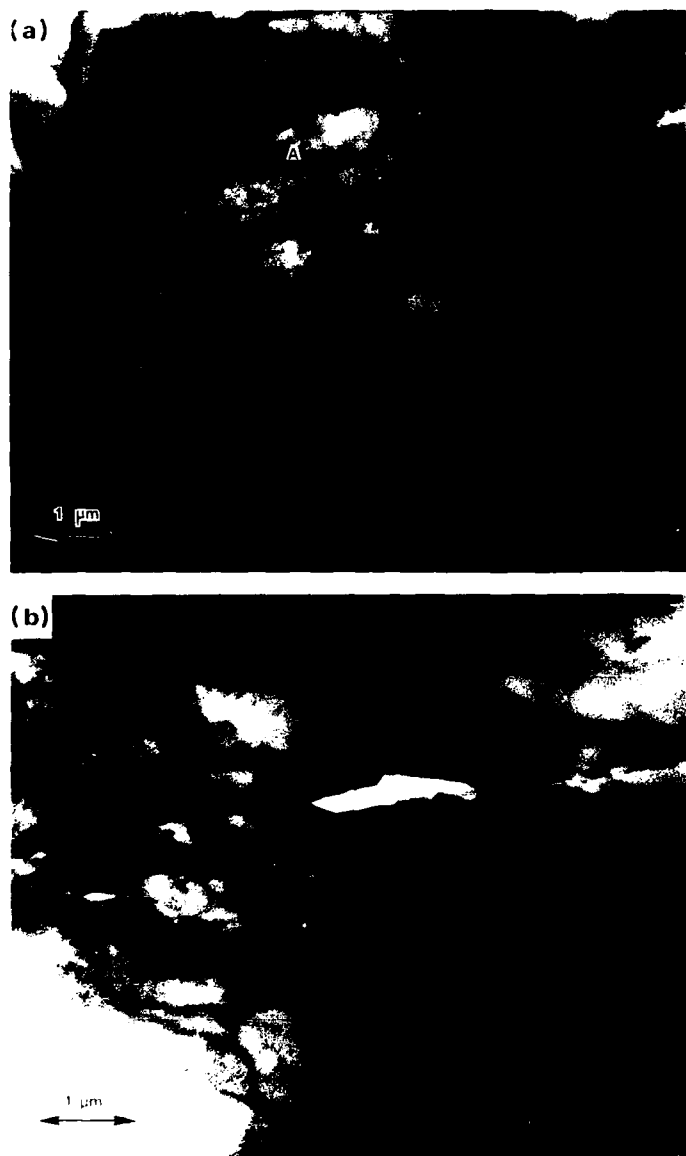


Fig. 3. Direct observation of initiation of microcracks in beryllium at dislocation cell walls during high voltage electron microscopy *in situ* straining of a foil approximately  $4 \mu\text{m}$  thick: (a) cell walls formed during straining; (b) the largest microcrack should be compared with region A in (a).

of the wall, the larger should be the strain energy associated with these cell walls. Misorientations between  $20^\circ$  and  $30^\circ$  and cell sizes of  $0.1\text{--}0.4\ \mu\text{m}$  have been recorded whereas the dislocation densities within cell walls average about  $5 \times 10^{11}\ \text{cm}^{-2}$  [1]. If dislocations within cell walls are to act as sources, free dislocations of link length of the order of  $10\ \text{nm}$  have to be activated within cell walls of misorientation greater than  $10^\circ$ . The necessary stress (about  $5 \times 10^9\ \text{Pa}$  for beryllium) suggests that nucleation of microcracks is an alternative to further glide dislocation production which becomes energetically favorable, a result substantiated by observations during *in situ* fracture and documented in Fig. 3(b) [15, 21].

A schematic illustration of a cell wall containing a cross-grid of screw dislocations is shown in Fig. 4(a) with the nucleation of an elastic crack along the interface. The strain energy associated with the misorientation across a boundary between the cell wall and the region free from dislocations is responsible for the nucleation of an elastic crack. The stress-free boundary conditions that exist at the free surfaces of an elastic microcrack

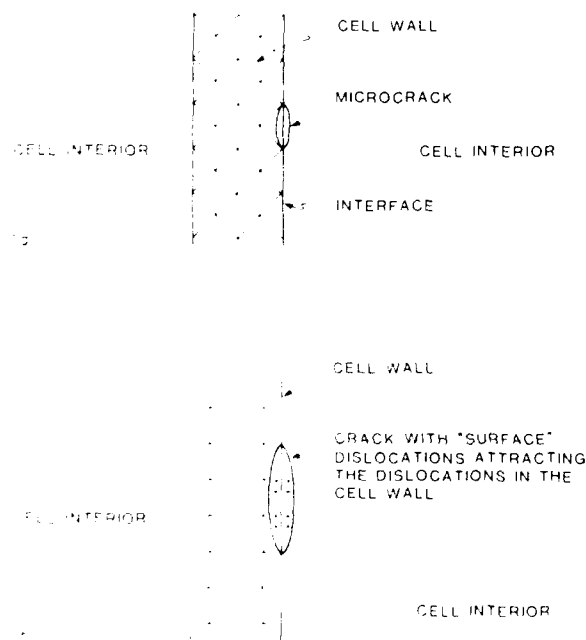


Fig. 4. (a) Schematic illustration showing microcrack initiation at a cell wall. (b) dislocation model of microcrack initiation at a cell wall. Surface dislocations have been drawn in a smaller size.

can be understood as the presence of surface dislocations of the opposite sign called anticrack dislocations [4]. The stress field due to the anticrack dislocations cancels with the stress associated with the lattice dislocations in the cell walls. A schematic illustration of the dislocation configuration associated with the cell wall and that of the elastic crack with anticrack dislocations, represented as edge dislocations for convenience, is shown in Fig. 4(b). The attractive force between the dislocations of opposite signs tends to move the lattice dislocations towards the elastic crack and thus to annihilate with the anticrack dislocations. As a result, a ledge step is produced on the surface which in turn removes the misorientation that is initially introduced because of the presence of the dislocations in the cell walls. Therefore, nucleation of a microcrack and further annihilation of dislocations within the cell wall give rise to formation of a microcrack with free surfaces and reduction in strain energy associated with the misorientation. The total energy change may be written in the simple form

$$\Delta E = E_{e_2} - E_{e_1} + E_{\gamma_2} + E_f + E_w \quad (3)$$

where  $E_{e_1}$  is the strain energy associated with the cell wall initially before the nucleation of the elastic crack,  $E_{e_2}$  is the elastic strain energy of the total configuration after partial dislocation annihilation,  $E_{\gamma_2}$  is the free surface energy associated with the crack surfaces,  $E_f$  is the frictional energy spent in the movement of lattice dislocations and  $E_w$  is the work done by the applied stress. If complete annihilation of the dislocations in the cell walls takes place,  $E_{e_2} = 0$ . The term  $E_{e_1}$  in eqn. (3) is the energy associated with the boundaries of the cell walls. Further, the above equation suggests that, if the frictional stress is small, the strain energy associated with the cell walls can be sufficiently larger than the surface energy before a crack nucleates that there is a net energy decrease. Therefore, a critical misorientation across the cell walls is needed above which nucleation of microcracks along cell walls becomes thermodynamically favorable.

At this point, it is useful to note that the cell wall has a boundary separating the dislocation-free area from that within which dislocations are present. Across this interface,

there is no material discontinuity other than the orientation difference. Therefore the energy  $E_e$  associated with the interface is only due to the misorientation and is given by the strain energy of the dislocations. When the foil area adjacent to the elastic crack becomes free from any defects, the dislocations originating from adjacent cell walls and the crack tip move into the free area of the foil and this will give rise to further thinning and relaxation of the stress field associated with cell walls.

### 5. NUCLEATION AND PROPAGATION OF CRACKS UNDER NORMAL RATES OF DEFORMATION

In this section the formation of dislocation substructures in thicker foils in front of the crack tip will be presented to illustrate the ductile fracture behavior at normal strain rates. Figure 5 shows the electron microscopy observations of a region in an Nb-10 at.% V foil ahead of the crack tip. The operation of several slip systems which generate dislocations with multiple Burgers vectors and further rearrangement in the form of the cell struc-



Fig. 5. Thinning in front of crack tip in Nb-10 at.% V foil (transmission electron microscopy *in situ* straining). Dislocation cells are in evidence in thinned and thicker regions.

ture is an important feature of the micrograph. The gradual thinning of the region ahead of the crack tip made the foil electron transparent to the beam. Simultaneously, the cell structure becomes more regular, with regions in between the cell walls now becoming free from dislocations. A comparison of the dislocation substructure in the thicker areas of the foil adjacent to the crack flanks with those observed in the thinned areas illustrates the rearrangement of dislocations into a more regular arrangement of cell walls with lower energy. The dense dislocation substructure within cell walls, separating the areas free from dislocations, can be recognized only within the thinned and more transparent area ahead of the crack tip.

The gradual thinning of the foil ahead of the tip requires the operation of several slip systems, with a minimum of two systems. This will be illustrated for the thinning of gold foils during the process of ductile fracture. First, a comparison will be made between a crack tip moving at a slow rate of straining (less than  $10^{-4} \text{ s}^{-1}$ ) (Fig. 2(a)) and a crack "tip" moving during strain rates larger than  $10^{-4} \text{ s}^{-1}$  (Fig. 6). The latter consists of a series of microcracks which have edges corresponding to crystallographic directions. The spacing of the ensuing holes is approximately equal to the dislocation cell diameter and nucleation occurred at cell walls as described above. While the whole tip configuration at first seems to be similar to the Dugdale model in Fig. 7, it is clear (i) that two glide systems are needed to effect the growth of each microcrack and (ii) that an additional system of translation is required in order to link the microcracks together. It was found [22] that four equally stressed glide systems of maximum resolved shear stress, namely  $(111)[10\bar{1}]$ ,  $(111)[01\bar{1}]$ ,  $(\bar{1}\bar{1}1)[101]$  and  $(\bar{1}\bar{1}1)[011]$ , operated to enlarge each individual microcrack, thereby thinning the foil parallel to  $[\bar{1}10]$  as shown for a foil orientation of  $(110)$  in Fig. 8.

The stress field associated with the major crack exhibits a singularity ahead of the tip in the presence of a plastic zone [6]. The energy changes at the nucleation of a microcrack in the form of a slit ahead of the major crack have been determined and are presented in Table 1. A schematic illustration of the mechanism of nucleation of a microcrack is



Fig. 6. Crack tip consisting of numerous microcracks in gold foil produced by *in situ* straining in a transmission electron microscope at  $\dot{\epsilon} \approx 10^{-3} \text{ s}^{-1}$ . The edges are parallel to  $\langle 110 \rangle$  and  $\langle 112 \rangle$ .

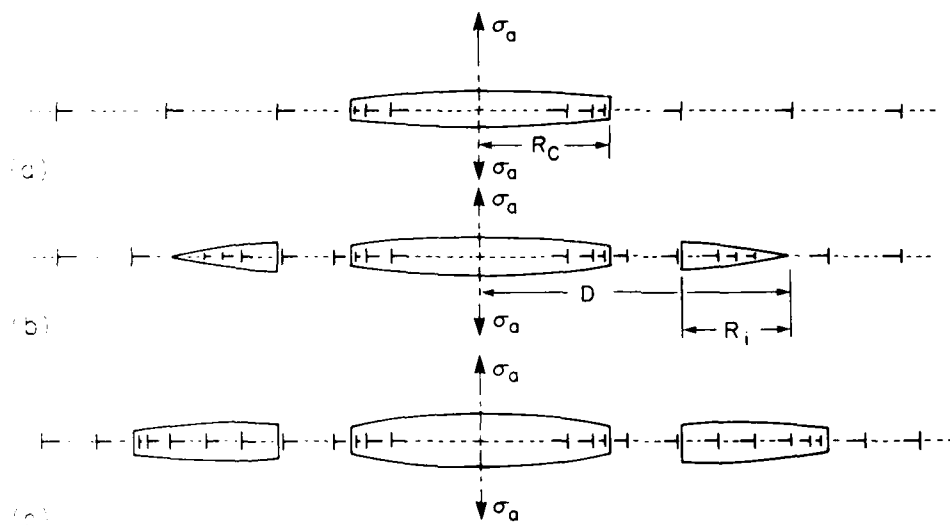


Fig. 7. (a) Dugdale's representation of a plastic tensile crack. The crack region is represented by crack dislocations and the plastic zone by lattice dislocations. (b) A void is nucleated at the position of the second lattice dislocation. The void tip is sharp at the opposite end. (c) Void growth by emitting lattice dislocations at the tip.

shown in Fig. 7, including the definition of some of the parameters presented in Table 1. In addition, the various energy terms contributing to the total energy of the configuration and the constitutive energy equations connecting the various energy terms are listed in Table 1, while the details of the analysis can be obtained from ref. 23.

The total energy of the crack-void configuration given by  $E_T$  in Table 1, last column, shows the decrease in energy associated with the nucleation of the void or microcrack. The important parameters that determine the successful nucleation of a microcrack are the

yield stress or the frictional stress in the lattice, the initial distance between the void and the crack, and the crack size. It is clear from Table 1 that a higher lattice frictional stress resulting in higher frictional energy is not favorable for crack nucleation. Similarly, if the frictional stress is very low, plastic deformation becomes very extensive so that nucleation in the form of a slit is again not favored. Instead, nucleation of a void along a cell wall should be more favorable energetically, as described earlier [15].

The development of crystallographic holes ahead of the crack tip at high strain rates of

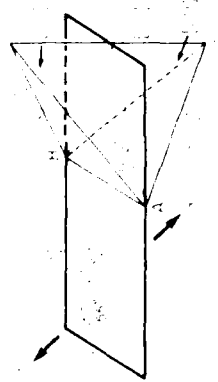


Fig. 8. Geometry of active slip planes for gold foil strained approximately parallel to [111]. The plane of foil is (110).

TABLE I

Energy contributions to the total energy of the crack-void configuration for  $\sigma_a = 300.0 \times 10^8 \text{ dyn cm}^{-2}$ ,  $R_c = 1200 \text{ \AA}$  and two values of  $\sigma_y$

$\sigma_y$ ( $\times 10^8$ dyn $\text{cm}^{-2}$ )	$D$ ( $\text{\AA}$ )	$R_1$ ( $\text{\AA}$ )	$b_{Lc}$ ( $\text{\AA}$ )	$b_{L1}$ ( $\text{\AA}$ )	$E_{e1}$ ( $\times 10^{-2}$ erg $\text{cm}^{-1}$ )	$E_{wc}/2$ ( $\times 10^{-2}$ erg $\text{cm}^{-1}$ )	$E_{e2}$ ( $\times 10^{-2}$ erg $\text{cm}^{-1}$ )	$(E_{w1} - E_{L1}^p)/2$ ( $\times 10^{-2}$ erg $\text{cm}^{-1}$ )	$E_{e1}$ ( $\times 10^{-2}$ erg $\text{cm}^{-1}$ )	$(E_{w1} - E_{L1}^p)/2$ ( $\times 10^{-2}$ erg $\text{cm}^{-1}$ )	$E_{L1}$ ( $\times 10^{-2}$ erg $\text{cm}^{-1}$ )	$E_{\gamma}$ ( $\times 10^{-2}$ erg $\text{cm}^{-1}$ )	$E_T$ ( $\times 10^{-2}$ erg $\text{cm}^{-1}$ )
400.0	—	—	31.43	—	11.83	11.56	—	—	10.07	9.80	0.12	—	-21.23
400.0	1408.5	30.0	40.32	9.30	9.85	9.64	3.22	3.24	10.12	9.84	0.19	0.23	-21.81
400.0	1418.5	40.0	41.33	10.45	9.70	9.50	3.64	3.67	10.10	9.85	0.20	0.31	-21.86
400.0	1428.5	50.0	42.26	11.03	9.60	9.40	3.81	3.90	10.27	9.97	0.21	0.39	-21.85
600.0	—	—	10.43	—	5.45	5.32	—	—	2.22	2.21	0.04	—	-7.48
600.0	1251.3	20.0	15.39	5.42	4.48	4.38	1.23	1.25	2.13	2.18	0.08	0.16	-7.44
600.0	1261.3	30.0	16.78	6.42	4.27	4.18	1.47	1.49	2.24	2.29	0.09	0.23	-7.44
600.0	1271.3	40.0	17.87	7.32	4.12	4.03	1.69	1.71	2.29	2.35	0.10	0.31	-7.41

The energy contributions to the total energy of the crack-void configuration shown in Fig. 7 are given in this table. In addition to the parameters defined in Fig. 7,  $\sigma_y$  represents the yield stress,  $b_{Lc}$  the ledge step associated with the crack and  $b_{L1}$  the ledge step associated with the void.  $E_{e1}$  corresponds to the self-energy and interaction energy terms associated with the crack,  $E_{e2}$  to the self-energy and interaction energy terms associated with the void and  $E_{e3}$  to the self-energy and interaction energy terms associated with the plastic zone.  $E_{wc}$  is the work done by the applied stress on the crack dislocations and  $E_{wL}$  the work done by the applied stress on the lattice dislocations.  $E_{L1}$  is the frictional energy spent on the lattice dislocations in the plastic zone,  $E_{L1}^p$  the frictional energy spent in creating the ledge step at the void and  $E_{L1}^c$  the frictional energy spent in moving the lattice dislocations through the void region prior to void nucleation.  $E_{L1}$  is the surface energy associated with the ledge and  $E_{\gamma}$  the surface energy associated with the crack and void.  $E_T$  is the total energy of the crack-void configuration. A detailed description of the energy terms and the constitutive equations is given in ref. 23.

deformation needs further consideration. The initial slit formation along  $[\bar{1}10]$  by additional slip on  $(\bar{1}1\bar{1})[10\bar{1}]$  and  $(\bar{1}1\bar{1})[011]$  systems gives rise to the crystallographic edges. These zigzag patterns of cracks compare very well with those observed in bulk specimens deformed in tensile machines at normal strain rates [22]. A schematic illustration of the plastic deformation by slip responsible for the crystallographic edges parallel to  $\langle 112 \rangle$  is presented in Fig. 9(a), clarifying a few very important features of deformation. The final step in the growth of the actual crack takes place by repetitive operation of glide in a narrow slip zone as illustrated schematically in Fig. 9(a) and observed experimentally as shown in Fig. 9(b). High strain rates of defor-

mation on a limited number of slip systems and a high critical strain (greater than 5 for gold) can only be accommodated by the movement of avalanches of substantial numbers of dislocations. The frictional energy spent in the movement of large numbers of dislocations is dissipated in the form of heat. During adiabatic or near-adiabatic glide, a temperature rise in the very narrow glide zone will take place which offsets work-hardening effects. An increase in the temperature of the glide plane accompanied by softening is responsible for continuation of slip on the same slip plane.

An estimate of the critical strain for work softening, using power law hardening with an exponent  $n$  of about 0.4 [24, 25], has shown

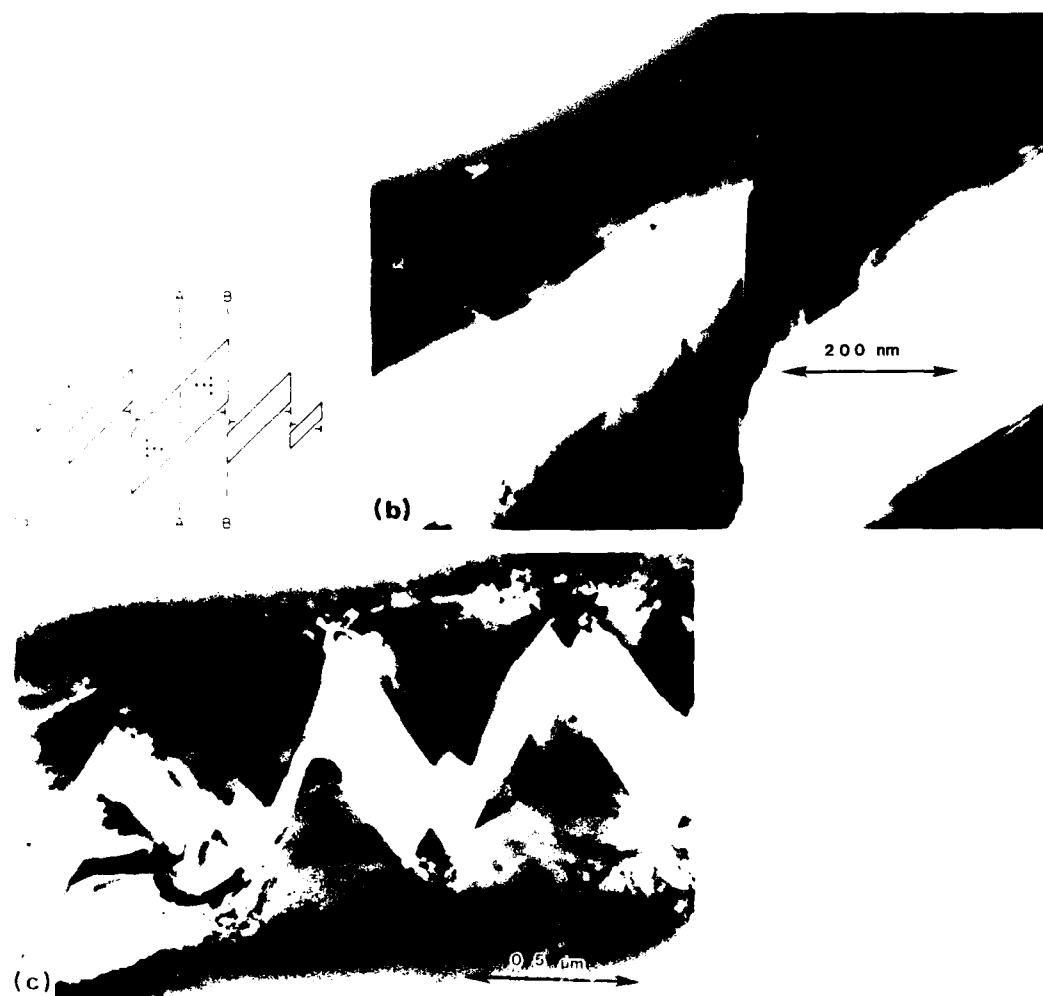


Fig. 9. Coalescence of crystallographic holes by shear along a very narrow zone: (a) schematic representation; (b) shear along narrow glide zones in a gold foil ( $\dot{\epsilon} \approx 10^{-3} \text{ s}^{-1}$ ); (c) zigzag crack produced by *in situ* straining in an Nb-10at%V foil. (a) By courtesy of M. J. Marcinkowski.)

that it should be greater than 4.4 with  $d\tau/dT = 0.2 \text{ MPa K}^{-1}$ . Similar crack growth behavior exhibiting zigzag crystallographic edges has also been observed in b.c.c. metals and alloys. Figure 9(c) shows as an example an Nb-10 at.% V alloy foil deformed *in situ* in a tensile stage. The crack flanks which were thinned during the crack propagation have been examined for the dislocation substructure retained in the foil. Extensive tilting of the foil has shown the absence of any dislocation substructure in the crack flanks. Therefore, it is concluded that the foil is sufficiently thin that it cannot retain dislocations. Only very few segments of the sources responsible for continuation of slip on the crystallographic planes and those left in the foil after extensive thinning can be observed. These are lined up parallel to the crystallographic edges of the crack. In contrast, a dense dislocation substructure consisting of a well-developed cell structure similar to that shown in Fig. 5 has been observed in the thicker areas of the foil adjacent to the crack flanks. Thus it is concluded that, simultaneously with the zigzag crack propagation, extensive thinning of the foil due to slip on several slip systems takes place, even while avalanches of dislocations on a few crystallographic planes, which result in adiabatic or thermoplastic slip and glide instability, are responsible for crystallographic edges and zigzag crack propagation [24].

As we have seen so far, there are two instabilities associated with a crack tip: the first results from the initiation of microcracks at dislocation cell walls, and the second completes local crack propagation by adiabatic shear. In addition, thermal instability occurs during the thinning of microligaments. This can be deduced from the presence of stacking fault tetrahedra found in ligaments of gold and copper [22] as shown in Fig. 10(a) for gold. Figure 10(b) permits accurate measurements to be made, leading to the calculation of a vacancy density  $C_v$  in gold of  $4 \times 10^{-4}$  [26]. The vacancies produced during plastic deformation do not form stacking fault tetrahedra spontaneously but need thermal activation to do so. A minimum temperature of 40 °C was estimated for the nucleation of stacking fault tetrahedra in gold [26]. Although this thermal instability is of minor importance in gold and copper, it may be-

come significant in ductile materials with a low thermal conductivity.

## 6. CRACK PROPAGATION UNDER LOW STRAIN RATES

Above, *in situ* deformation of foils at strain rates comparable with those observed in macroscopic specimens and the resulting dislocation substructures observed at the crack tip have been discussed. This section is devoted to observations at the other extreme of strain rates, namely foils deformed at very slow strain rates [1]. Under these conditions, glide dislocations do not move in large numbers all at the same time but rather singly so that each dislocation comes to rest in or near an equilibrium position. As a result, thermal instability and softening of the glide planes are not expected. Instead, work hardening due to the development of dense dislocation substructures continues on numerous slip planes. The dissipation of frictional energy causing a rise in temperature is here not large enough to reduce work hardening. As a result of increasing work hardening through deformation on specific slip planes, the operation of secondary sources with different Burgers vectors begins so that plastic deformation can continue. The final outcome is a more uniform and homogeneous deformation by the generation and movement of dislocations with several different Burgers vectors, as indeed has been observed experimentally [1].

Dislocation rearrangements to lower the energy of the configuration naturally gives rise to low energy cell walls. In comparison with the cell structure observed under normal strain rates, the cell walls formed at lower strain rates are thinner and more regular. This regular arrangement of the dislocations in the cell walls, betokening low energy configurations, is clearly seen in Fig. 11. In addition, since a repetitive operation of glide on a few slip planes is here replaced by a more uniform deformation, the crack tip becomes blunted and thus a more rounded tip is observed. At the same time, thinning of the foil continues such that the crack is linked to the nearby holes or voids. While nucleation of microcracks is still favored along the cell walls, their growth cannot be confined any longer to specific crystallographic planes. Instead, a more irregular growth of microcracks due to

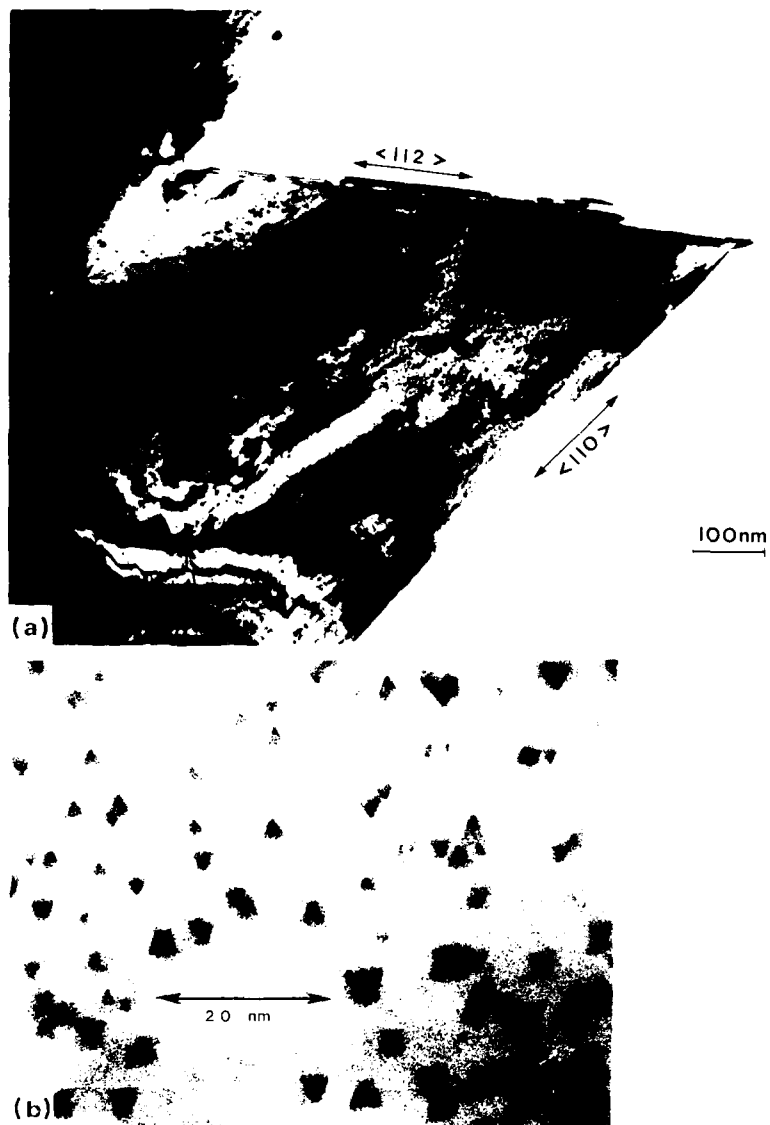


Fig. 10. Stacking fault tetrahedra in a ligament remnant of gold (a) after *in situ* straining; (b) the size of the stacking fault tetrahedra is between 1.5 and 4 nm.

deformation along several slip planes is observed. Substantial rearrangement of dislocations at low strain rates results in thinning of the foil to link the grown microcracks together. These features observed in a foil of gold deformed at very low strain rates are illustrated in Fig. 12.

#### CRACKS NUCLEATED AT INTERSECTIONS OF SLIP BANDS

As mentioned earlier, there are several parameters that influence the development

of dislocation substructure and the microstructural changes in ductile materials. Of these, the low stacking fault energy in f.c.c. and h.c.p. metals and alloys is an important parameter that restricts the mobility of dislocations. As a result, plastic deformation is by slip in the planar mode. The limited mobility of dislocations bound by stacking faults confines their movement along the slip planes, instead of developing first tangles and later on cell structures.

This type of plastic deformation is characteristic of  $\alpha$ -brass and austenitic stainless steel. It is illustrated for type 304 stainless steel in



Fig. 11. Straining at  $\dot{\epsilon} \approx 10^{-4} \text{ s}^{-1}$  leads to extensive blunting at the crack tip: (a) microcrack formation; (b) blunted crack tip. The increase in low energy dislocation walls between strain increments should be noted.

the electron micrograph shown in Fig. 13(a) [27]. A schematic illustration of the continuous thinning of the foil due to plastic deformation confined to two intersecting narrow glide bands is shown in Fig. 13(b). When thinning occurs along each band, a void is nucleated at the intersection of the bands as a result of the superposition of deformation associated with both bands. Thus, several voids nucleated along the foils at points of intersection of slip bands grow as a result of

further deformation. The growth of the voids continues only in the direction of the thinning of the foil, as illustrated in Fig. 12(a). This mechanism of void formation and growth is similar but different from that of voids when incompatibility of plastic deformation and a triaxial state of stress exist ahead of a crack tip in a work-hardened ductile material [28]. In the present situation the inhomogeneity of plastic deformation is responsible for the void nucleation and growth.



Fig. 12. Development of round holes at a crack tip during the straining of gold at  $\dot{\epsilon} < 10^{-4} \text{ s}^{-1}$ .

#### 8. DISCUSSION

It is clear from the results presented in the preceding sections that the ductile fracture behavior of metals and alloys critically depends on several experimental and materials parameters. Common to all the above descriptions of crack growth is the importance of the dislocation configurations in the process zone. In particular, low energy dislocation configurations of cell structures are a striking, and perhaps initially unexpected, microscopic observation. Provided that the dislocations in the region ahead of the crack tip are mobile, rearrangement into cell walls evidently takes place efficiently. This is accounted for by the principle of minimization of strain energy associated with the dislocation configurations [4] and may be ascribed to the energy changes associated with the dislocation rearrangements [3], namely

$$\Delta E = E_{e_2} - E_{e_1} + E_f + E_w \quad (4)$$

where  $E_{e_2}$  is the strain energy of the final cell structure configuration,  $E_{e_1}$  the strain energy of the initial configuration,  $E_f$  the frictional energy change associated with the dislocation rearrangement and  $E_w$  the work done by the applied stress. First of all, it is important to note that the term due to the applied stress is always negative while the term due to the lattice frictional stress is always positive.

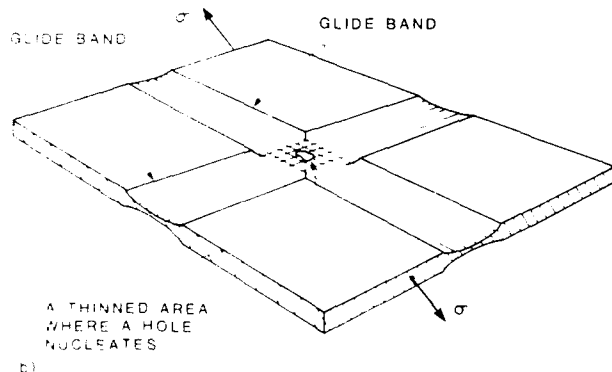
Therefore, whether dislocation rearrangement takes place or not depends largely on the frictional stress. If the frictional stress is too high, such as in the deformation of certain b.c.c. metals at low temperatures, dislocation rearrangement cannot be expected. Similarly, in f.c.c. or h.c.p. metals and alloys with a very low stacking fault energy the mobility of dislocations is very low and cell structures cannot form at moderate dislocation densities.

On the assumption that the frictional stress is very low and  $E_f$  is a negligible term, the decrease in energy of the formation of the final configuration depends on  $E_{e_2}$ . The minimization of the strain energy  $E_{e_2}$  in terms of the cell size [3], together with eqn. (1), directly leads to the simple result given in eqn. (2), with the constant  $K$  of the order of 10.

These results, which are valid for a uniform applied stress, should now be applied to the region in front of the crack tip. A schematic illustration of the cell structure envisaged in the region ahead of the crack tip is shown in Fig. 14. It is important to distinguish the dislocation substructure formed in front of a crack tip in a virgin crystal from that present in a crystal wherein a crack is nucleated after considerable plastic deformation. In the former situation the dislocation configuration is formed in the presence of both the applied stress and the crack tip stress field, and the latter corresponds to the prior



(a)



(b)

Fig. 13. (a) Hole formation at intersection of crossing glide bands in a type 304 stainless steel foil  $0.6 \mu\text{m}$  thick after *in situ* straining in the high voltage electron microscope; (b) schematic drawing depicting hole formation as shown by (a). ((a) By courtesy of Bauer [27].)

development of a stable cell structure before the crack is nucleated. Therefore, growth of the crack into a region where there is micro-crack nucleation along cell walls may be distinguished from a region where gradual thinning of the foil with a more regular cell wall arrangement occurs. Actually, further subdivision of a pre-existing cell structure is also observed in the crack tip stress field. This can reduce cell diameters to one-tenth or less of those which are a long distance from the tip.

Measurements of cell diameters in front of the crack tip in Figs. 3(a) and 3(b) for beryllium, in Fig. 5 for Nb 10 at.% V and in Figs. 11(a), 11(b) and 12 for gold correspond to an average value of 60–100 nm. Using this value

of  $L$  in eqn. (2), the shear stress  $\tau$  in the Nb-10 at.% V foil is determined to be  $1.56 \times 10^6$  Pa or  $E/90$  where  $E$  is Young's modulus. The same order of magnitude of shear stress was also found in other foils examined and it is considered to be a reasonable value. Here the frictional stress  $\tau_0$  was neglected in comparison with the resolved shear stress  $\tau$  in the foil. It should be noted that these results are applicable in foils with prior deformation so that a well-developed cell structure pre-exists ahead of the crack tip.

When a crack is formed in a well-annealed crystal, the resulting dislocation configuration must correspond to the crack tip stress field over a wide area. In particular, we consider

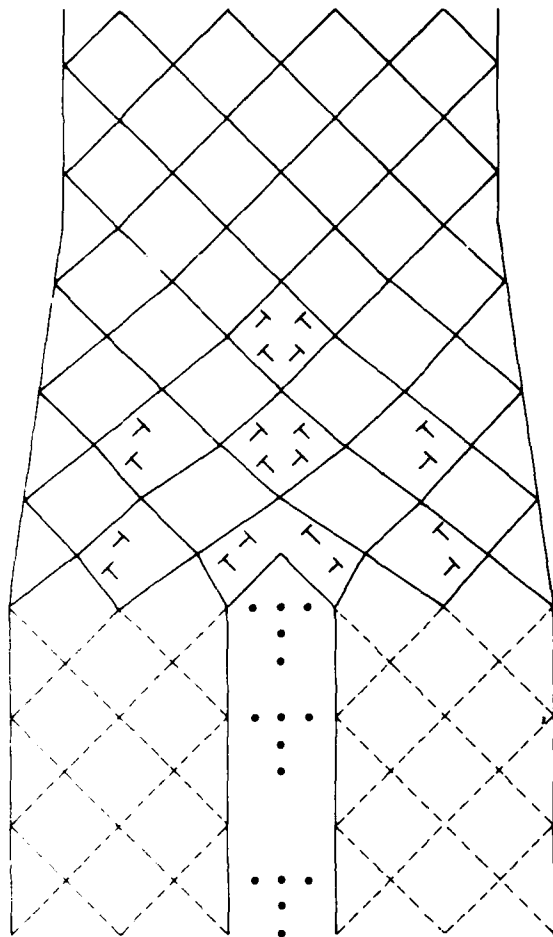


Fig. 14. Model of a crack tip surrounded by dislocation cells. (By courtesy of M. J. Marcinkowski.)

the plane strain situation of an elastic crack in mode I present in a thick foil. The shear stress component responsible for the generation and movement of dislocations is given by

$$\sigma_{xy}(r, \theta) = \sigma_a \left( \frac{R}{2r} \right)^{1/2} \sin \theta \sin \frac{3}{2} \theta \quad (5)$$

where  $(r, \theta)$  coordinates are employed [4]. The shear stress component due to the crack is superimposed on the component due to the applied stress. Thus, in addition to the dislocation density  $\rho_{\text{appl}}$  due to the applied stress, the dislocation density  $\rho_{\text{crack}}$  due to the crack tip stress field should be determined and superimposed to obtain the total dislocation density

$$\rho_{\text{total}} = \rho_{\text{crack}} + \rho_{\text{appl}} \quad (6)$$

Implicit in eqn. (6) is the assumption that the two dislocation density terms can be superimposed. The resultant flow stress may be given in the form

$$\tau_{\text{appl}} - \tau_0 = \frac{Gb}{6\pi} \rho_{\text{appl}}^{1/2} \ln \left( \frac{3}{b\rho_{\text{appl}}^{1/2}} \right) \quad (7)$$

and

$$\begin{aligned} \sigma_a \frac{R}{2r} \sin \theta \sin \frac{3}{2} \theta - \tau_0 \\ = \frac{Gb}{6} \rho_{\text{crack}} \ln \left\{ \left( \frac{3}{b\rho_{\text{crack}}} \right) \right\} \end{aligned} \quad (8)$$

The arrangement of lattice dislocations in the form of a low energy configuration such as a cell structure, a Taylor lattice, a dipolar mat, a tilt wall or a dislocation boundary [10] is to be expected in the spatially varying stress field. Using eqn. (2) in conjunction with eqns. (7) and (8), the cell size theoretically expected at the crack tip can be calculated. It is found that the resolved shear stress component due to the crack tip when calculated for different applied stress levels [4] remains almost constant over a limited length along certain orientations of slip planes. Thus a cell structure of uniform size along these planes of constant shear stress results. A one-to-one correspondence between the magnitude of shear stress and the low energy cell structure is observed [29].

In the fracture of ductile materials, crack nucleation and propagation into a region containing stable cell structures are the most common case. The cell structure screens the stress field associated with the crack. In addition, the crack tip in ductile materials is not sharp because of the formation of ledges through multiple slip at the tip. As a result, the actual stress field does not exhibit a strong singularity. Therefore, crack growth necessarily progresses via microstructural changes ahead of the tip, such as foil thinning and the microcrack nucleation described earlier. The coalescence of microcracks or voids leads to growth of the crack in the macroscopic sense.

When the crack encounters the stable cell structure, the stress associated with the tip generates additional dislocations from sources present in the cell walls. This is clearly illustrated in Fig. 15 by the nucleation of disloca-



Fig. 15. Nucleation of numerous dislocations from links in cell walls during straining of an Nb-10at.%V foil in the transmission electron microscope, thereby continuing the thinning process at the crack tip. The direction of dislocation motion is indicated by the arrow.



Fig. 16. Ligament remnants in a fractured Nb-10at.%V foil. It should be noted that cells are absent in the areas of the crack flank; incomplete cells are visible at the upper crack flank near the non-transparent foil.

tions in the thin area of a propagating crack tip in an Nb-10at.%V foil. Thus, in bulk samples, the increase in dislocation density as a crack advances into a stable cell structure occurs by the activation of sources from free dislocation link lengths within the cell walls. In contrast, in foil samples, plastic deforma-

tion ahead of the tip leading to thinning of the foil such that the foil is free from any dislocation substructure as shown in Fig. 16 is very important. When the foil is free from dislocations, it may become brittle and final separation can take place. The same process can presumably also occur in the bulk. There-

fore, in the fracture of ductile materials the nature of the microstructural features formed ahead of the crack tip is very important as already repeatedly emphasized.

Restrictions on the mobility of dislocations, such as through the presence of stacking fault ribbons between partials in extended dislocations, have a significant influence on the development of substructural features. This has already been demonstrated by the example of the confinement of sequences of gliding dislocations into narrow slip zones in low stacking fault energy alloys and the resulting nucleation of voids due to foil thinning at points of intersection of slip bands as discussed in Section 7. Conversely, the mobility of dislocations can be increased by raising the temperature of deformation. Then, both conservative and non-conservative motion of dislocations becomes relatively easier so that polygonization and low energy dislocation cell structures can develop.

In this connection the importance of strain rate cannot be overemphasized. Already, thermal instabilities giving rise to crystallographic microcrack growth and coalescence have been documented in Section 6 for high strain rates. However, irregular microcrack configurations are a natural consequence of low strain rates. The above concept of the importance of local temperature increases due to straining has been tested in recent high strain rate experiments on macroscopic specimens in two titanium alloys [30]. These have confirmed that the heat evolution at the tip of a moving crack can indeed give rise to large temperature increases in these alloys. In fact, a considerable number of dimples have been found to consist of solidified regions from molten crack ligaments, constituting irrefutable proof of the occurrence of thermal instabilities as discussed above.

## 9. SUMMARY AND CONCLUSIONS

The ductile fracture behavior of metals and alloys inferred from *in situ* experiments in the transmission electron microscope has been reviewed. Direct observations of dislocation substructures developed during *in situ* fracture of foils of ductile materials have been presented. The influence of several parameters

(including some associated with the experimental conditions and others dictated by the nature of the metal or alloy) on the formation of microstructural features ahead of the crack tip have been clarified. Whereas some differences in the observations can be ascribed to the nature of the metal or alloy, a common feature is that all the dislocation configurations discussed exhibit evidence for the operation of the principle of energy minimization. Specifically, provided that the mobility of the dislocations is fairly high and more than one Burgers vector is represented, low energy cell structures form.

Microstructural features, such as crystallographic microcracks, foil thinning due to multiple slip, microcrack nucleation along cell walls in thick foils, and irregular microcracks due to the formation of thinner cell walls during very slow straining, have all been illustrated to emphasize the conditions of crack formation and their effect on the growth of cracks. In this, the influence of restricted mobility of dislocations on the confinement of slip to narrow slip zones and the resultant thinning to form voids or microcracks has been clarified. Also, the occasional gradual thinning of the foil such that no dislocations are present when it becomes very thin, together with the resulting brittle behavior, has been noted.

Two types of crack growth behavior were discussed, namely the crack growth into a region free from any dislocation substructure and the movement of a crack into a region with a well-developed stable cell structure. In this connection the importance of work hardening in the ductile fracture behavior of metals and alloys has been emphasized. The superposition of two dislocation density terms, namely the dislocation density due to the applied stress and the dislocation density due to the crack tip stress field, has been inferred. Most notably, and contrary to intuition, it has been found that there should not be a continuously spatially varying cell size in the region of the crack tip, since the theoretically deduced resolved shear stress component, which is responsible for the movement of the most prevalent dislocations, is constant over a length of specific planes. Thus, it is therefore proposed (and appears to be confirmed in Fig. 5, for example) that a uniform cell size will form along the planes

of those orientations in the region of constant shear stress.

*In situ* fracture experiments are useful for understanding macroscopic ductile fracture provided that a proper choice of experimental parameters is made. The direct observation of microstructural features in the transmission electron microscope to gain a better understanding of ductile fracture is an invaluable advantage associated with *in situ* fracture experiments. This is so, especially since changes in dislocation substructures in the region ahead of the crack tip, in the plastic zone, lead to microstructural features which turn out to be of utmost importance for the understanding of ductile fracture in general.

#### ACKNOWLEDGMENTS

We thank Professor M. John Marcinkowski for valuable contributions and Professor Doris Kuhlmann-Wilsdorf for numerous discussions in the course of preparing this paper.

One of the authors (K.J.) acknowledges the support of the Division of Materials Science, Office of Basic Energy Sciences, U.S. Department of Energy, under Contract W-7405-Eng.-82. H.G.F.W. appreciates the support of the Office of Naval Research, Metals and Alloy Program, under Contract N00014-82-K-0309.

#### REFERENCES

- 1 H. G. F. Wilsdorf, *Mater. Sci. Eng.*, **59** (1983) 1.
- 2 J. D. Eshelby, in M. r. Kanninen, W. A. Adler, A. R. Rosenfield and R. A. Jaffee (eds.), *Inelastic Behavior of Solids*, McGraw-Hill, New York, 1969, p. 77.
- 3 D. Kuhlmann-Wilsdorf and J. H. van der Merwe, *Mater. Sci. Eng.*, **55** (1982) 79.
- 4 K. Jagannadham and M. J. Marcinkowski, *Unified Theory of Fracture*, Trans Tech Publications, Aedermannsdorf, 1983.
- 5 H. Liebowitz (ed.), *Fracture, An Advanced Treatise*, Vol. 2, Academic Press, New York, 1968, pp. 429, 583.
- 6 J. R. Rice, in H. Liebowitz (ed.), *Fracture, an Advanced Treatise*, Vol. 2, Academic Press, New York, 1968, Chapter 3.
- 7 R. W. Armstrong, *Mater. Sci. Eng.*, **1** (1966) 251.
- 8 J. R. Rice and R. Thompson, *Philos. Mag.*, **29** (1974) 73.
- 9 R. W. Bauer, R. L. Lyles and H. G. F. Wilsdorf, *Z. Metallkd.*, **63** (1972) 525.
- 10 N. Hansen and D. Kuhlmann-Wilsdorf, *Mater. Sci. Eng.*, **81** (1986) 141.
- 11 J. P. Hirth and J. Lothe, *Theory of Dislocations*, McGraw-Hill, New York, 1968.
- 12 J. A. Horton, S. M. Ohr and W. A. Jesser, *J. Nucl. Mater.*, **103** (1981) 865.
- 13 I. Y. Chan and H. G. F. Wilsdorf, *Acta Metall.*, **29** (1981) 1221.
- 14 A. R. Rosenfield, *Metall. Rev.*, **13** (1968) 29.
- 15 R. N. Gardner, T. C. Pollock and H. G. F. Wilsdorf, *Mater. Sci. Eng.*, **29** (1977) 169.
- 16 D. Kuhlmann-Wilsdorf, in J. P. Hirth and J. Weertman (eds.), *Work Hardening, Gordon and Breach*, New York, 1968, p. 97.
- 17 T. C. Pollock and H. G. F. Wilsdorf, *Mater. Sci. Eng.*, **61** (1983) 7.
- 18 K. Sadanada, K. Jagannadham and M. J. Marcinkowski, *Phys. Status Solidi A*, **44** (1977) 633.
- 19 K. Jagannadham and F. C. Laabs, to be published
- 20 E. Orowan, in *Fracture, Proc. Int. Conf. on the Atomic Mechanisms of Fracture, Swampscott, MA, 1959*, Wiley, New York, 1959, pp. 1-4.
- 21 T. C. Pollock, *Ph.D. Dissertation*, University of Virginia, Charlottesville, VA, 1977.
- 22 H. G. F. Wilsdorf, *Acta Metall.*, **30** (1982) 1247.
- 23 K. Jagannadham, *Mater. Sci. Eng.*, **60** (1983) 95.
- 24 H. G. F. Wilsdorf, *Z. Metallkd.*, **75** (1984) 154.
- 25 R. S. Culver, in R. W. Ronde, B. M. Butcher, J. R. Holland and C. H. Carnes (eds.), *Metalurgical Effects at High Strain Rates*, Plenum, New York, 1973, p. 519.
- 26 H. G. F. Wilsdorf, *Scr. Metall.*, **17** (1983) 1209.
- 27 R. W. Bauer, *Ph.D. Dissertation*, University of Virginia, Charlottesville, VA, 1975.
- 28 J. R. Rice and G. F. Rosengren, *J. Mech. Phys. Solids*, **16** (1968) 1.
- 29 K. Jagannadham, J. Narayan and H. G. F. Wilsdorf, in F. H. Wohlbiel (ed.), *Materials Science Reviews*, Trans Tech Publications, Aedermannsdorf, 1986.
- 30 J. D. Bryant, D. D. Makel and H. G. F. Wilsdorf, *Mater. Sci. Eng.*, **77** (1986) 85.

## PRESENTATIONS

Under ONR Contract #N00014-82-K-0309 by the Principal Investigator with graduate students and colleagues

1. Crack Initiation and Growth in Ductile Fracture. Dept. of Mechanics and Materials Science, Rutgers University, New Jersey (March 18, 1982).
2. Fracture of a Ti-8Mn Alloy, Virginia Academy of Science, Annual Meeting; with J. I. Bennetch (April 22, 1982).
3. Ductile Fracture - A Microstructural Viewpoint, Materials Science Alumni Conference, University of Virginia (August 14, 1982).
4. Rupture Processes in Ductile Fracture, 1983 TMS-AIME Annual Meeting, Atlanta, GA (March 9, 1983).
5. Crystal Defect Behavior During Heavy Deformation Leading to Rupture, American Physical Society, Los Angeles, CA (March 23, 1983).
6. Investigations of Crack Tips by HVEM and TEM, Colloquium, Inst. f. Metallphysik, Univ. Gottingen, Germany (May 13, 1983).
7. A Microstructural Study of Ductile Fracture of an Aluminum-Copper Alloy, Virginia Academy of Science, George Mason University; with D. Nakel (May 19, 1983).
8. The Ductile Fracture of C.P. Titanium, Virginia Academy of Science, George Mason University; with M. Erickson (May 19, 1983).
9. Riss-Spitzen Vorgange beim Duktilbruch in Reinstmetallen, Deutsche Gesellschaft fur Metallkunde, Erlangen, Germany (May 27, 1983).
10. Shear Instabilities During Crack Propagation in Gold, Conference on Crack Tip Structure and Processes, NBS, Gaithersburg, MD (June 7, 1983).
11. Crack Tip Geometries in Pure FCC Metals (Poster), Conference on Crack Tip Structure and Processes, NBS, Gaithersburg, MD (June 6-8, 1983).
12. Flow Instabilities at Crack Tips, Fracture Seminar, Inst. f. Metallphysik, Univ. Gottingen, Germany (June 10, 1983).
13. Energy Dispersion at Crack Tips, Colloquium, Fraunhofer Inst. f. Angew. Materialforschung, Bremen-Lesum, Germany (August 8, 1983).
14. Crack Tip Geometries and Glide Configurations, Inst. f. Elektronenmikroskopie, Halle, Germany (August 16, 1983).

15. Investigation of Ductile Fracture by in-situ HVEM, Inst. f. Werkstoffkunde, Techn. Univ. of Clausthal-Zellerfeld, Germany (August 22, 1983).
16. Crack Tip Geometries in Ductile Metals, Colloquium, Department of Mechanical Engineering, The University of Manitoba, Winnipeg, Canada (November 14, 1983).
17. Instabilities at Crack Tips in Ductile Metals, Plenary Lecture, Pacific Northwest Metals and Minerals Conference, Portland, OR (May 1, 1984).
28. Conclusions from a 3-D Analysis of Fracture Surfaces. Seminar, Oregon Graduate Center, Beaverton, OR (May 2, 1984).
19. Crack Initiation in Ductile Metals and Alloys, Colloquium, Department of Metallurgy, University of British Columbia, Vancouver, Canada (May 4, 1984).
20. Subsurface Microstructure Determination Using a Metal Plate Profiling Technique, Annual Meeting, Virginia Academy of Science, Richmond; with D. Makel (May 17, 1984).
21. Orientation Determination of Planar Regions in the Fracture Surface of Ti-10V-2Fe-3Al, Annual Meeting, Virginia Academy of Science, Richmond; with D. Bryant (May 17, 1984).
22. Fracture in Titanium, Second Navy Fracture Mechanics Workshop, Laurel, MD (May 23, 1984).
23. HVEM In-Situ Straining to Fracture, AIME-TMS Fall Meeting, Detroit, MI (September 18, 1984).
24. Crack Tip Instabilities in Ductile Metals, American Physical Society, Baltimore, MD (March 29, 1985).
25. High Temperatures Observed at the Rupture of Micro-Ligaments in Titanium Alloys, American Physical Society, Baltimore, MD (March 29, 1985).
26. Temperature Rise at Fracture in Two Titanium Alloys, Annual Meeting, Virginia Academy of Science, Williamsburg (May 17, 1985).
27. Localized Melting at the Crack Tip in Two Titanium Alloys, Int. Conference on Metallurgical Applications of Shock-Wave and High-Strain-Rate Phenomena, Portland, OR; with D. Bryant and D. Makel (July 31, 1985).
28. Heating Effects During Fracture in Ti-10V-2Fe-3Al, TMS-AIME Annual Meeting, New Orleans, LA; with D. Bryant (March 4, 1986).
29. The Influence of Strain Rate on the Mechanism of Crack Propagation in Titanium Alloys, Annual Meeting of the Deutsche Gesellschaft für Metallkunde, Göttingen, West Germany (May 21, 1986).

30. Effects of Temperature on the Fracture of Titanium Alloys, Fraunhofer-Institut für angewandte Materialforschung, Bremen-Lesum, West Germany (May 26, 1986).
31. Low-Energy Dislocation Structures Associated with Fracture, International Conference on Low-Energy Dislocation Structures, University of Virginia, Charlottesville, VA; with K. Jagannadham (August 12, 1986).
32. An Assessment of the Temperature Rise at the Crack Tip in Titanium Alloys, Naval Surface Weapons Center, Silver Spring, MD (September 18, 1986).
33. Stereoscopic Investigations of the Surface and Subsurface Structures Formed During the Fast Fracture of Ti8Mn, 1986 TMS Fall Meeting, Orlando, FL; with D. D. Makel (October 5-9, 1986).
34. Effect of Loading Rate on the Fracture Toughness of Ti-10V-2Fe-3Al, 1986 TMS Fall Meeting, Orlando, FL; with J. D. Bryant (October 5-9, 1986).
35. An Assessment of the Temperature Rise at the Crack Tip in Titanium Alloys, North Carolina State University, Raleigh, NC (March 13, 1987).
36. Quantifying Fracture Surfaces by Stereo-photogrammetry, Sixth Pfefferkorn Conference on Image and Signal Processing, Niagara Falls, Ontario; with J. D. Bryant (April 27-May 2, 1987).
37. Investigations of Thermal Effects in Areas of High Shear Caused by Rapid Tensile Separation, IMPACT'87, Bremen, Germany; with D. D. Makel (May 18-22, 1987).
38. Effect of Increasing Loading Rate on Tensile Properties and Fracture Toughness, IMPACT'87, Bremen, West Germany; with J. D. Bryant (May 18-22, 1987).
39. The Fracture Surface as an Indicator for Strain Rate Effects, Virginia Academy of Science Annual Meeting, Norfolk, VA; with J. D. Bryant (June 19-20, 1987).
40. Development of High Temperature During Fast Fracture in Titanium Alloys, David Taylor Naval Ship Research and Development Center, Annapolis, MD (July 29, 1987).
41. Thermal-Mechanical Coupling at the Head of a Rapidly Loaded Crack Tip, TMS Fall Meeting, Cincinnati, OH; with J. D. Bryant (October 10-15, 1987).
42. Adiabatic Shear During the Final Separation of Tensile Samples, TMS Annual Meeting, Phoenix, AZ; with D. Makel (January 25, 1988).

## PUBLICATIONS

Under ONR Contract #N00014-82-K-0309 by the Principal Investigator with graduate students and colleagues

1. "The Ductile Fracture of Metals: A Microstructural Viewpoint," Materials Science and Engineering, Vol. 59 (1983), pp. 1-39.
2. "Flow Instabilities at Crack Tips in Ductile Metals," Scripta Met., Vol. 17 (1983), pp. 1209-1212.
3. "The Ductile Fracture of C.P. Titanium: A Study in the Microstructural Regime." by Marjorie A. Erickson, Master's thesis (Materials Science), University of Virginia, April 1983.
4. "Deformation Processes at Crack Tips in Ductile Metals," ZS. Metallkd., Vol. 75 (1984), pp. 154-160.
5. "Mikrostrukturelle Vorgänge an der Riss-Spitze in Kubisch flächenzentrierten Metallen und Legierungen," Nachr. Akad. Wissensch. Göttingen. II Math. Physikal. Kl. 1984, 1-12.
6. "HVEM In-Situ Straining to Fracture," Proceedings of a Symposium, Measurement of Localized Deformation Associated with Fracture Using Novel Techniques," Eds., Gerberich, W. W., and Davidson, D. L., TMS-AIME (1985), pp. 137-149.
7. "Dislocation-Free Zones at Crack Tips: Do They Exist?" Proceedings of a Symposium, "Measurement of Localized Deformation Associated with Fracture Using Novel Techniques," Eds., Gerberich, W. W., and Davidson, D. L., TMS-AIME (1985), pp. 119-123 (with Robertson, I. M., Bond, G. M., and Birnbaum, H. K.).
8. "The Effect of Primary Alpha Precipitates on Deformation in Ti-10V-2Fe-3Al," by James Daniel Bryant, Master's thesis (Materials Science), University of Virginia, January 1985.
9. "Observations on the Effect of Temperature Rise at Fracture in Two Titanium Alloys," Materials Science and Engineering, Vol. 77 (1986), pp. 85-93 (with Bryant, J. D., and Makel, D. D.).
10. "Localized Melting at the Crack Tip in Two Titanium Alloys," Proc. Int. Conf. on Metall. Appl. of Shock-Wave and High-Strain-Rate Phenomena, Eds., Murr, L. E., Staudhammer, K. P., and Meyers, M. A., Marcel Dekker, NY (1986), pp. 723-739 (with Bryant, J. D., and Makel, D.D.)
11. "Low Energy Dislocation Structures Associated with Cracks in Ductile Fracture," Materials Science and Engineering, Vol. 81 (1986), pp. 273-292 (with Jagannadham, K.).
12. "The Influence of Several Parameters at Electron Microscopic Observations of In-Situ Fracture," Crystal Properties and Preparation, Vol. 9 (1986), pp. 1-54 (with Jagannadham, K., and Narayan, J.).

13. "Semi-Automated Topographic Mapping of Fracture Surfaces Through Stereo-Photogrammetry," Micron and Microscopica Acta, Vol. 17 (1986) pp. 237-242 (Bryant, J. D.).
14. "Spatially Varying Crack Tip Stress Fields and Low Energy Dislocation Substructures," International Journal of Fracture, Vol. 34 (1987), pp. 297-307 (with Jagannadham, K.).
15. "An Investigation of Unusual Surface Features Caused by Adiabatic Shear During Tensile Separation," Scripta Met., Vol. 21 (1987), pp. 1229-1234 (with Makel, D. D.).
16. "Deformational Heating at the Crack Tip and Its Role in Fracture of Ti-10V-2Fe-3Al." by James Daniel Bryant, Doctoral thesis (Materials Science), University of Virginia, January 1987.
17. "Strain Rate Dependent Processes in the Fracture of Ti8Mn." by David D. Makel, Doctoral thesis (Materials Science), University of Virginia, August 1987.
18. "Investigations of Thermal Effects in Areas of High Shear Caused by Rapid Tensile Separation," Proceedings of IMPACT'87: International Conference on Impact Loading and Dynamic Behavior of Materials, Vol. II (1988) pp. 587-594 (with Makel, D. D.) DGM Inf. Ges. Verlag.
19. "The Effect of Increasing Loading Rate on Tensile Properties and Fracture Toughness of Ti-10V-2Fe-3Al," Proceedings of IMPACT'87: International Conference on Impact Loading and Dynamic Behavior of Materials, Vol. I (1988) pp. 145-152 (with Bryant, J. D.) DGM Inf. Ges. Verlag.
20. "Quantifying Fracture Surfaces by Stereo-Photogrammetry," Proceedings: 6th Pfefferkorn Conf. on Image and Signal Processing, SEM International, in press (with Bryant, J. D.).
21. "The Development of High Temperatures in Titanium Alloys During Fast Fracture," Proceedings of ICSMA8, in press. (with Jagannadham, K., Kunze, H.-D., and Meyer, L. W.).
22. "The Effect of Thermal-Mechanical Coupling at the Head of a Rapidly Loaded Crack Tip," by J. D. Bryant, to be submitted.
23. "A Geometrical Model of the Strain Rate Dependent Fracture of Ti-8Mn," by D. D. Makel, to be submitted.
24. "A Numerical Model for Calculating the Temperature Rise at Crack Tips in a Titanium Alloy," to be submitted (with Jagannadham, K.).

### DEGREES AWARDED

The following degrees have been awarded during this project period:

1. M. S. (Materials Science), University of Virginia, to Marjorie A. Erickson, April 1983: "The Ductile Fracture of C.P. Titanium: A Study in the Microstructural Regime."
2. M. S. (Materials Science), University of Virginia, to James Daniel Bryant, January 1985: "The Effect of Primary Alpha Precipitates on Deformation in Ti-10V-2Fe-3Al."
3. Ph.D. (Materials Science), University of Virginia, to James Daniel Bryant, January 1987: "Deformational Heating at the Crack Tip and Its Role in Fracture of Ti-10V-2Fe-3Al."
4. Ph. D. (Materials Science), University of Virginia, to David D. Makel, August 1987: "Strain Rate Dependent Processes in the Fracture of Ti8Mn."

DISTRIBUTION LIST

Copy No.

- 1 - 6      Director  
            Naval Research Laboratory  
            Washington, DC 20375  
            Attention: Code 2627
- 7            Dr. D. E. Polk  
            Program Officer  
            Materials Division  
            Code 1131  
            Office of Naval Research  
            800 N. Quincy Street  
            Washington, DC 22217-5000
- 8 - 19      Defense Technical Information Center  
            S47031  
            Building 5, Cameron Station  
            Alexandria, VA 22314
- 20 - 21     H. G. F. Wilsdorf, MS
- 22 - 23     T. H. Courtney, MS
- 24 - 25     Ms. E. H. Pancake, Clark Hall
- 26           SEAS Publication Files
- 27 - 76     Supplemental Distribution List
- \*            Office of Naval Research Resident Representative  
            818 Connecticut Avenue, N. W.  
            Eighth Floor  
            Washington, DC 20006  
            Attention: Mr. Michael McCracken  
                    Administrative Contracting Officer

\*Cover letter

JO:1601:ph